THE ENTRAINMENT INTERFACE LAYER OF STRATOCUMULUS TOPPED BOUNDARY LAYERS DURING THE PHYSICS OF STRATOCUMULUS TOP FIELD CAMPAIGN

by

Samantha Anne Hill

A thesis submitted to the faculty of
The University of Utah
in partial fulfillment of the requirements for the degree of

Master of Science

Department of Atmospheric Sciences

The University of Utah

December 2013

The University of Utah Graduate School

STATEMENT OF THESIS APPROVAL

The thesis of **Samantha Anne Hill**

has been approved by the following supervisory committee members:

Steven K. Krueger	, Chair	**8/13/2013** Date Approved
Timothy J. Garrett	, Member	**8/12/2013** Date Approved
Hermann Gerber	, Member	**4/24/2013** Date Approved

and by **Kevin D. Perry** , Chair/Dean of

the Department/College/School of **Atmospheric Sciences**

and by David B. Kieda, Dean of The Graduate School.

ABSTRACT

The stratocumulus topped boundary layers that tend to form off the west coast of major continents have been an important topic in cloud physics research due to their large impact on global climate, while uncertainty exists about their formation and behavior. This uncertainty is largely due to the substantial range of scales that govern the characteristics and evolution of these cloud decks. Specifically, small scale processes near cloud top have remained unexplored in the field due to limits in technology that inhibit the resolution necessary for these small scale processes to be investigated and studied. The entrainment interface layer (EIL), a region near cloud top where free tropospheric air is mixed with cloudy boundary layer air, is especially suspected to have an effect on these clouds. Three important processes occur in the EIL: mixing between free tropospheric air and cloudy mixed layer air, radiative heating and cooling, and heating and/or cooling due to phase changes of water, all of which may have an important effect on cloud properties and behavior.

The Physics of Stratocumulus Top (POST) field campaign took place in July and August of 2008 off the coast of Monterey, California with the mission of gathering data from the stratocumulus topped boundary layers that regularly form there each summer. The POST mission was unique in that it employed the use of a small aircraft, which allowed for colocation of instrumentation during research flights. This colocated instrumentation, coupled with vertical flight paths specifically designed to sample the region near cloud top of these cloud capped boundary layers, produced a data set especially equipped to probe into the small scale processes that are so pivotal to the behavior of these clouds.

Here, high rate data from POST are combined with a conserved variables analysis to

define the location and extent of the EIL for five flights during the summer of 2008. Two daytime flights and three evening flights were selected for analysis. Overall, the existence of an EIL is detected and defined for all five of the flights analyzed. In addition, for each case, the EIL is found to be noticeably thicker than what was found in past studies, with a typical extent of several tens of meters. Further use of conserved variables to approximate virtual potential temperature changes within the EIL reveals the effects of radiation and phase changes to be of the same order as each other, on average, for most of the flights. In addition, radiative cooling occurs most frequently during evening flights while solar warming occurs most frequently for daytime flights. Finally, evaporative cooling occurs much more frequently than condensational warming within the EIL for all flights, regardless of whether the flight was during the daytime or during the evening.

For my grandpa, Jim Balaich, who always encouraged and supported my dreams.

For my mother, Joyce Balaich, who first taught me the beauty of clouds.

TABLE OF CONTENTS

ACKNOWLEDGMENTS

I thank my advisor, Dr. Steve Krueger, for his guidance, patience, and inspiration over the last few years. I thank the members of my thesis committee, Dr. Tim Garrett and Dr. Hermann Gerber, for their insight into cloud physics and their suggestions regarding my work. I thank all of the members of the POST research team, especially Dr. Hermann Gerber and Dr. Szymon P. Malinowski, for providing the data necessary for the work presented within this thesis. I thank the Center for High Performance Computing at the University of Utah for computing support. I thank my friends within the University of Utah Atmospheric Sciences department who have made graduate school an incredible experience. I thank my wonderful friends Brittni Groothuis, Michael Schoffstall, Holly Reveal, Danielle Howey, Tyler Pulver, Elijah Stevens, David Gardner, and Sundari Nilsson for their love and emotional support over my entire college career. I am incredibly grateful to all of my grandparents, who taught me the immense value of a college education. I thank my late father, Michael Balaich; my mother, Joyce Balaich; and my sister, Micki Balaich, for their love, patience, encouragement, and support. I especially thank my husband, John, for his limitless understanding, encouragement, and love.

This research was funded by grants from the National Science Foundation.

CHAPTER 1

INTRODUCTION

For many years, the fine scale cloud structure near the top of stratocumulus topped boundary layers (STBLs) has remained unexplored due to limitations in aircraft and technology. This cloud top region in marine stratocumulus (Sc) is especially of interest because processes that take place there help to govern the behavior and persistence of the cloud decks that form at the top of these boundary layers. These small scale cloud top processes influence the physical characteristics of marine Sc cloud layers, including albedo, which currently plays a major role in keeping the earth's climate cooler than it would be in their absence due to the high amount of incident solar radiation these cloud decks reflect back to space (Bretherton 1997; Klein and Hartmann 1993). Thus, STBLs play an important role in Earth's radiation balance and climate (Hartmann et al. 1992). Furthermore, studies have shown that uncertainties in the behavior of Sc clouds inhibit prediction of an accurate future climate (Bony et al. 2006; Wyant et al. 2006). Therefore, largely due to their potential influence on climate, and due to the fact that little is understood about the small scale processes that influence the behavior of these clouds, STBLs have remained a central topic in cloud physics research.

This chapter will describe previous efforts to understand STBLs through observations and modeling, as well as introduce the entrainment interface layer (EIL) as the main topic of this thesis. Section 1.1 is a brief background of STBLs based on studies and investigations over the past several decades. Next, Section 1.2 gives a description of the entrainment

process at the top of Sc clouds, and the EIL that develops there as a result of this process. Section 1.3 is a quick overview of the use of conserved variables to study mixing processes involving saturated air. As a conclusion, the objectives of this thesis will be defined in Section 1.4.

1.1 A Brief Background of STBLs

STBLs tend to form under a layer of strong static stability, and are thus tightly connected to the general circulation of the atmosphere, which provides a strong subsidence inversion in the downward branch of the Hadley cell (Bretherton and Hartmann 2008). Specifically, the synoptic conditions during spring and summer off the west coast of California create ideal conditions for the formation of Sc clouds. The Pacific high pressure system, somewhat stationary over the Pacific Ocean, coupled with a thermal low that tends to form inland over the continental United States during summertime, create sharp pressure gradients across the western coast of the United States. This baroclinicity contributes to the formation of the Pacific Coast Jet, a phenomenon observed during several studies (Zemba and Friehe 1987; Gerber et al. 1989; Burk and Thompson 1996; Kalogiros and Wang 2001). This jet runs parallel to the west coast of the U.S., and its strong equatorward component causes oceanic upwelling in local waters. This upwelling brings colder water from below to the surface, making coastal sea surface temperatures much cooler than they would be normally.

The resultant oceanic environment due to this upwelling, which is exposed to turbulent eddies within the boundary layer, produces a layer of cool, moist air to develop. Thus, parcels of air are moistened by evaporation of water from the ocean surface and warmed, becoming positively buoyant. These buoyant parcels create practically neutral temperature profiles within the mixed layer (Paluch and Lenschow 1991). The formation of a saturated layer occurs when the cool and moist boundary layer becomes deep enough that it exceeds the lifting condensation level (LCL) of the cloud layer. Radiative processes begin once this

saturated layer grows to be on the order of a tens of meters thick (Paluch and Lenschow 1991), and cooling at cloud top begins. This cooling acts to create negatively buoyant parcels, sharpen the subsidence inversion, and may invoke convective instabilities which will eventually lead to a mixed layer capped by Sc clouds. A summary of the processes found within a typical STBL is shown in Figure 1.1.

Sc clouds are warm phase clouds, meaning the moisture contained within their boundaries is all in the form of liquid water and water vapor (no ice). The Sc clouds that populate STBLs generally form in the top few hundred meters of the boundary layer, making them not much colder than the temperature at the surface (Klein and Hartmann 1993). They are maintained via shallow convection, primarily driven by radiative cooling at cloud top (Lilly 1968; Nicholls and Leighton 1986; Nicholls 1989). There is some evidence for radiative cooling above cloud top (Deardorff 1981; Nieuwstadt and Businger 1984; Siems et al. 1993), and recently, peak values have been observed immediately above and adjacent to cloud top (vanZanten and Duynkerke 2002).

Several studies have shown latent heat due to condensation in STBLs can have a significant effect on the generation of buoyancy and turbulence (Lilly 1968; Schubert et al. 1979; Moeng et al. 1992; Bretherton and Wyant 1997). Just above cloud base, there is warming due to latent heat released once vapor contained in ascending parcels is condensed at the LCL, which can act to strengthen the convective circulation in the cloud layer. Aircraft studies outlined by Nicholls and Leighton (1986) and Duynkerke et al. (1995) confirm this, as substantial increases in buoyancy flux just above cloud base were observed in many cases. This buoyant production has also been related to fluxes of liquid water by turbulent eddies in STBLs (Bretherton and Wyant 1997). However, less pronounced circulations have been observed due to solar absorption by cloud droplets during daytime hours, which warms the tops of STBLs, and decreases overall cooling in the cloud layer (Duynkerke and Hignett 1993; Hignett 1991).

Evaporative cooling at cloud top may act to further cool the top of the saturated layer

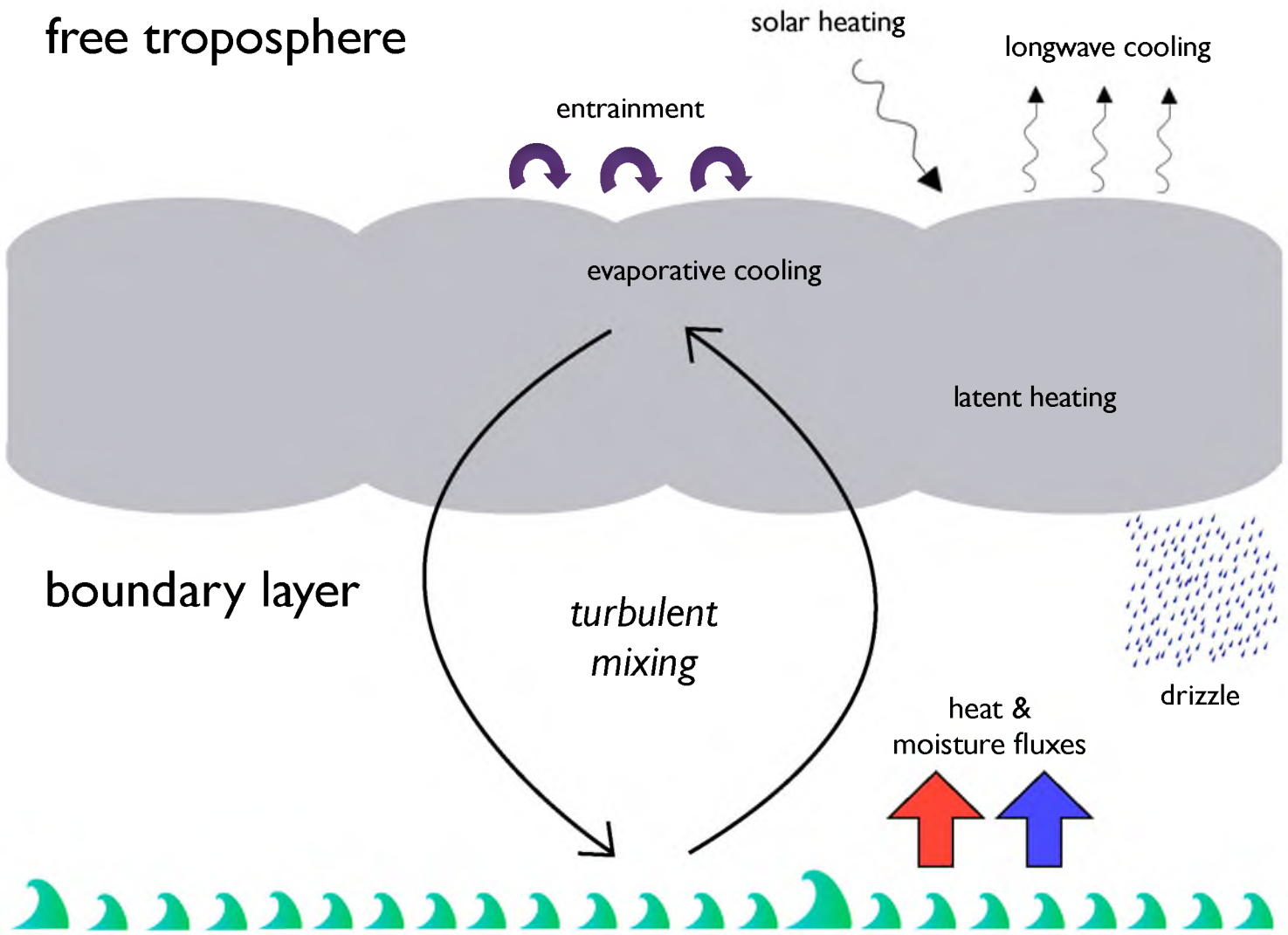

Figure 1.1: A summary of the circulations and processes found within a typical marine STBL.

or lead to thinning and possible dissipation of a cloud deck. Randall (1980) defines "conditional instability of the first kind upside down" associated with evaporative cooling and the shallow convection that maintains Sc cloud layers. He develops a criterion based on virtual dry static energy and buoyancy to indicate when evaporative cooling itself has the capability of inducing negative buoyancy and instability at cloud top.

Shallow convection in Sc is a product of all of the above effects, and is often the main mechanism of dynamics within a Sc layer (Lilly 1968; Nicholls 1984; Meong et al. 1996). Shallow convection also usually links the cloud layer to a surface moisture source, which works to sustain and even out the cloud deck (Nicholls 1984; Bretherton and Wyant 1997).

Finally, though Sc clouds do not produce substantial amounts of precipitation, thick Sc clouds have been known to develop drizzle (Nicholls and Leighton 1986; Petty 1995; Austin et al. 1995; Pawlowska and Brenguier 2003; Wood 2005; vanZanten et al. 2005; Leon et al. 2008). In fact, in regions where Sc clouds usually persist, drizzle is detected a significant amount of the time (Leon et al. 2008; Wood et al. 2009). The effects of drizzle on the dynamics of the cloud layer are highly complex, involving warming and drying of the cloud layer, and induced stratification of the STBL (Nicholls 1984; Wang and Albrecht 1986; Stevens et al. 1998; Mecham and Kogan 2003; Ackerman et al. 2009). In contrast, cloud thickness may grow if drizzle works to decrease entrainment of free tropospheric air into the mixed layer (Ackerman et al. 2004).

1.2 The Entrainment Process in Sc Clouds

The overturning associated with the shallow convection observed in STBLs causes some interaction between the moist, cloudy air at the top of the mixed layer, and the dry, overlying air of the free troposphere. Updrafts within the cloudy layer reach the stable capping inversion and spread out horizontally, as further vertical motion is inhibited by strong static stability above. Oftentimes, near the interface between the cloudy upper mixed layer and free troposphere, the interaction between these two layers is in the form of entrainment,

a process by which dry, free tropospheric air is drawn into the cloud layer from below by turbulent eddies in the mixed layer penetrating upward. This turbulence acts to pull free tropospheric air into the cloud, where it is mixed with saturated air. The exposure of cloud droplets to subsaturated air causes subsequent evaporation and cooling, which may influence the shallow convection in the cloud layer, further promoting entrainment (Lilly 1968; Randall 1980; Nicholls and Turton 1986).

Krueger et al. (1993) show that this mixing is a two part process whereby turbulent deformation of the two fluids works with molecular diffusion across fluid filament interfaces to eventually produce a uniform mixture. Model results have shown explicit representation of turbulent deformation and molecular diffusion in mixing processes within clouds is important due to the fact that molecular diffusion is not a significant factor in the mixing process until turbulent deformation has increased scalar gradients (Krueger 1993). This is a crucial factor because it is molecular diffusion that brings subsaturated air in contact with cloud droplets to initiate evaporation; therefore, these details in mixing are important to the evaporation rate near the top of the cloud layer (Krueger 1993).

Entrainment can have a variety of effects on the mixed layer. It tends to deepen the STBL through the incorporation of free tropospheric air, and, as it does so, it may become so deep that longwave cooling and evaporative cooling are less likely to support mixing through the entire boundary layer (Bretherton and Wyant 1997). At that point, the STBL will separate into two distinct layers: a mixed upper layer containing the cloud layer, and a second layer near the surface. This process is called decoupling of the cloud layer, and is documented in many studies (Albrecht et al. 1995; Bretherton and Pincus 1995; Bretherton et al. 1995; Krueger 1995a-b; Wyant et al. 1997; Miller et al. 1998).

A second possible influence of entrainment is the development of Cloud Top Entrainment Instability (CTEI), a phenomenon suggested by Randall (1980) and Deardorff (1980), furthering the idea from Lilly (1968). This theory dictates that there are certain circumstances under which negatively buoyant downdrafts may be generated by mixtures of cloudy

and free tropospheric air. Subsequently, these downdrafts may strengthen turbulent kinetic energy (TKE) in the cloud layer, leading to more entrainment, accelerating the process. Randall (1980) and Deardorff (1980) suggest that if this positive feedback were to develop, it would quickly dry the STBL and lead to evaporation of the cloud layer. However, data from the field show STBLs existing under the proposed theoretical conditions of CTEI (Kuo and Schubert 1988; Weaver and Pearson 1990; de Roode and Duynkerke 1997). Several revisions to the CTEI criterion have been formulated (MacVean and Mason 1990; Siems et al. 1990; Duynkerke 1993), some of which point to a weaker inversion in order for a jump in moisture to create unstable conditions. Consequently, it is less probable to find conditions which satisfy CTEI in the field, which is much more consistent with observations. In addition, recent modeling endeavors show that CTEI may be hidden by other processes that are conducive to prolonging the life of the cloud layer (Yamaguchi and Randall 2008).

1.2.1 The Entrainment Interface Layer

The mixing that occurs across cloud top has been thought to lead to a relatively thin layer between cloudy mixed layer air and free tropospheric air that has thermodynamic properties intermediate to the two types of air. Caughey et al. (1982) first dubbed this region above cloud top the "entrainment interfacial layer," and described its structure based on observations, as has been done in several other studies (vanZanten and Duynkerke 2002; Gerber et al. 2005; Haman et al. 2007). Caughey et al. (1982) and Nicholls and Turton (1986) showed that the transition from the cool and moist cloudy layer to the warm and dry free troposphere does not happen abruptly, but is instead a region of transition with measurable thickness.

When compared to the atmosphere lying above it, the entrainment interface layer (EIL) is cool and moist (Brenguier and Wood 2009; Wang and Albrecht 1994). Haman et al. (2007) focused on one flight from the DYCOMS II field campaign during July 2001 over the eastern Pacific Ocean to investigate the processes taking place in and around the EIL,

as well as to document EIL characteristics. Overall, they found the thickness of the EIL to be small, typically less than 20 meters. In addition, they used high rate data to detect very thin filaments of cloudy and clear air at different stages of mixing among a background of turbulence. In a more recent study, Yamaguchi and Randall (2012) used LES model results and a conserved variables analysis to approximate EIL thickness and to diagnose the effects of radiation, evaporation, and mixing within the EIL. Their results showed an EIL thickness of several tens of meters. Also, they found the effects of radiation and phase changes to be of comparable magnitude, while the mixing process itself is, by far, the primary contributor to the final temperature of a mixed parcel.

Important implications from studies of the EIL are that the cloud top does not necessarily mark the top of STBLs (Lenschow et al. 2000), and that the EIL may play a vital role in establishing an entrainment rate and setting the degree to which the cloud top is stable with respect to entrainment (Wang and Albrecht 1994; Gerber et al. 2005; de Roode and Wang 2007). Since its discovery in the early 1980s, investigators have been seeking ways to study the EIL in more detail to reveal its characteristics, evolution, and central role in the development and dissipation of Sc decks lying at the top of marine boundary layers. A diagram of entrainment circulations near the top of an STBL is shown in Figure 1.2.

Though the direct connection between the EIL and entrainment remains under scrutiny by current research efforts, the EIL seems to play an important role in the entrainment process. In their recent study, Yamaguchi and Randall (2012) were able to observe individual parcels undergoing the entrainment process through the use of a Lagrangian Parcel Tracking Model integrated into a Linear Eddy Model. Their results support the hypothesis that the EIL is a region where parcels are cooled and moistened by detrained air from the top of the cloudy mixed layer. Their results also show that temperature (and hence buoyancy) changes of parcels are mostly affected by the physical process of mixing along with minor contributions from phase changes and radiative processes, both of which tend to be of the same order of magnitude. Negative buoyancy changes within the EIL can be conducive to

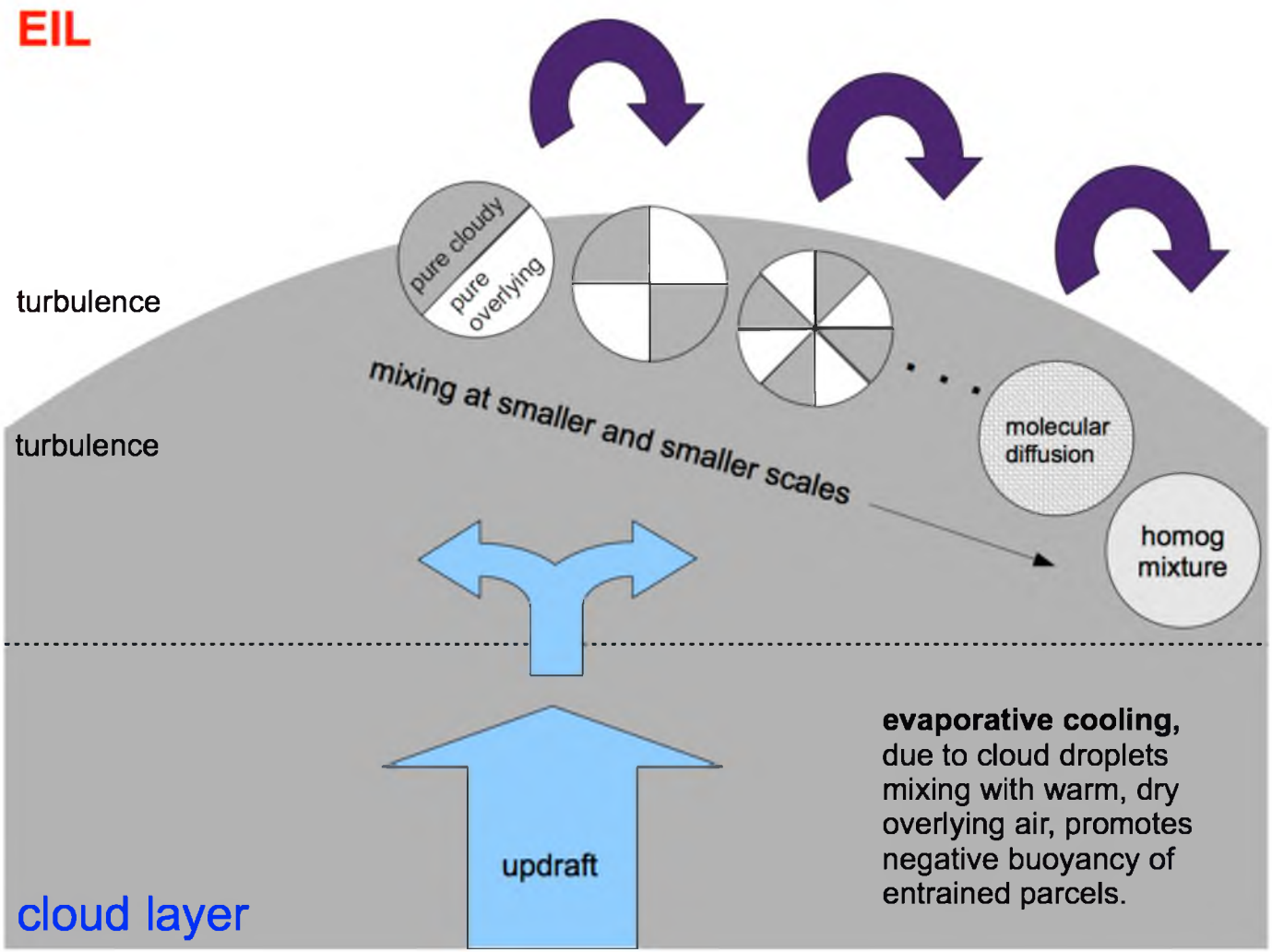

Figure 1.2: Cloud top circulations and entrainment in the EIL.

entrainment, as they tend to lead parcels toward downdrafts in the mixed layer where free tropospheric air is further mixed with saturated air of the cloudy mixed layer.

1.3 Conserved Variables and Mixing

The use of conserved variables to investigate mixing between two thermodynamically distinct types of air within clouds has been employed in several studies (Burnet and Brenguier 2007; Paluch 1979; Pearson 2002). Specifically, this type of analysis has proven useful to study parcels in the midst of entrainment as dry and warm free tropospheric air mixes with cool and moist cloudy air. Moist conserved variables, such as total water mixing ratio (q_t) and liquid water potential temperature (Θ_l), are important for these analyses, as they are conserved quantities under moist adiabatic processes, and will remain relatively constant, regardless of the parcel's altitude in the atmosphere. For two parcels of different types of air that are mixing, a conserved variable, such as q_t, of the new mixture will have a q_t which is a linear combination of the q_ts of the original parcels, weighted by the mass contribution of each original parcel to the mass of the resultant mixture:

$$q_{t,mix} = (1 - \chi) * q_{t,a} + \chi * q_{t,b}, \tag{1.1}$$

where $q_{t,a}$ is the total water mixing ratio of the first parcel, and $(1 - \chi)$ is the fraction of unit mass contributed to the final mixture from the first parcel, while $q_{t,b}$ is the total water mixing ratio of the second parcel, and χ is the fraction of unit mass contributed to the final mixture from the second parcel.

Due to this linearity of mixing for conserved variables, all possible mixing states for a resultant mixture which is the product of mixing between two original parcels lie on a straight line connecting a point representing the thermodynamic characteristics of the first parcel and a point representing the thermodynamic characteristics of the second parcel. A diagram illustrating this is shown in Figure 1.3. This concept will be used in Chapter 3.

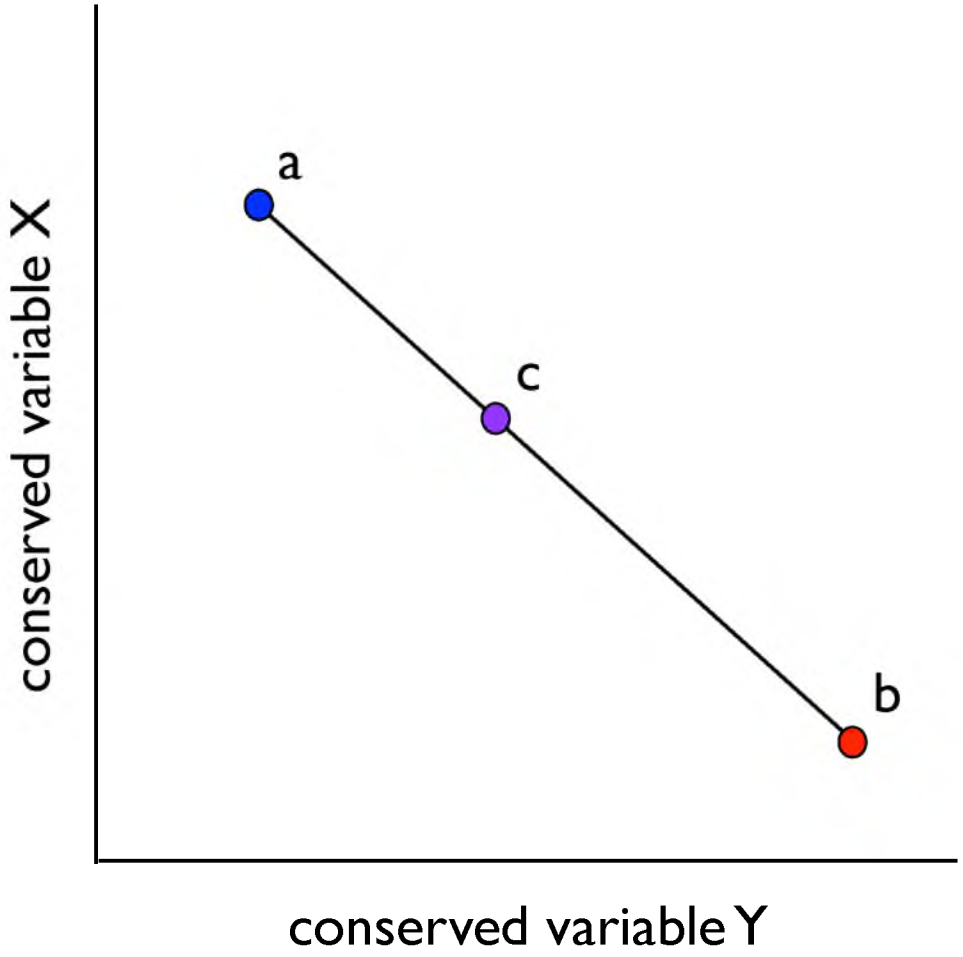

Figure 1.3: Mixing line diagram for mixing between two parcels of air with original mixing states a and b, plotted in terms of two conserved variables that mix linearly. For a parcel c, formed from mixing parcel a and parcel b, its mixing state will fall along the line connecting a and b according to the amount of each of parcels a and b mixed into parcel c.

For studying mixing near the top of Sc clouds, one original mixing state is taken to be the pure cloudy mixed layer below the top of the STBL, and the second original mixing state is taken to be the pure free troposphere overlying the EIL. VanZanten and Duynkerke (2002) suggest a method for using a conserved variable called mixing fraction to study radiative and phase change effects on virtual potential temperature changes at the top of a Sc layer. Mixing fraction is a measure of the amount of one type of air mixed into a parcel of a second type of air, based on ratios and differences in q_t for the two types of air. This method will be further explained in Chapter 3.

1.4 Thesis Outline

The analyses within this thesis were based on data from the Physics of Stratocumulus Top (POST) field campaign, which was specifically designed for investigating the small scale processes near cloud top and the EIL of STBLs through the use of colocated, high response airborne instrumentation and specially designed flight plans.

The goals of this thesis are to use the methodology of vanZanten and Duynkerke (2002) to detect and to define the EIL for five research flights from the POST field campaign, as well as to diagnose the relative contributions of radiative and phase change processes to temperature changes within the EIL, as defined by this method. Chapter 2 is a description of the POST field campaign, which includes a description of data from the five flights that were selected for analysis. Methodology and results for mixing fraction calculations and approximation of the location and extent of the EIL are given in Chapter 3. Chapter 4 includes a statistical analysis of EIL thickness, a glimpse at time evolution of the EIL, and an alternate way of detecting the EIL based on turbulence characteristics. Methods and results for virtual potential temperature changes due to radiation and phase changes, also motivated by vanZanten and Duynkerke (2002), are outlined in Chapter 5, and Chapter 6 is a discussion of major results of this study, which includes suggestions for future work.

CHAPTER 2

THE PHYSICS OF STRATOCUMULUS TOP PROJECT

2.1 The Field Campaign

The Physics of Stratocumulus Top (POST) field campaign took place during the months of July and August in 2008 to investigate the fine-scale structure of entrainment and other mixing processes near the top of STBLs, and to examine the properties of the EIL in these types of boundary layers. This field experiment used a Twin Otter Turboprop aircraft with a wingsan of only 65 feet, just under two times smaller than the wingspan of the NSF RC-130, an aircraft used in many previous Sc studies. In the past, on the RC-130, some probes were located up to six meters apart, preventing proper spacial correlation of data. The small size of the Twin Otter aircraft allowed for colocation of fast response instruments, enabling accurate calculations of important quantities, such as entrainment rate and radiative cooling at cloud top. This allowed for the study of fine scale structure and small scale processes taking place in the Sc clouds observed during the campaign.

With the EIL being a primary focus of the POST project, vertical flight plans were specially designed to collect data from within the EIL, and from the regions transitioning into, and out of, the EIL. These flightpaths were comprised of three (sometimes four) sections of repeated "sawtoothing" through the cloud deck, meaning the aircraft would dip down into the cloud layer, and then once in the cloud layer, would rise back up above the cloud layer. This pattern was repeated several times within a section of the flight path. Also, level legs

were flown near the surface, in-cloud, and just below the cloud layer for later calculation of fluxes. An example of a typical vertical flight path is shown in Figure 2.1.

In the horizontal, the flight path was prescribed as well, in an attempt to capture consistent parcels of air. Instead of simply flying down the coast or maintaining a straight path within the Sc layer, the pilot was assigned to fly a quasi-Lagrangian flight path, meaning the aircraft would follow the general flow of the surrounding atmosphere, resulting in an overall zigzag pattern. An example of the horizontal Lagrangian flight path from Research Flight 10 is shown in Figure 2.2.

The Twin Otter aircraft was outfitted with several instruments, many of which could be considered colocated due to very closely located mounts on the aircraft. Specific to this research is the Ultra Fast Thermometer (UFT), which took temperature measurements at a frequency of 1000 Hz.; the Particle Volume Monitor (PVM) which measured liquid water content (LWC) at a frequency of 1000 Hz.; and the UCI LICOR hygrometer, which measured the water vapor mixing ratio, whose data was placed in the archive at 40 Hz.

By the end of the POST mission in mid August of 2008, data had been collected from a total of 17 flights, 9 during the day and 8 during the evening/night. Most flights were approximately 5 hours long. The variety of flights (daytime and nighttime, under various atmospheric conditions) allowed for study of the EIL under many different circumstances.

The results presented in this thesis are based on five flights selected from the POST field campaign, each exhibiting special cases involving time of day, cloud cover, moisture content of the mixed layer, moisture content of the overlying free atmosphere, or observed jump in thermodynamic properties across the inversion at the top of the mixed layer.

2.2 Observational Data

Most of the data collected during POST were gathered by high rate, fast response probes at a frequency of 1000 Hz. However, this high rate data was averaged to a rate of 40 Hz. due to the fact that the PVM and LICOR probes on the nose of the Twin Otter aircraft were

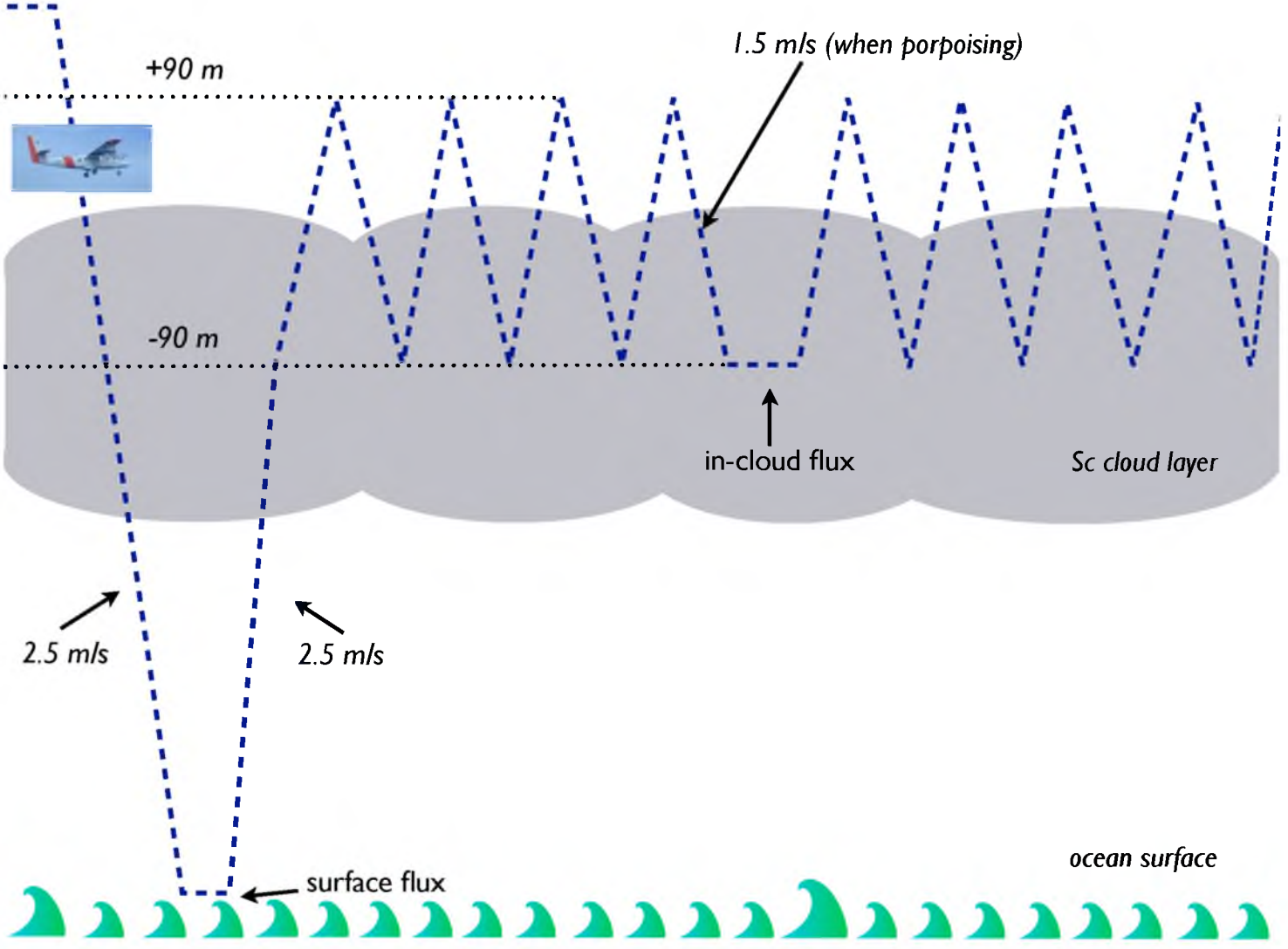

Figure 2.1: Typical vertical flight plan for POST missions.

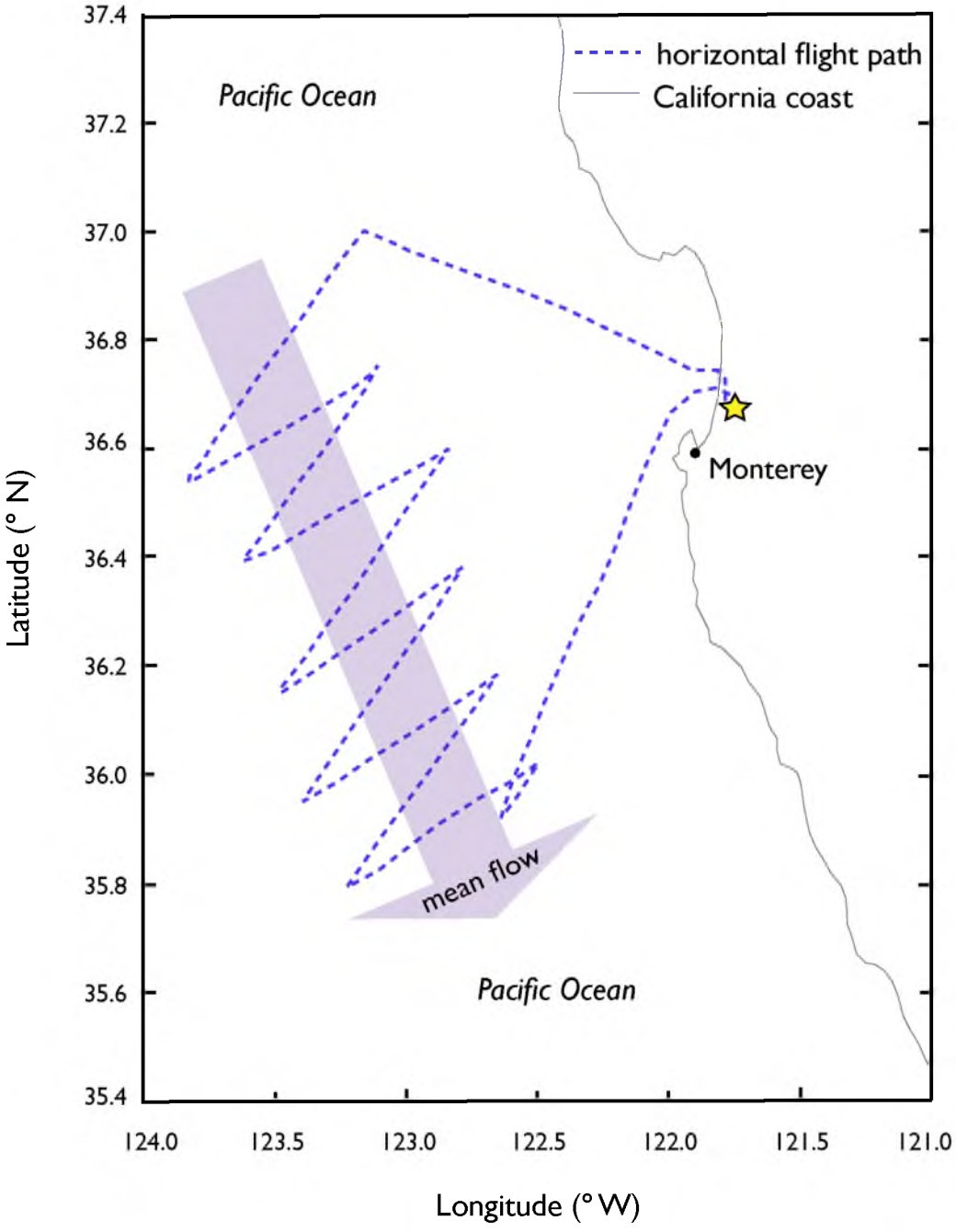

Figure 2.2: Typical Lagrangian flightpath in the horizontal domain for POST missions.

separated by a distance of one meter. Given that the aircraft was traveling at approximately 50 m/s, averaging to 40 Hz. would provide a spacial resolution of 1.25 meters; a data rate any higher than this would make correlations between the data prone to errors as the separation distance between the probes would have been larger than the separation distance between data points. This averaging to 40 Hz. was accomplished using matrix techniques in Matlab. Data from aircraft cabin instruments were used for calculations involving ambient air pressure and height data. As the recording frequency for the cabin instruments was only 10 Hz., these data were interpolated to 40 Hz. as well, using Matlab interpolation functions.

As was already mentioned, each flight included sections of "porpoising" in and out of the cloud layer, as well as horizontal legs for calculating fluxes. The analyses described here mainly focus on studying the extent and structure of the EIL; therefore, they focus on the portions of each flightpath that are comprised of porpoising, and the data used for these analyses are solely those data points from within the porpoising sections of the flightpath. These sections were defined based on a required amount of repetitive porpoises in and out of the cloud layer in a given amount of time. These groups of repetitive porpoises during each flight were named "pods." In most cases, each flight contained three pods comprised of at least five porpoises each. Most of the results in the following analyses are given in the form of results from pods of a given flight. A sketch of the vertical flightpath from one flight during POST with pods highlighted in red boxes is shown in Figure 2.3.

2.2.1 Data Issues

By plotting water vapor mixing ratio as gathered by the UCI LICOR water vapor hygrometer, and by separating data points into saturated points and unsaturated points (based on a threshold value of liquid water mixing ratio), it was found that the instrument exhibited anomalously low vapor values upon exiting and entering the cloud layer for all flights. To attempt to correct for these erroneous values, the water vapor data were plotted against mixing fraction, and a linear fit was then made to the data. Finally, all points a distance

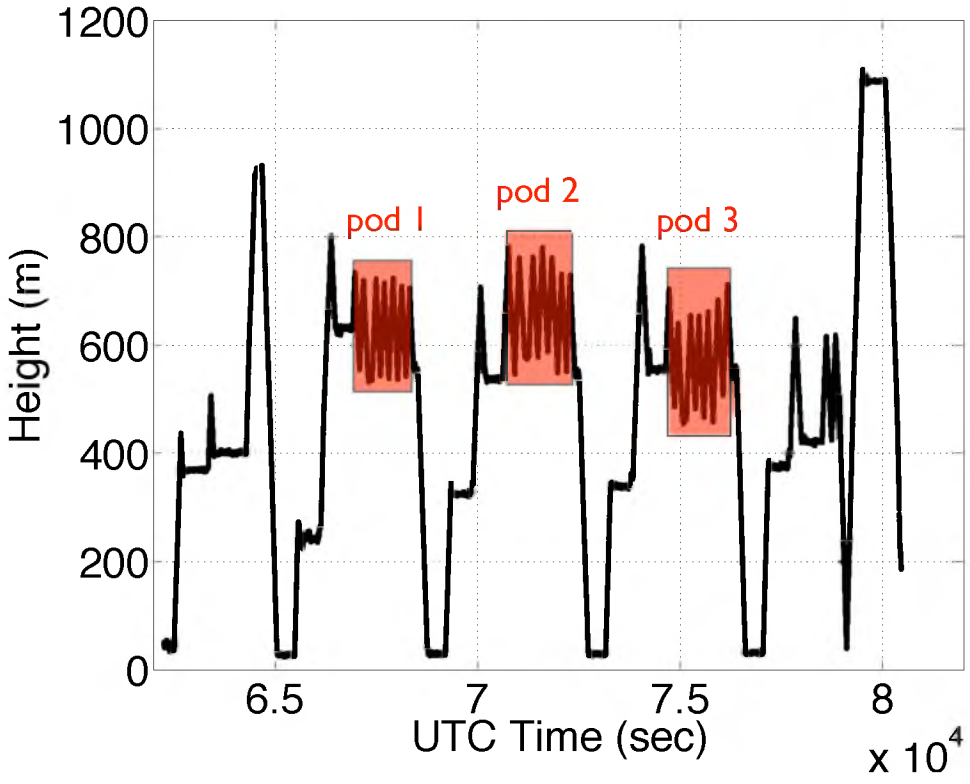

Figure 2.3: Total vertical flight plan from POST Research Flight 10 with pods highlighted with red boxes.

greater than three times the root mean squared error away from the linear fit were eliminated from the data set. These revised data sets for water vapor mixing ratio were used for the actual analyses.

2.3 Flights For Analysis

When selecting flights for analysis, several criteria were considered. Firstly, for a flight to be valid for our analyses, the aircraft needed to have followed the prescribed Lagrangian flightpath in the horizontal field of motion. This condition was not met for two of the flights, namely RF04 and RF09, due to airspace restrictions on the days these missions were flown. Therefore, they were discarded immediately. A second criterion for analysis was whether the flight data showed distinct characteristics of mixing through the use of a mixing line analysis, which will be discussed in further detail in a following chapter. This narrowed the focus of our analyses to a subset of flights: RF05, RF06, RF10, RF11, RF12, RF14, RF15, and RF16, most of which are evening flights. The results presented here will focus on RF10 and RF16 (daytime flights), along with RF11, RF12, and RF14 (evening flights).

2.3.1 Research Flight 10

RF10 took place on August 4, 2008, and was flown from 10:12 a.m. to 3:23 p.m. Pacific Standard Time, making it a daytime flight, for a total of 5.2 hours. According to flight notes for this mission, the Sc cloud layer that day was uniform, with clear, free atmospheric air above the cloud top inversion. The Sc layer was also observed to thin during the duration of the flight. Maximum winds of 8 to 9 m/s were observed in the cloud layer, with a sharp drop off in winds just above the cloud layer to 2 to 3 m/s. Also, toward the end of the flight, a clear, moist layer was observed just above the cloud layer with the same vapor content as the cloud. The horizontal and vertical flight paths for RF10 are shown in Figure 2.4.

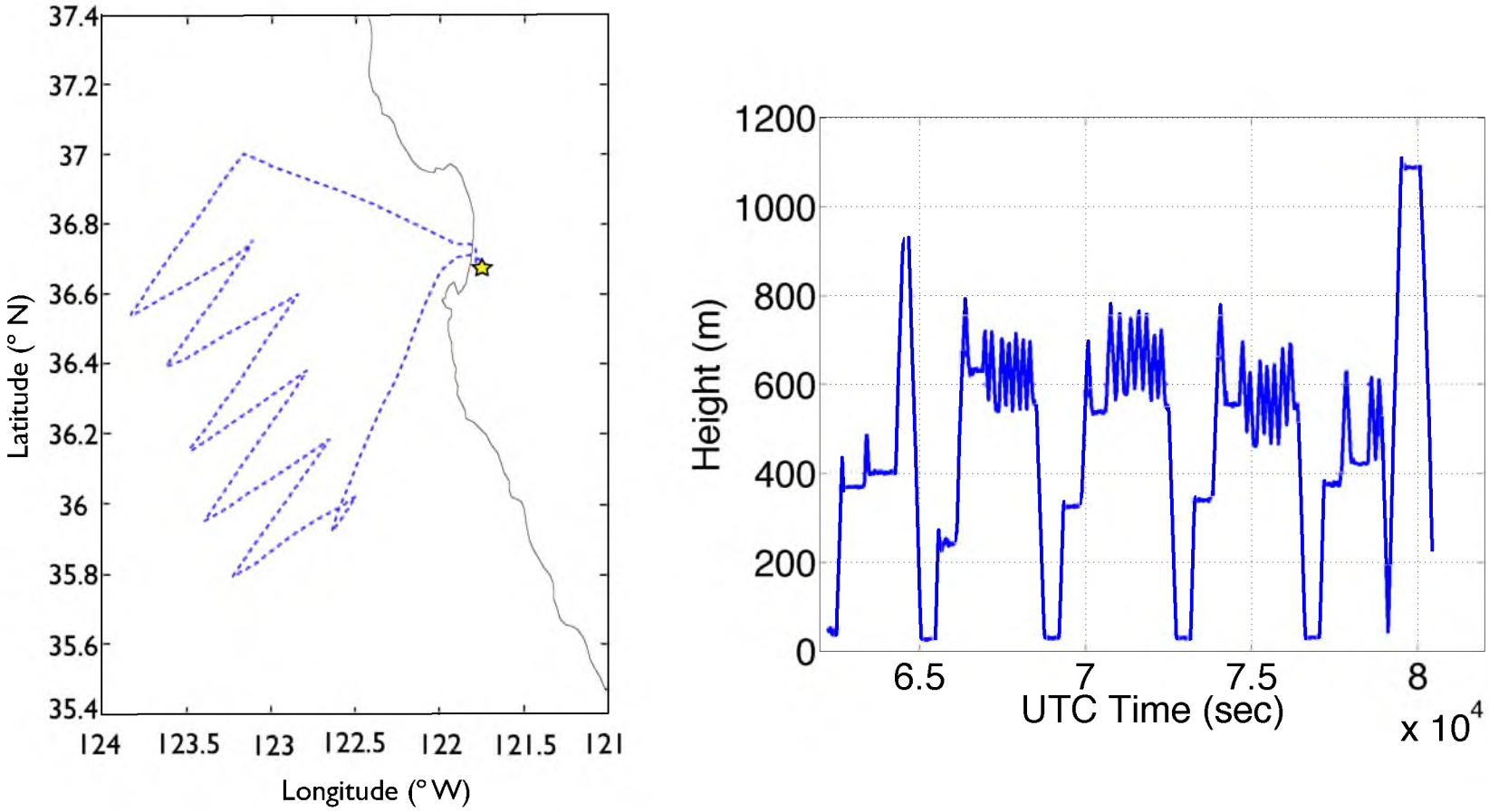

Figure 2.4: Horizontal and vertical flight paths for daytime RF10.

2.3.2 Research Flight 11

RF11 took place on August 5, 2008 from 5:57 p.m. to 10:48 p.m. Pacific Standard Time, making it an evening flight, for a total of 4.9 hours. The boundary layer during RF11 was supporting very little cloud cover near the beginning of the flight. Clouds were sparse, and the flight path had to be altered to get to areas where the instrumentation could sample cloudy mixed layer air. When clouds were encountered, the cloud deck was very thin, at around 400 meters thick, and, even in these cases, observed LWC was low. In addition, cirrus clouds were observed above the Sc layer for the majority of the flight. A shear layer was suspected just above cloud top due to winds observed at a little less than 10.5 m/s from the north northwest in the boundary layer, which changed to 2.5 m/s from the south southwest above the inversion. The horizontal and vertical flight paths for RF11 are shown in Figure 2.5.

2.3.3 Research Flight 12

RF12 took place on August 7, 2008 from 5:55 p.m. to 10:53 p.m. Pacific Standard Time, making it an evening flight with a total duration of approximately 5.0 hours. During this flight, the cloud bases were higher than normal, and the cloud deck itself was reported as "very solid." No cirrus clouds and no overlying haze layer were observed during the totality of the flight. Before sunset, a layer of cloudy air seemed to have formed below the dominant top layer of clouds. This dissipated soon after the sun went down. Horizontal and vertical flight paths for RF12 are shown in Figure 2.6.

2.3.4 Research Flight 14

RF14 was flown on August 11, 2008 from 5:57 p.m. to 10:48 p.m. Pacific Standard Time, making it an evening flight with a total duration of 4.9 hours. A moist overlying layer seemed to be due to a thick layer of haze located above the mixed layer during this flight. LWC values during RF14 were higher than LWC values on other flights, further

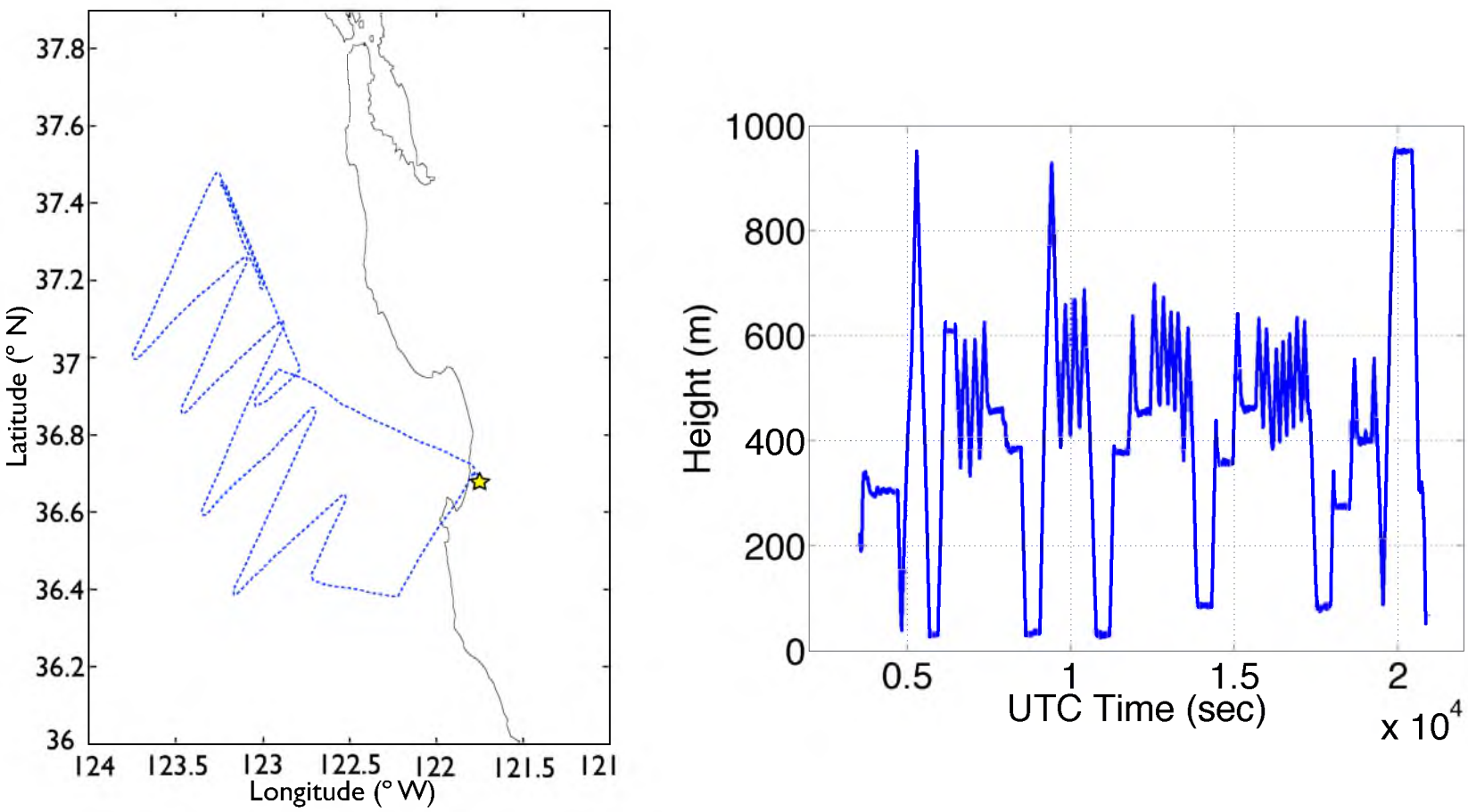

Figure 2.5: Horizontal and vertical flight paths for nighttime RF11.

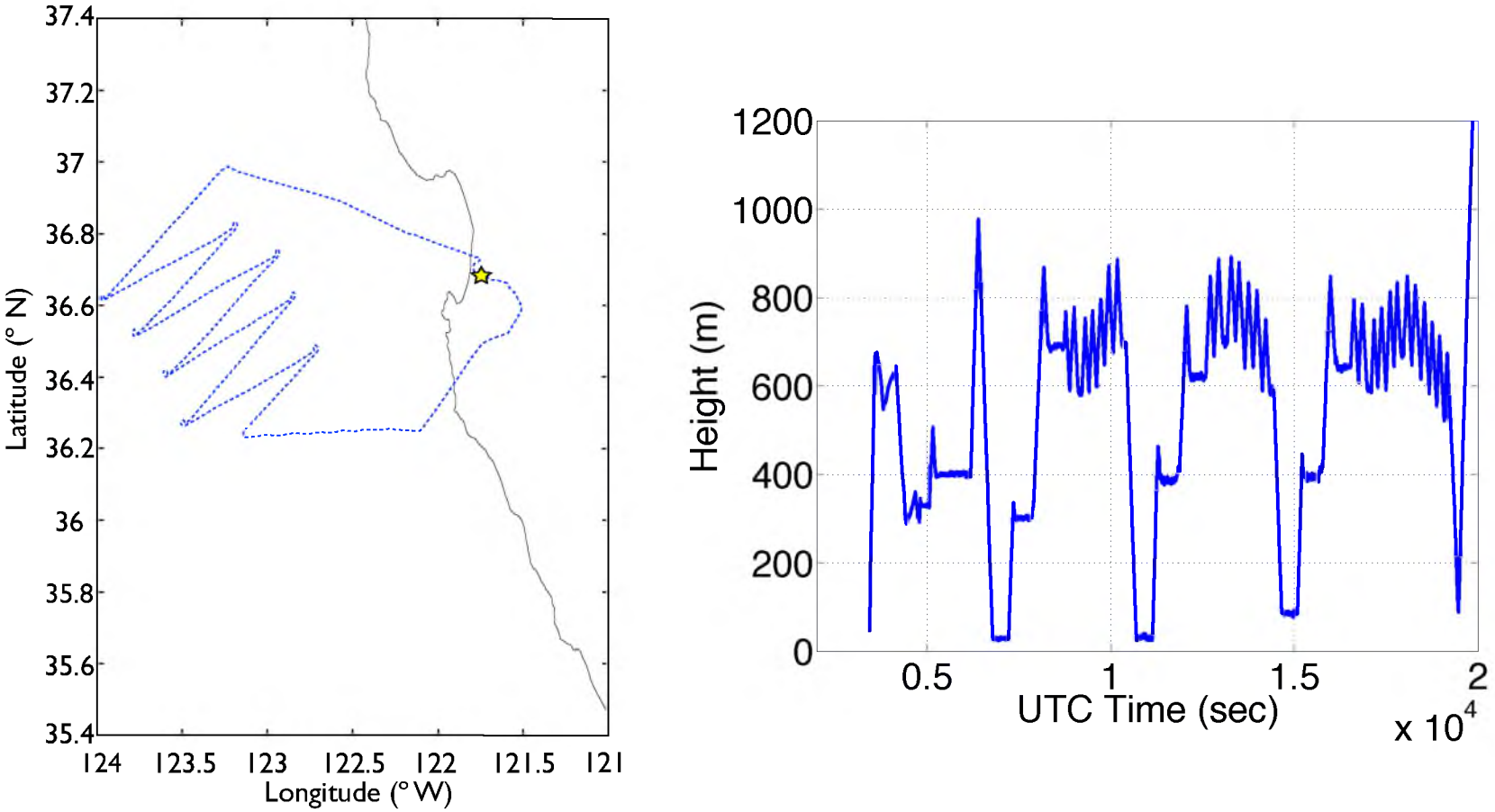

Figure 2.6: Horizontal and vertical flight paths for evening RF12.

illustrating the moist state of the mixed layer on this evening. All reports of the clouds during this flight were of a uniform cloud deck. Figure 2.7 shows the horizontal and vertical flight paths from RF14.

2.3.5 Research Flight 16

RF16 was flown on August 14, 2008 from 10:28 a.m. to 3:02 p.m. Pacific Standard Time, making it a daytime flight with a total duration of 4.6 hours. Cirrus clouds were observed during this flight, and winds were at about 1.5 m/s out of the north northwest. Figure 2.8 shows the horizontal and vertical flight paths from RF16.

2.4 Data Access

Data from these five flights will be used in the following chapters to locate the EIL, as well as diagnose heating and cooling within the EIL for a typical California STBL. A complete set of data collected during the POST field campaign is available for download from that National Center for Atmospheric Research's Earth Observing Laboratory website at http://www.eol.ucar.edu/projects/post/.

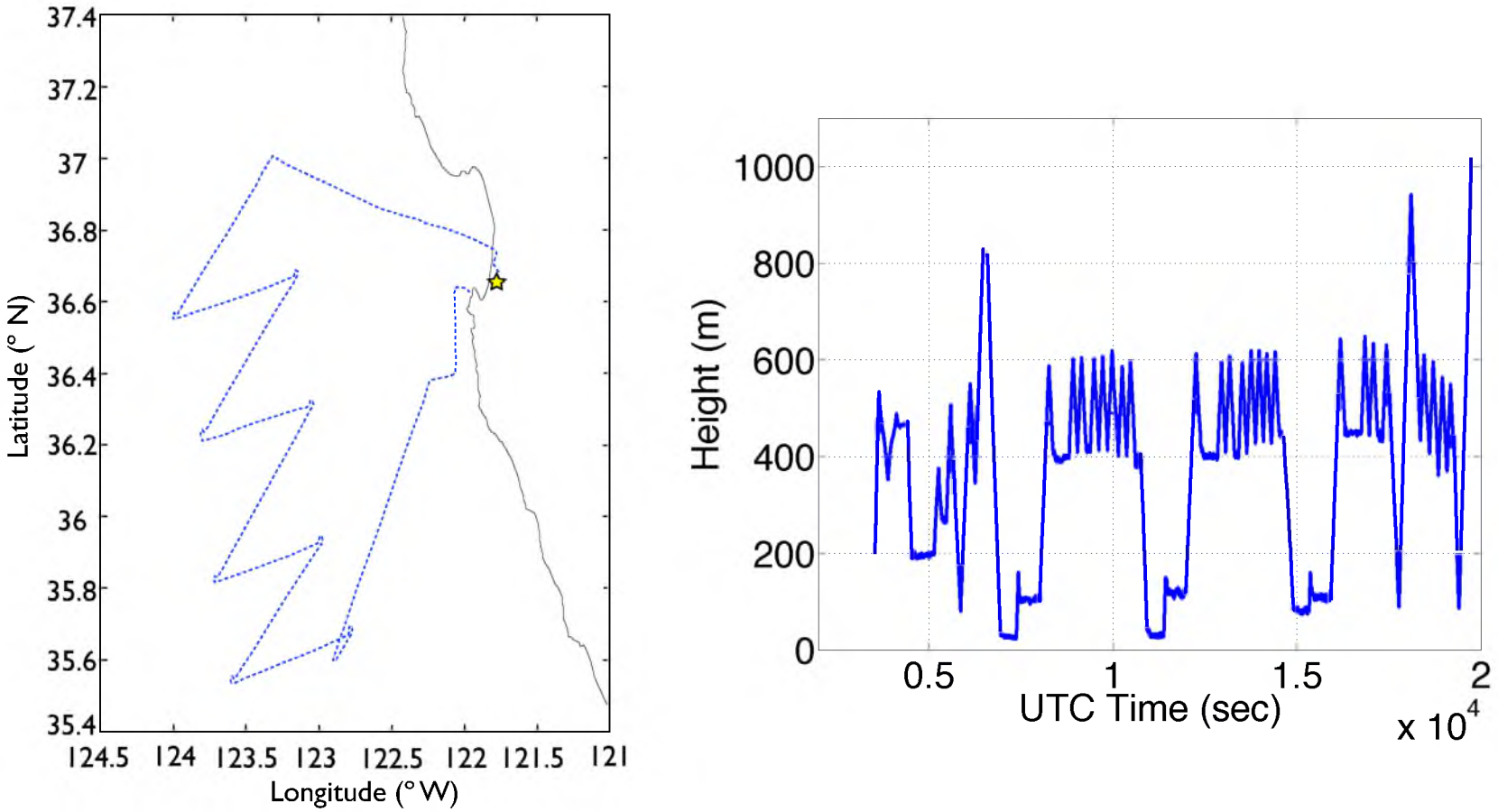

Figure 2.7: Horizontal and vertical flight paths for evening RF14.

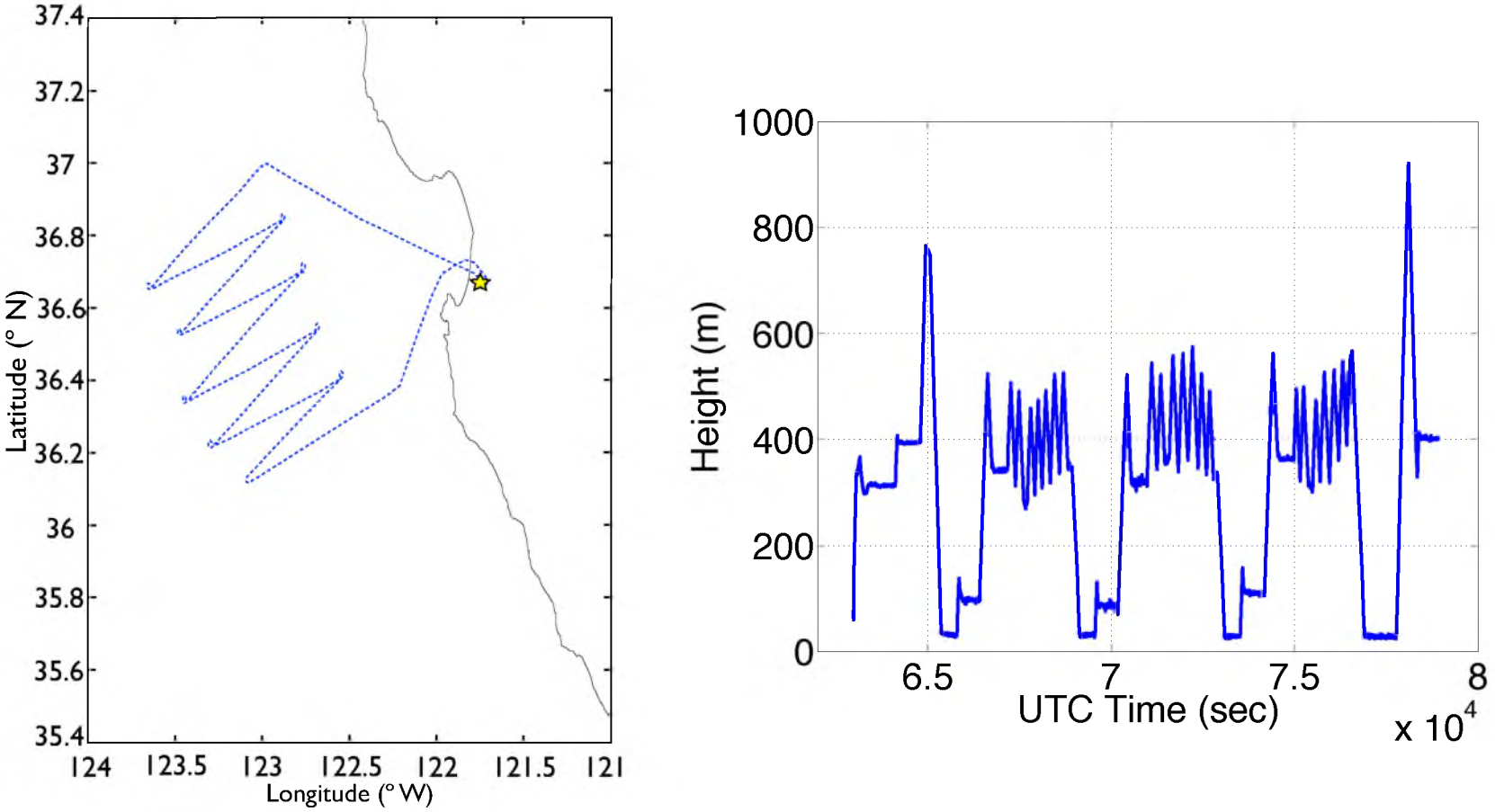

Figure 2.8: Horizontal and vertical flight paths for evening RF16.

CHAPTER 3

MIXING FRACTION: LOCATING THE EIL

This chapter will introduce the moist conserved variable mixing fraction (χ) as a unique technique for identifying the regions near the top of the mixed layer observed during POST that show qualities characteristic of parcels in the the midst of mixing processes. This variable provides a new way of plotting the flight path, as will be shown in the last part of the chapter.

3.1 Saturated and Unsaturated Data Points

To begin the analyses, the data for each flight were separated into saturated and unsaturated points based on liquid water mixing ratio. This liquid water mixing ratio (q_l) was calculated from the liquid water content (LWC) data measured by the Particle Volume Monitor (PVM) mounted to the Twin Otter aircraft. For this conversion, the following equation was used:

$$q_l = \frac{LWC}{\rho} \tag{3.2}$$

where ρ is the dry air density, taken to be a good approximation for ambient air density during the course of all flights. This density was calculated using the equation of state for the atmosphere:

$$\rho = \frac{p}{RT} \tag{3.3}$$

where p is pressure from the cabin instruments, T is temperature from the UFT, and R is the gas constant for dry air, 287.05 J/kg K.

Cloud fraction was used next to determine whether a given data point in the averaged 40 Hz. data set should be considered saturated or unsaturated. This quantity was calculated as follows. First, the original 1000 Hz. data set was needed for LWC because the new 40 Hz. data was created by averaging every 25 data points of the original 1000 Hz. data. Though this new form of averaged data was adequate for other steps in the analyses, it created an "average parcel," which represented the *average* LWC of the parcel over 1/40 of a second, instead of accurately representing the *actual* instantaneous LWC of the parcel at each point in the flight path measured at 1000 Hz. In other words, simply using a liquid water threshold with the averaged 40 Hz. data was making too much of an assumption about the saturation of original parcels of air along the flight path as sampled at 1000 Hz. Therefore, the 1000 Hz. LWC time series was broken up into subsets of 25 data points, and each subset was compared to a threshold of 0.05 g/kg. Data points meeting or surpassing the threshold within the subset were given a value of 1, and data points less than the threshold were given a value of 0. Next, these 25 points (with values 0 or 1) were averaged. This provided a "cloud fraction" value for each 1/40 of a second. If the cloud fraction value was equal to 1, that 1/40 of a second in the averaged data set was considered saturated, but if the cloud fraction value was less than 1, that 1/40 of a second in the averaged data set was considered unsaturated.

This enabled us to make an approximation of the extent of saturated and unsaturated air along the flight path. Examples of flight paths with saturated (blue) and unsaturated (black) points are shown in Figure 3.1.

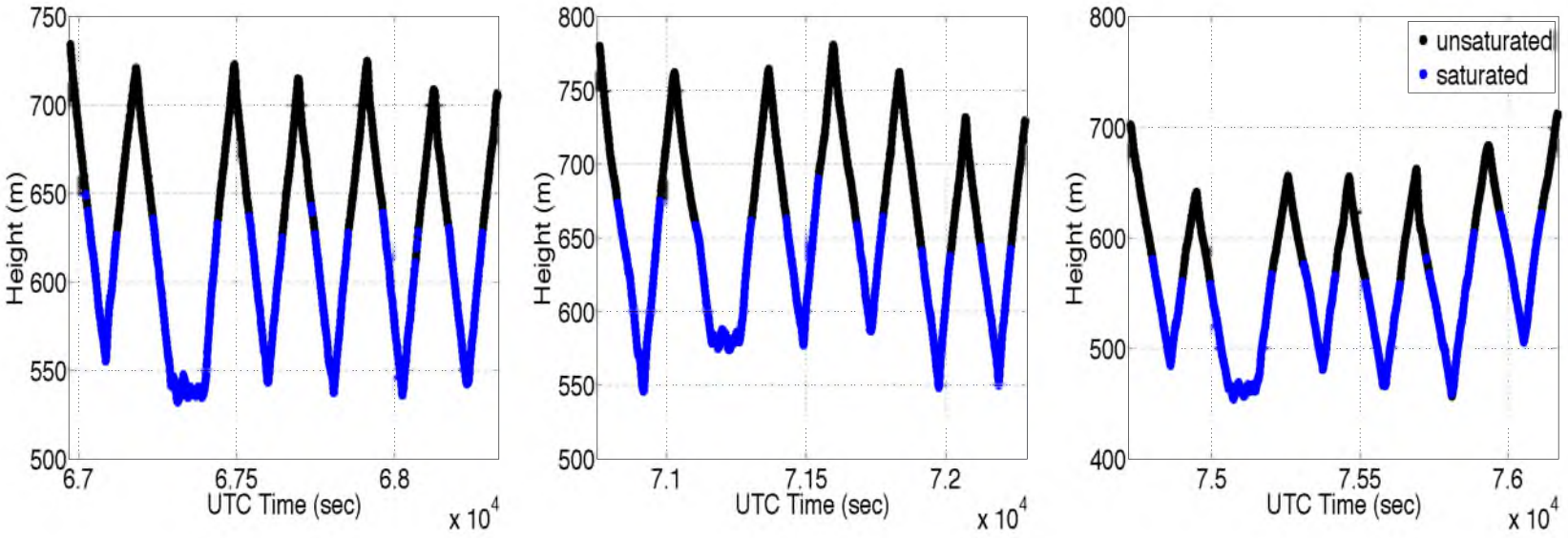

Figure 3.1: Saturated points (blue) and unsaturated points (black) show the approximate vertical extent of the cloud layer and location of cloud top for three pods of RF10.

3.2 Conserved Variables

Locating mixing events at the top of the STBLs during POST first required defining pure mixing states in and above the boundary layer. Moist, turbulent, cloud layer air was defined as one such mixing state, and dry, warm, free troposphere air from above the inversion was defined as a second pure state. The mixing of these two pure states was used to study the properties of the EIL. First, it was necessary to select and use variables that are conserved under both dry adiabatic and moist adiabatic processes due to the presence of moisture in both vapor and liquid phases throughout circulations within the mixed layer. The two moist conserved variables selected for this analysis were total water mixing ratio (which remains constant though moisture may change from the vapor state to the liquid state, or visa versa, assuming no precipitation), and liquid water potential temperature.

Total water mixing ratio was calculated as the sum of water vapor mixing ratio and liquid water mixing ratio:

$$q_t = q_l + q_v. \tag{3.4}$$

Liquid water mixing ratio was again calculated from data collected onboard the Twin Otter. Liquid water potential temperature was calculated (to a first approximation) using

$$\Theta_l = \Theta - \frac{L_v}{c_{pd}} q_l, \tag{3.5}$$

where Θ is the ambient potential temperature (which was calculated using Poisson's equation and ambient temperature measurements from the UFT), L_v is the latent heat of vaporization ($2.5x10^6 J/K$), c_{pd} is the specific heat of dry air at constant pressure ($1005 J/kgK$), and q_l is the liquid water mixing ratio (calculated earlier for the total water mixing ratio computation).

Conserved quantities for each data point enabled us to see the distribution of both total water and liquid potential temperature vertically in the atmosphere. Profiles of these variables are shown in Figures 3.2 through 3.11. Due to the high frequency of data points, many

of the following plots are color coded according to density of data points on any given area of a plot, in two dimensional histogram plots. The domain has been broken up into boxes; warm colors represent large density of points in each box, and cool colors represent small density of points in each box. Total water profiles are shown in Figures 3.2 through 3.6, and liquid water potential temperature profiles are in shown in Figures 3.7 through 3.11.

3.3 Mixing Fraction

Our conserved variables, q_t and Θ_l,were used to calculate a third conserved quantity, called mixing fraction, for each point along the flight path. Mixing fraction is defined as the fractional amount of one pure fluid mixed into a parcel of another pure fluid during a mixing process. In this case, mixing fraction is defined to be the fractional amount of free tropospheric air mixed into a parcel of purely cloudy air. Values of mixing fraction range between 0 and 1. Using our method, a mixing fraction of 0 means no free tropospheric air has been mixed into the parcel of cloudy air, and therefore represents a parcel of completely pure cloud layer air; conversely, a mixing fraction of 1 represents a parcel comprised completely of free tropospheric air.

Following the methodology of vanZanten and Duynkerke (2002), mixing fraction was computed using the following equation:

$$\chi = \frac{\delta q_t}{\Delta q_t} \tag{3.6}$$

where

$$\delta q_t = q_{tm} - \overline{q_{t2}}, \tag{3.7}$$

and

$$\Delta q_t = \overline{q_{t1}} - \overline{q_{t2}}. \tag{3.8}$$

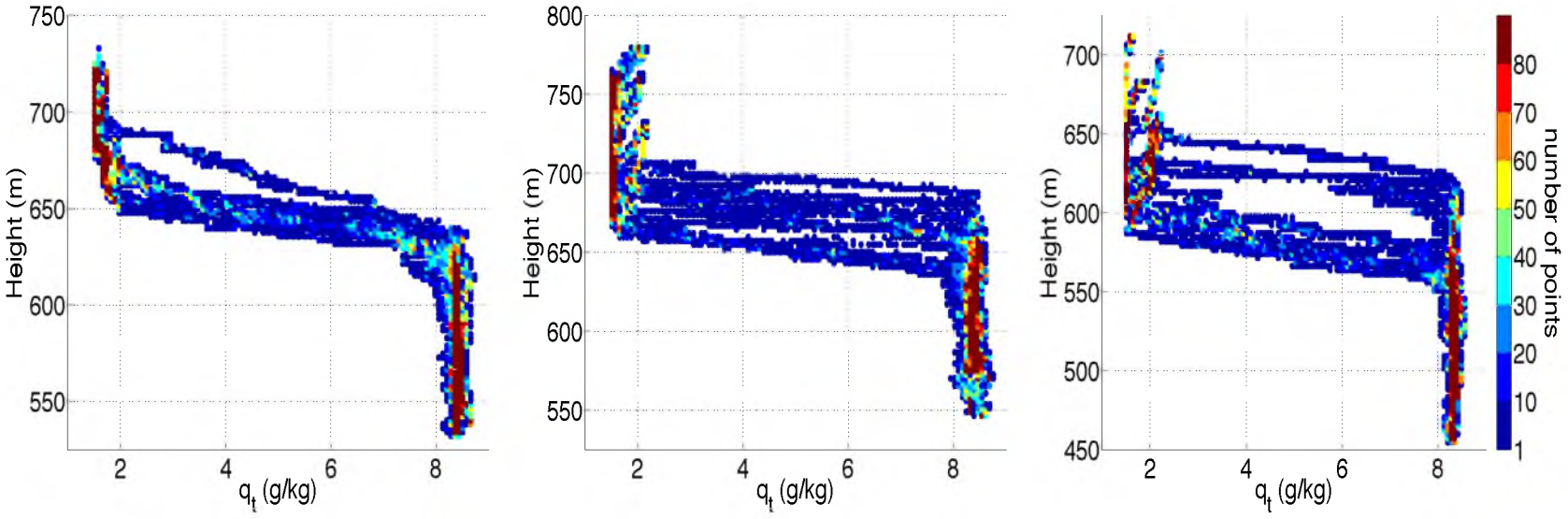

Figure 3.2: Total water profiles for all three pods of RF10, a daytime flight.

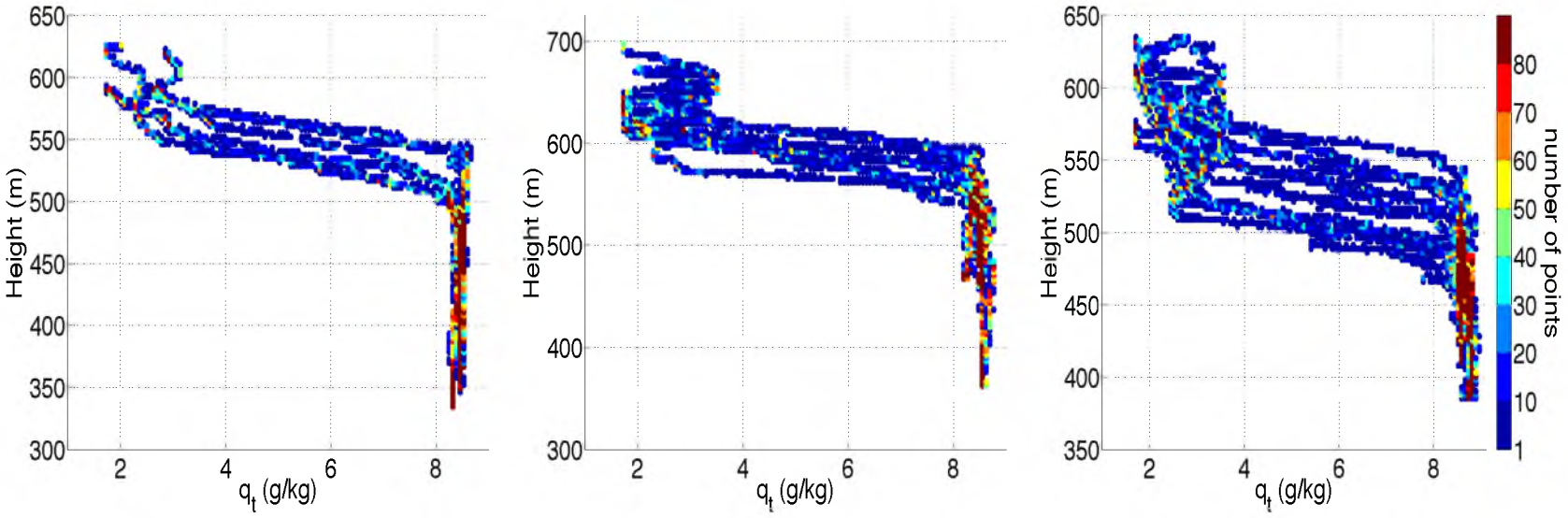

Figure 3.3: Total water profiles for three pods of RF11, an evening flight with overall low cloud amount.

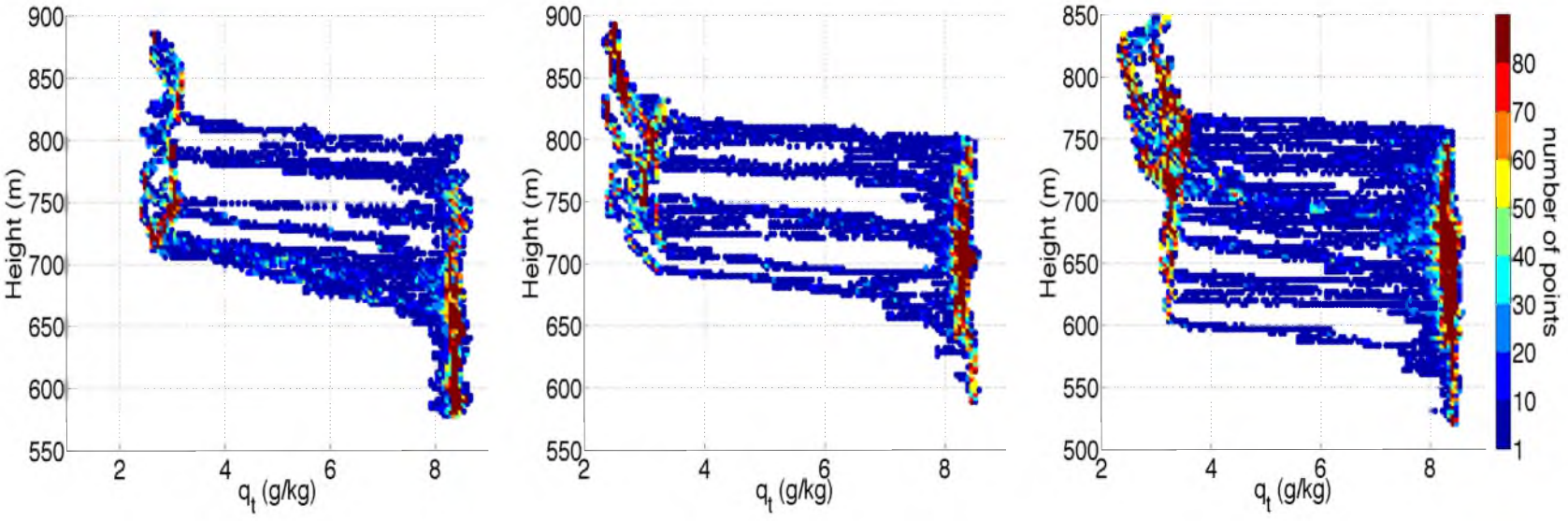

Figure 3.4: Total water profiles for all three pods of RF12, an evening flight with large variation in cloud top height.

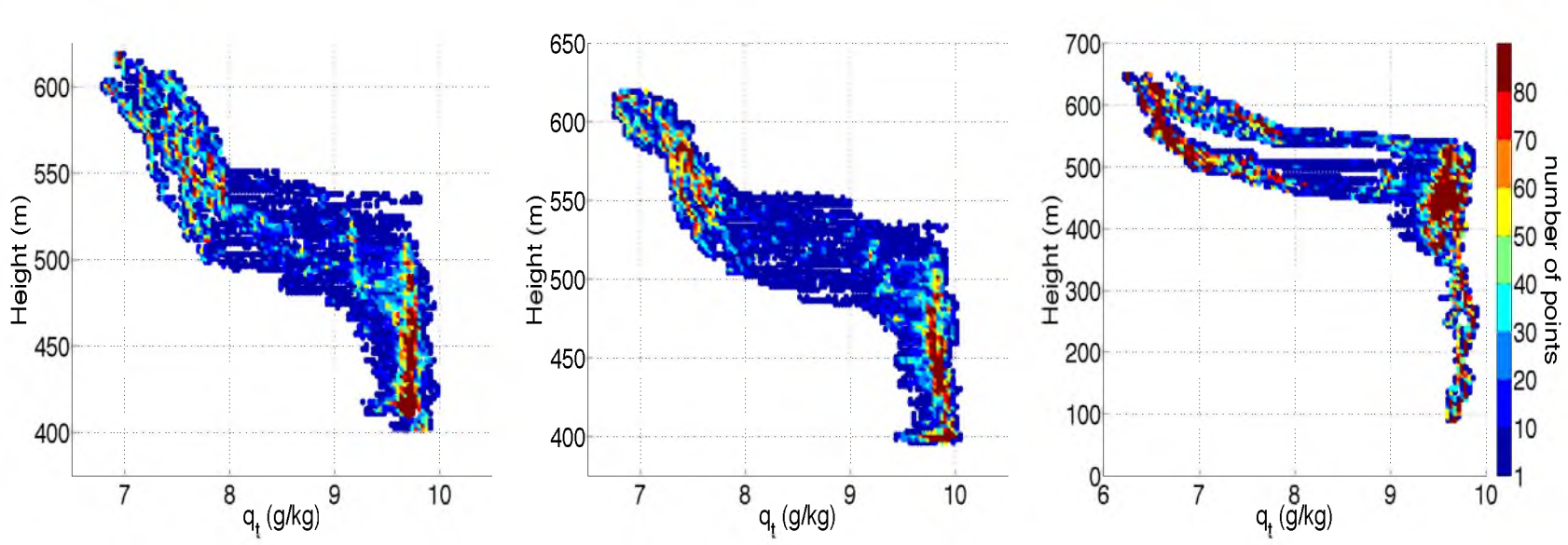

Figure 3.5: Total water profiles for all three pods of RF14, an evening flight with an observed moist overlying layer.

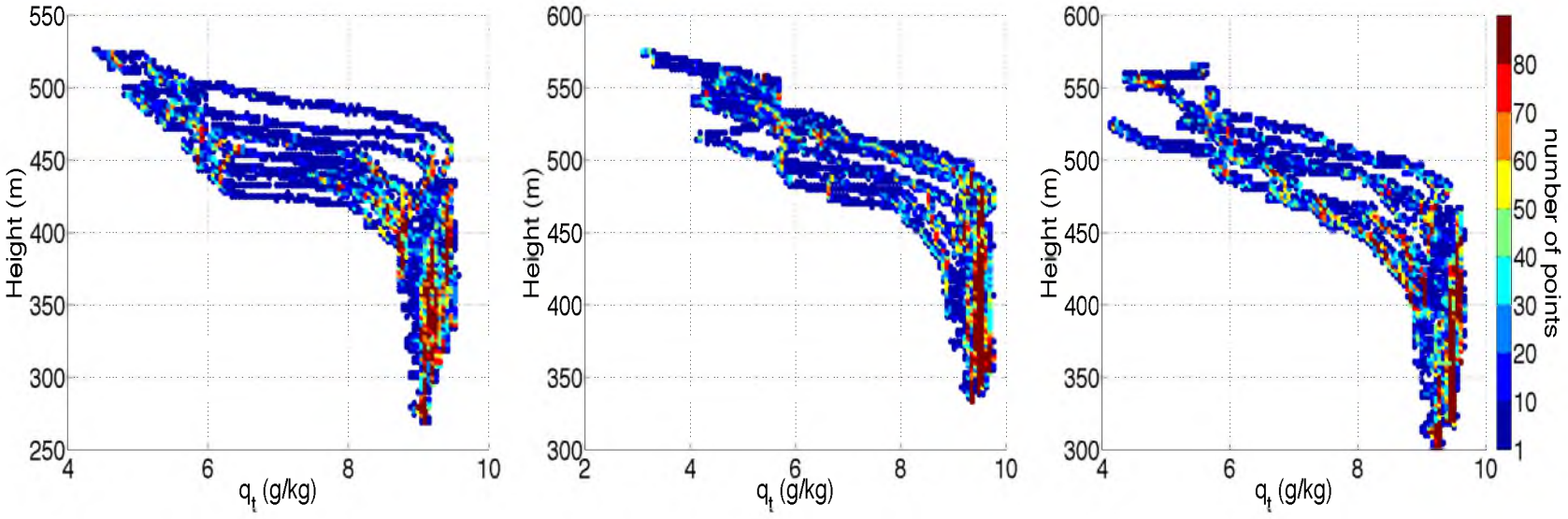

Figure 3.6: Total water profiles for all three pods of RF16, a daytime flight.

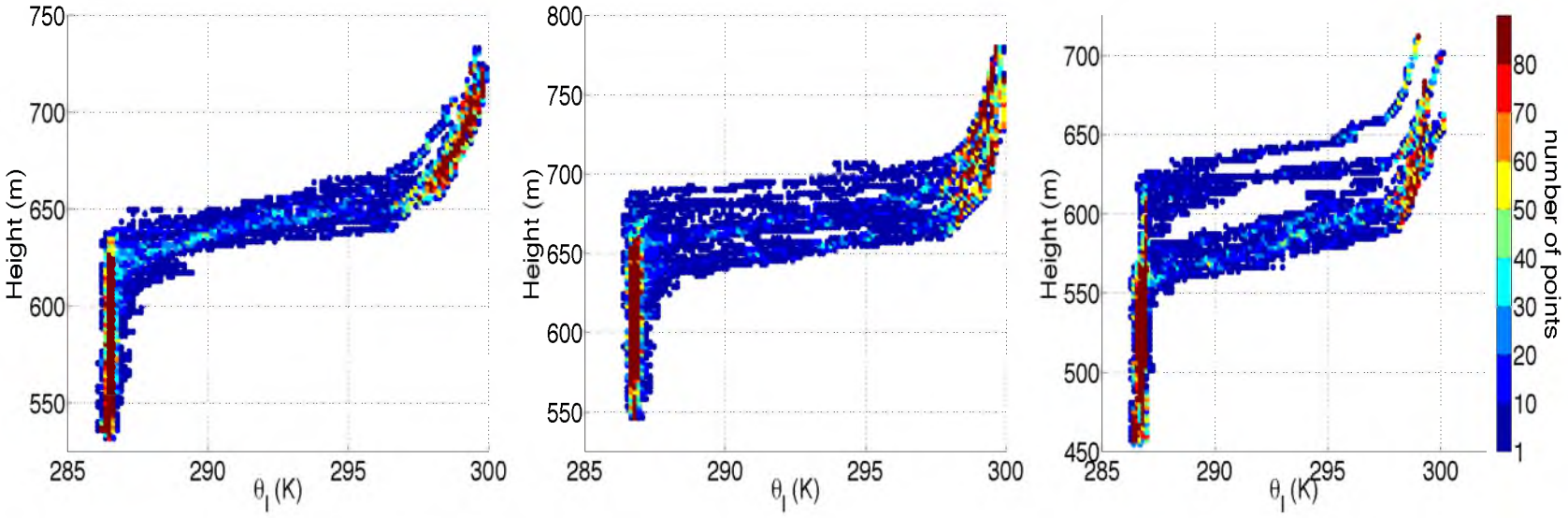

Figure 3.7: Liquid water potential temperature profiles for all three pods of RF10, a daytime flight.

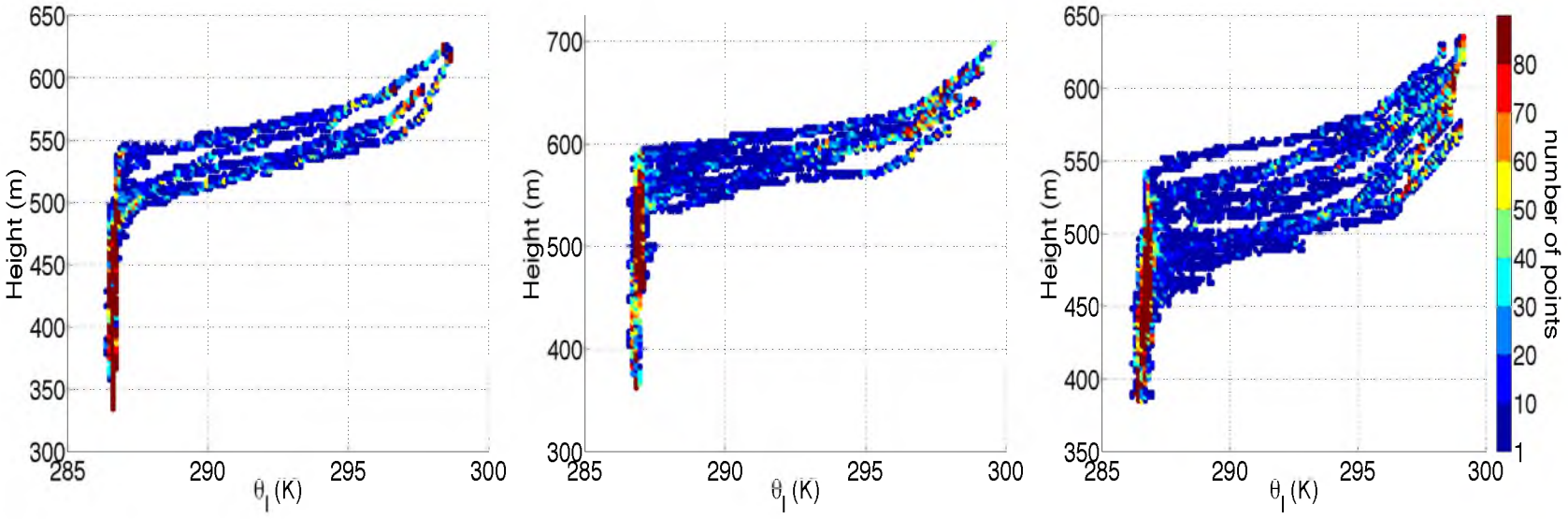

Figure 3.8: Liquid water potential temperature profiles for three pods of RF11, an evening flight with overall low cloud amount.

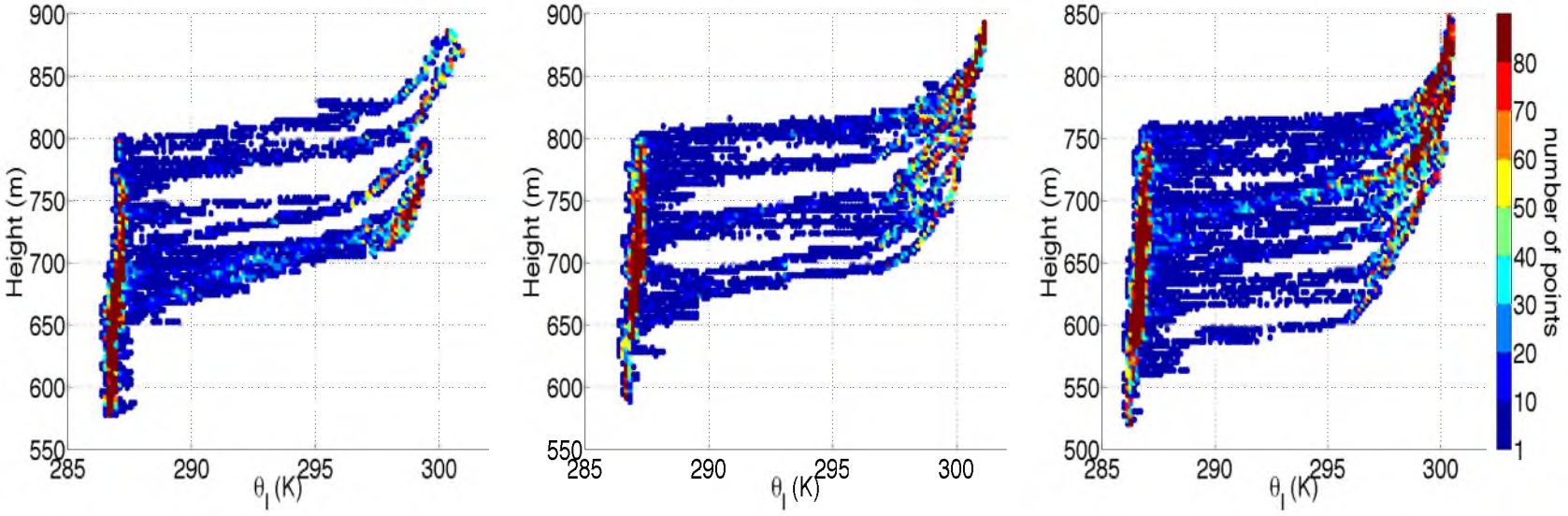

Figure 3.9: Liquid water potential temperature profiles for all three pods of RF12, an evening flight with large variation in cloudtop height.

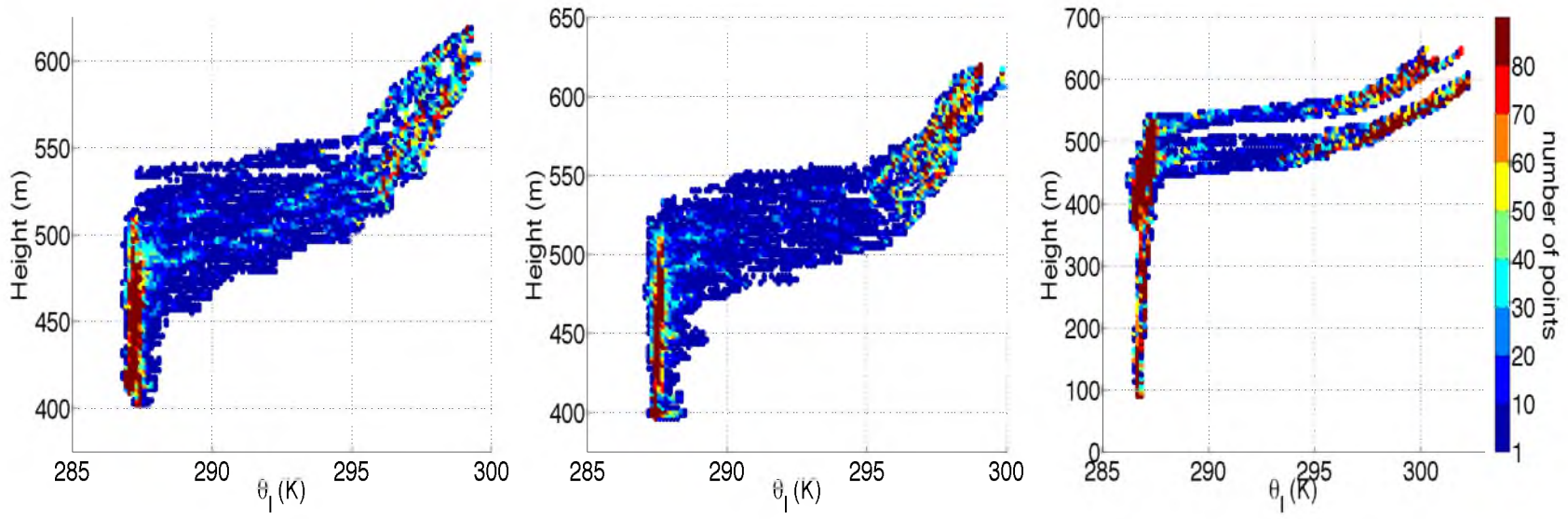

Figure 3.10: Liquid water potential temperature profiles for all three pods of RF14, an evening flight with an observed moist overlying layer.

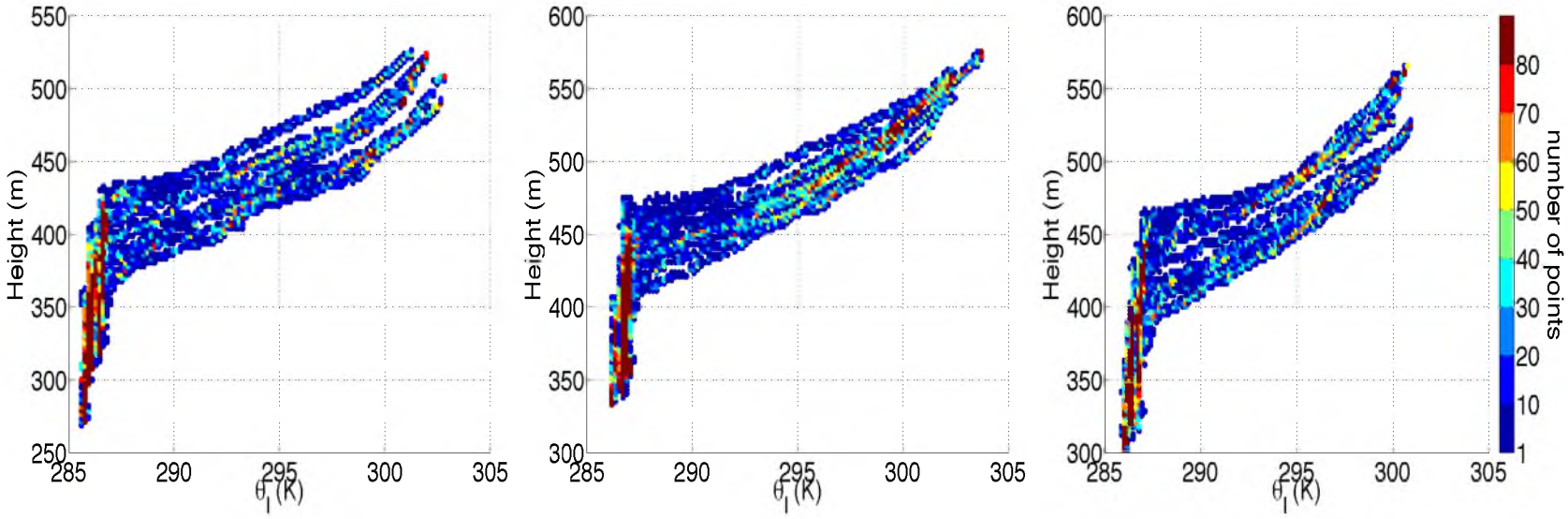

Figure 3.11: Liquid water potential temperature profiles for all three pods of RF16, a daytime flight.

In the equations above, q_t represents total water mixing ratio, a subscript of 1 represents a value characteristic of the free troposphere, a subscript of 2 represents a value characteristic of the cloudy mixed layer, and an overbar indicates an average value over the given layer (cloudy mixed layer or free troposphere). In other words, Δq_t is the jump in total water mixing ratio across the inversion at cloud top, and δq_t is the local fluctuation in total water mixing ratio along the flight path.

To estimate layer average values for the cloudy layer and for the overlying free troposphere, we used a mixing line analysis, as described in Chapter 1. To plot these mixing lines, conserved variables q_t and Θ_l were plotted against each other. Mixing lines for our five selected flights are shown in Figures 3.12 through 3.16, also in color coded two dimensional histogram plots.

As explained in Chapter 1, the endpoints of these mixing lines give the state prior to mixing of two thermodynamically distinct and pure states. In this case, the two pure, distinct types of air prior to mixing were defined as air from the overlying free troposphere, and air from the cloudy mixed layer. Therefore, for our mixing fraction equation, to make a good approximation for an average total water mixing ratio over the cloud layer, we estimated an upper "endpoint" for our mixing lines, while we estimated a lower "endpoint" for the mixing lines to provide an average total water mixing ratio value for the overlying free troposphere. These average endpoint values, as well as average cloud top pressure are given in Table 3.1.

Calculating mixing fraction for each point along the flight path allowed for the region near the top of the mixed layer to be plotted in a new way, now characterized by mixing fraction. Values with a mixing fraction of at least 0.9 were taken to be values characteristic of pure free tropospheric air, and are colored red; values with a mixing fraction of 0.1 or less were taken to be characteristic of pure cloudy mixed layer air, and are colored blue; finally, points with mixing fraction values between these two extremes were taken to be characteristic of parcels in the midst of mixing processes, and are colored black. The re-

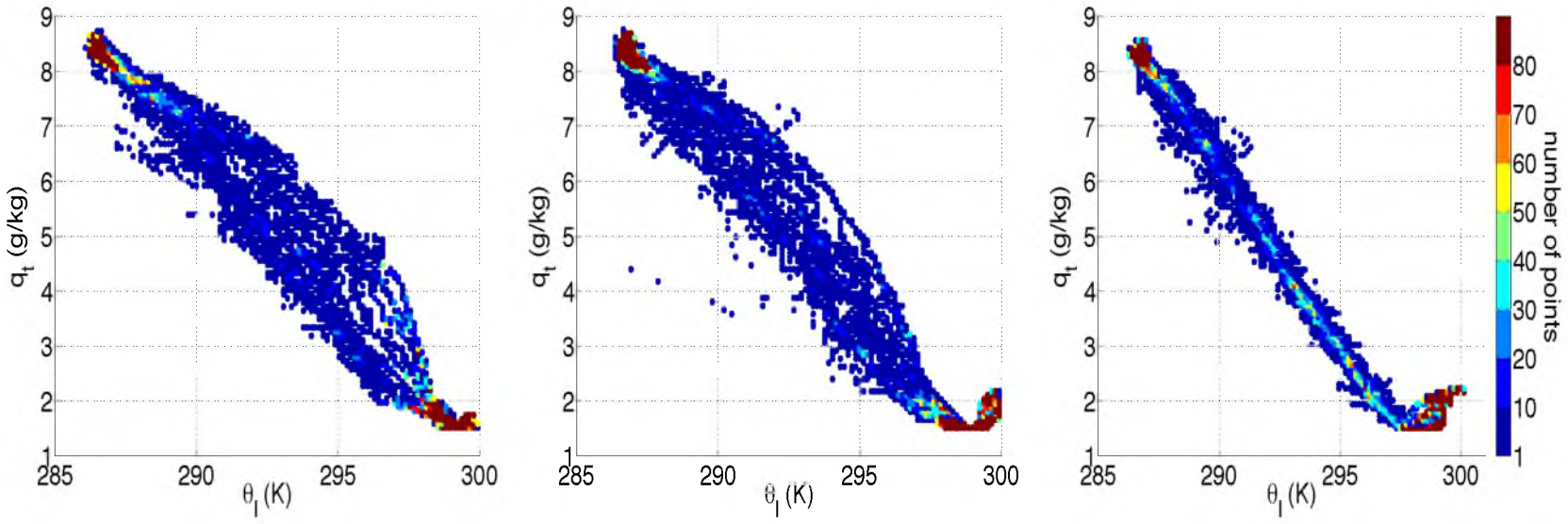

Figure 3.12: Mixing lines for all three pods of RF10, a daytime flight with significant jumps in thermodynamic properties across the inversion at cloud top.

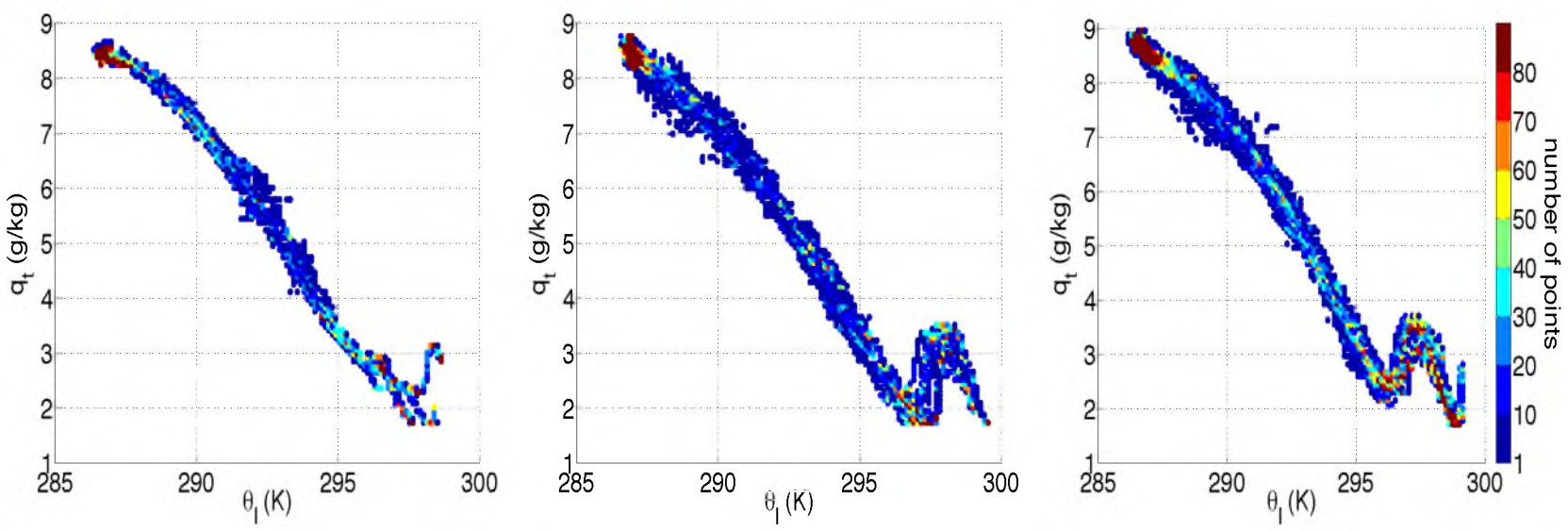

Figure 3.13: Mixing lines for three pods of RF11, an evening flight with overall low cloud amount.

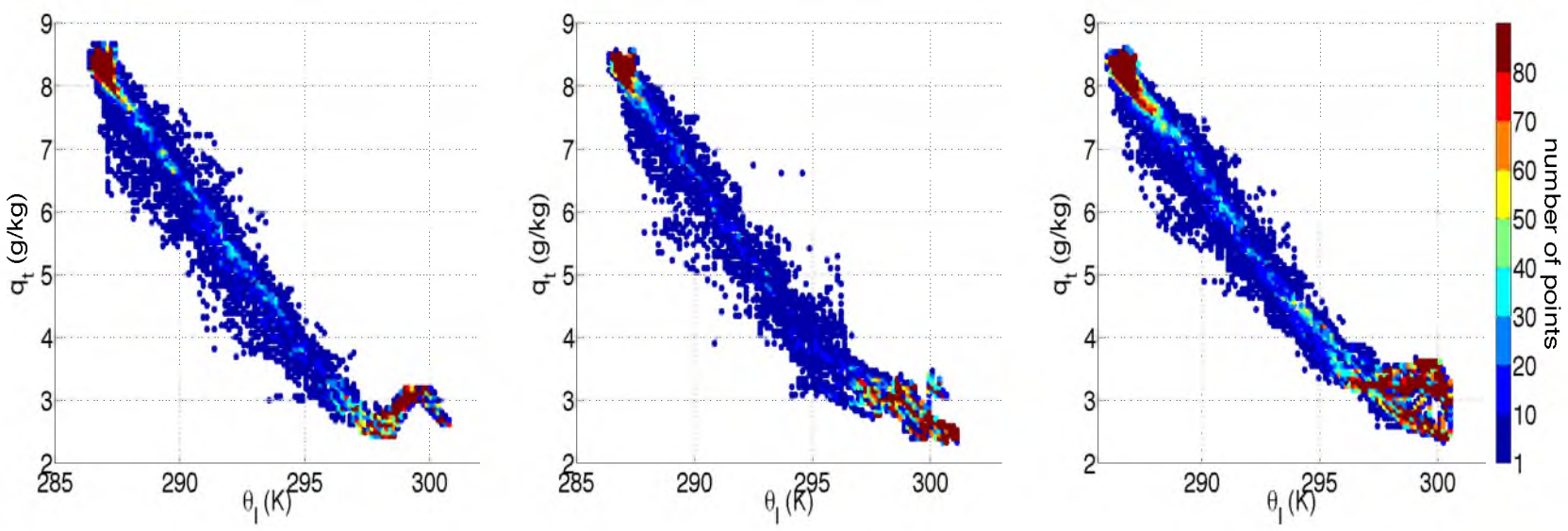

Figure 3.14: Mixing lines for all three pods of RF12, an evening flight with large variation in cloudtop height.

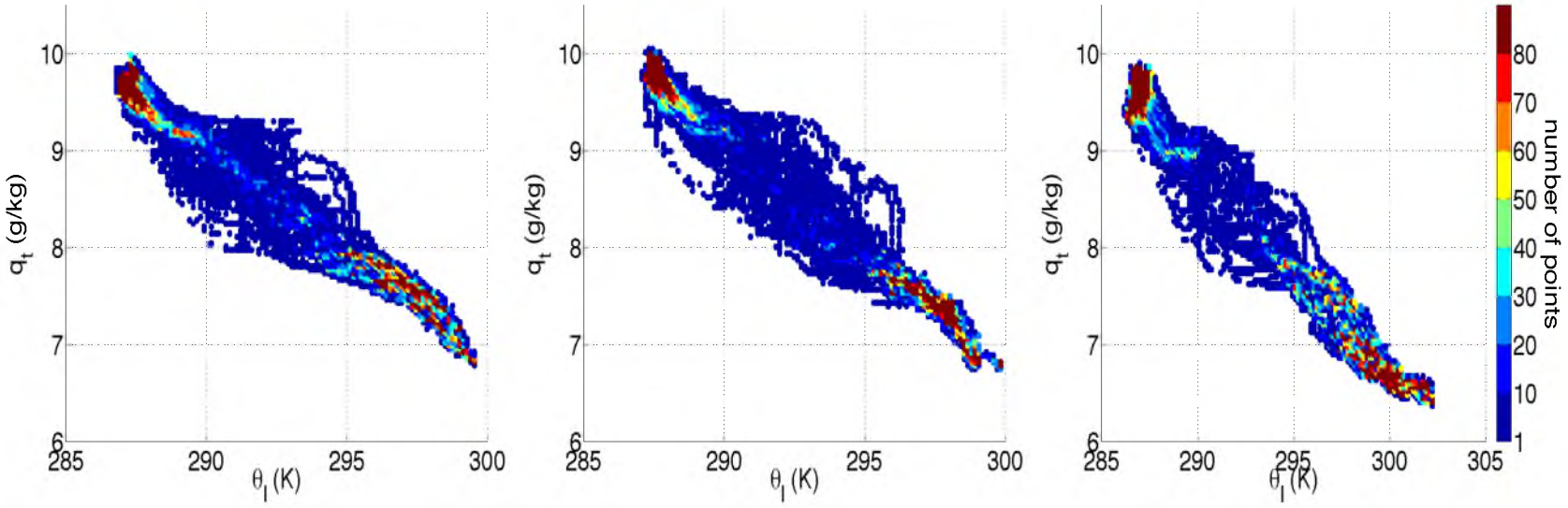

Figure 3.15: Mixing lines for all three pods of RF14, an evening flight with an observed moist overlying layer.

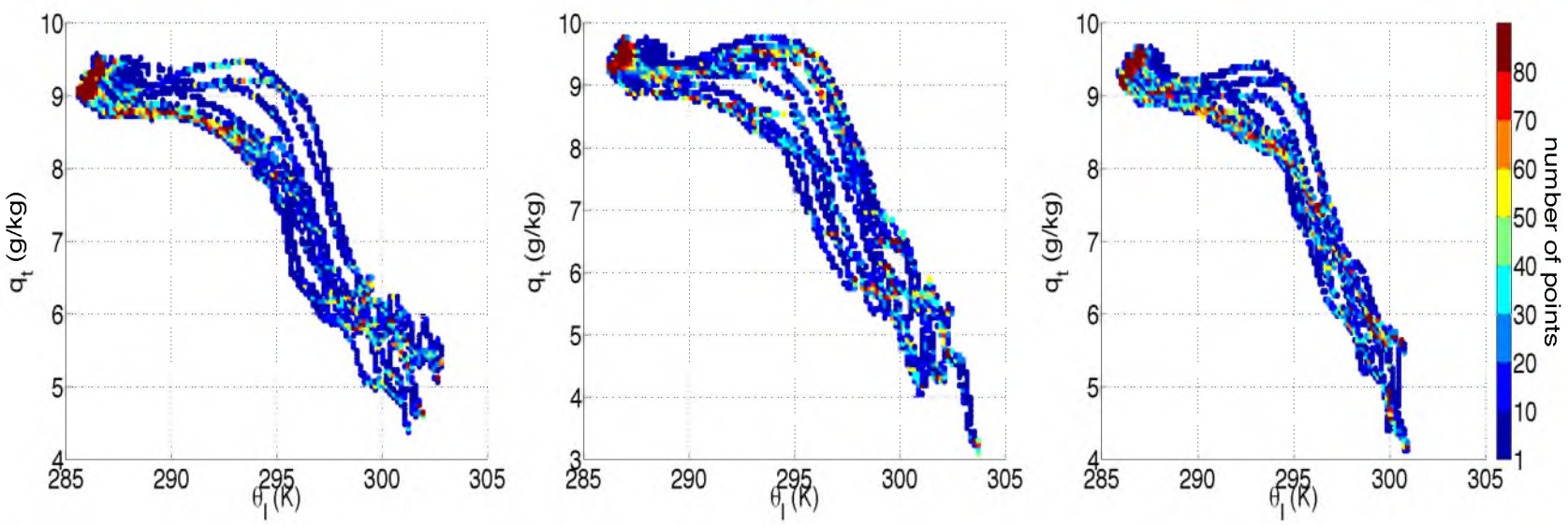

Figure 3.16: Mixing lines for all three pods of RF16, a daytime flight.

Table 3.1: Average total water mixing ratio and liquid water potential temperature values for pure cloudy mixed layer air and pure free tropospheric air for RF10, RF11, RF12, RF14, and RF16, as well as average cloud top pressures.

Flight No.	$q_t(g/kg)$		$\theta_l(K)$		Avg. CT Pressure (hPa)
	$\chi = 1$	$\chi = 0$	$\chi = 1$	$\chi = 0$	
RF10 (daytime)					
pod 1	1.90	8.40	298.6	286.4	942.6
pod 2	1.70	8.40	298.4	286.7	940.4
pod 3	1.60	8.35	297.4	286.7	951.7
RF11 (evening)					
pod 1	2.90	8.50	295.9	286.7	959.4
pod 2	1.70	8.40	297.1	286.9	949.7
pod 3	1.80	8.60	296.8	286.8	954.0
pod 4	2.40	8.80	296.2	286.6	959.4
RF12 (evening)					
pod 1	2.70	8.40	297.1	286.9	933.7
pod 2	3.30	8.30	296.4	286.8	928.5
pod 3	3.20	8.40	297.0	286.4	935.0
RF14 (evening)					
pod 1	7.50	9.70	297.7	287.3	950.9
pod 2	7.40	9.80	297.8	287.6	955.2
pod 3	6.60	9.70	299.9	287.4	954.7
RF16 (daytime)					
pod 1	5.80	9.40	299.2	286.8	967.1
pod 2	5.80	9.60	299.4	286.8	961.5
pod 3	5.80	9.40	299.0	286.8	964.2

sult, for all of our analyzed flights, was a clearly defined layer of black points, bordered on the top by red points (free troposphere), and on the bottom by blue points (cloudy mixed layer). This result indicates a clearly defined layer of mixing between two pure states of the atmosphere. Examples of this result are shown in Figures 3.17 and 3.18, for all three pods from RF10 (a daytime flight) and RF12 (an evening flight).

3.4 Defining the Extent of the EIL

To define top (the interface between the EIL and the free troposphere) and bottom (the interface between the EIL and cloudy mixed layer) boundaries for the EIL, an algorithm was designed to detect each interface in the mixing fraction time series between cloud layer values and EIL values, and between free tropospheric values and EIL values:

$$detect = (\chi_i - \chi_0) * (\chi_{i-1} - \chi_0) \tag{3.9}$$

where χ_0 is our threshold value for one of the two pure mixing states (0.1 or 0.9 – this algorithm was used to detect interfaces at both boundaries), and χ_{i-1} and χ_i are consecutive values in the mixing fraction time series. Here, if consecutive elements in the mixing fraction time series were on opposite sides of a threshold, one factor would be a positive value while the other factor would be a negative value, yielding an overall negative value for our "detect" algorithm. Likewise, two consecutive elements in the mixing fraction time series on the same side of a threshold would yield a positive result.

Mixing fraction values for all data points were run through this algorithm, and then height and time data for negative "detect" values were extracted from the corresponding height and time data sets. These interfaces were marked with circles in the flight path. Figure 3.19 shows an example of one pod from a daytime flight and one pod from an evening flight with detected interfaces in magenta for the boundary between the cloudy layer and the layer of mixing, and in black circles for detected interfaces between the layer of mixing and the overlying free troposphere. Figure 3.20 shows a closeup of one porpoise

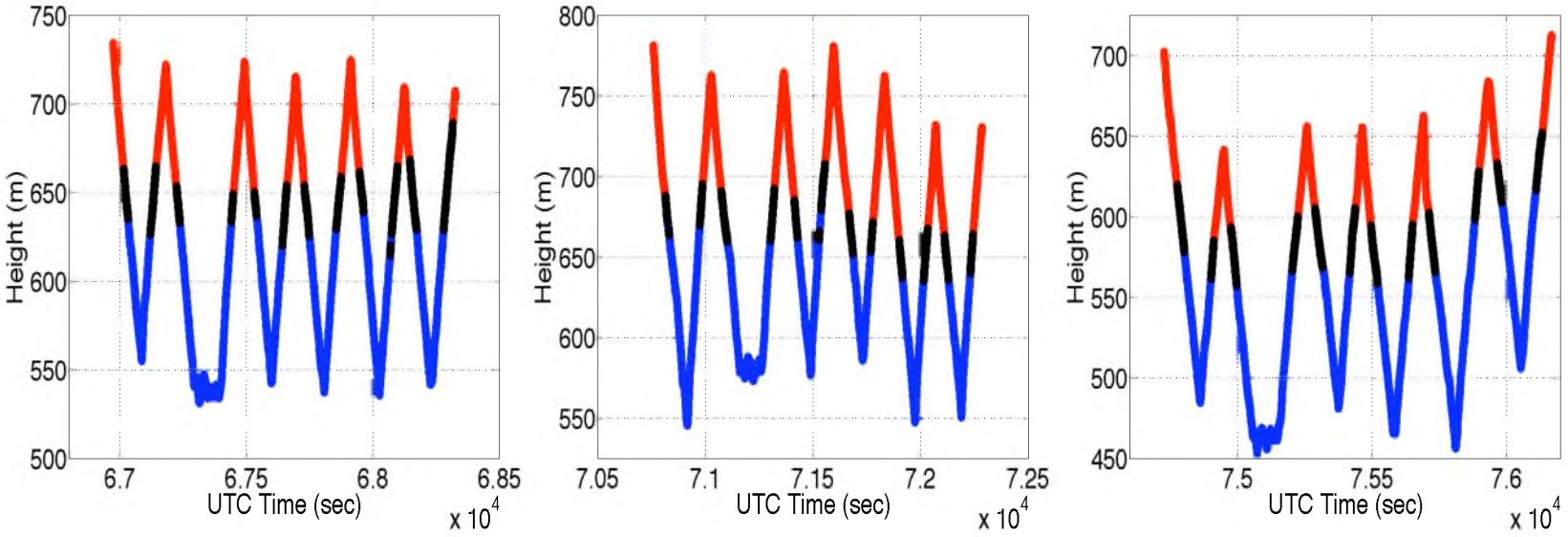

Figure 3.17: The flight path for the three pods from RF10, color-coded according to mixing fraction. Red points represent $\chi \geq 0.9$ (pure free tropospheric air), blue points represent $\chi \leq 0.1$ (pure cloud layer air), and black points represent $0.1 < \chi < 0.9$ (values in between the two pure states, indicative of mixing).

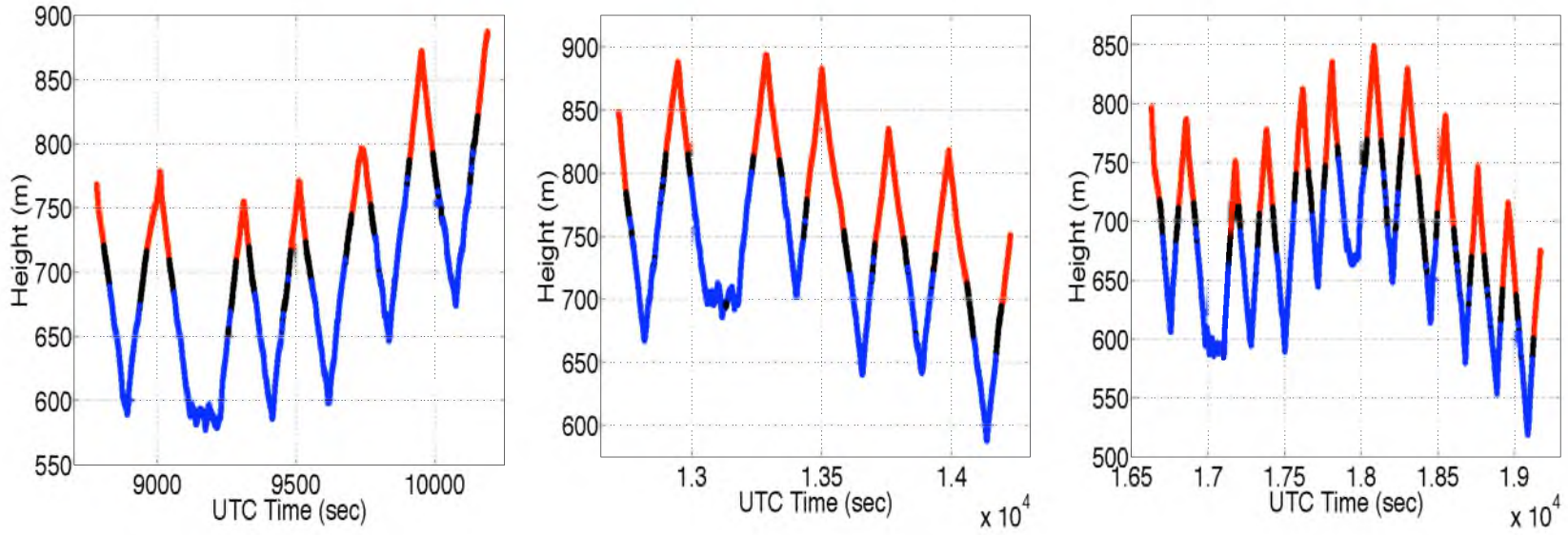

Figure 3.18: The flight path for the three pods from RF12, color-coded according to mixing fraction. Red points represent $\chi \geq 0.9$ (pure free tropospheric air), blue points represent $\chi \leq 0.1$ (pure cloud layer air), and black points represent $0.1 < \chi < 0.9$ (values in between the two pure states, indicative of mixing).

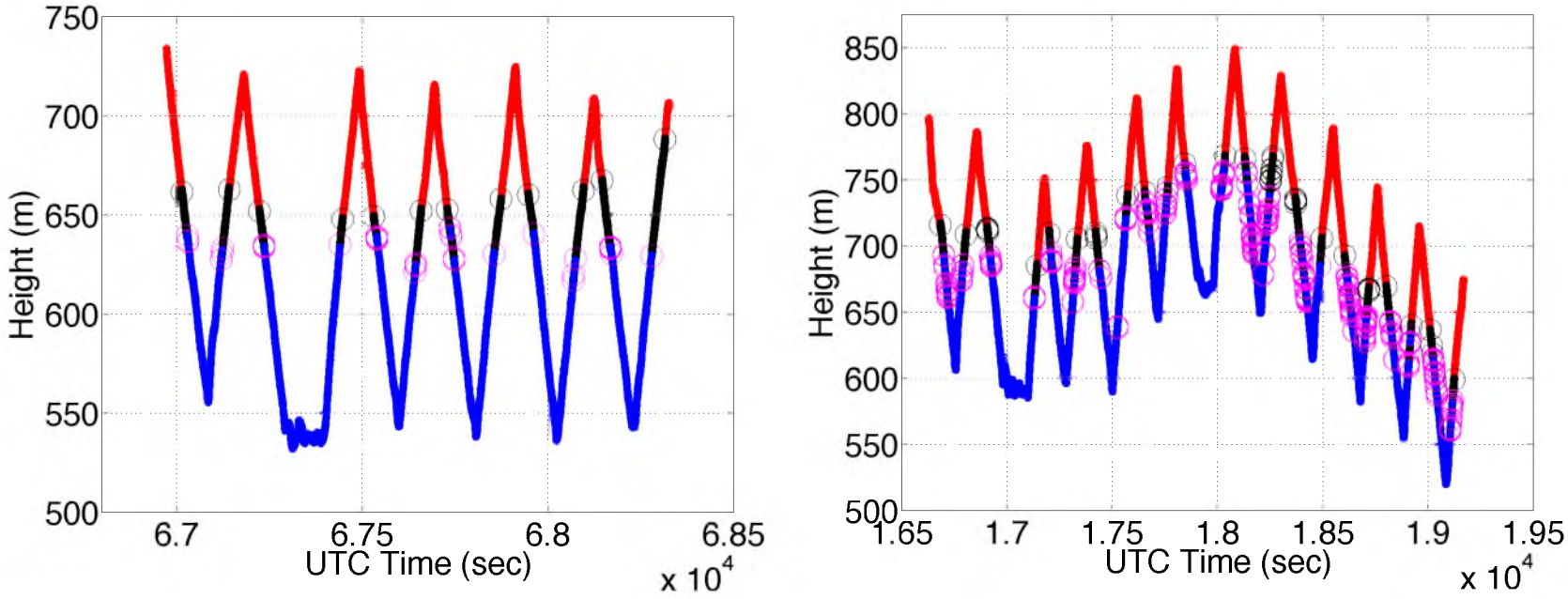

Figure 3.19: Interfaces between mixing states, for one pod of a daytime flight, and for one pod of an evening flight. Mixing fraction values characteristic of pure cloud layer air are in blue, values characteristic of mixing are in black, and values characteristic of pure free tropospheric air are in red. Interfaces between the cloud layer and the EIL are circled in magenta; interfaces between the EIL and the free troposphere are circled in black.

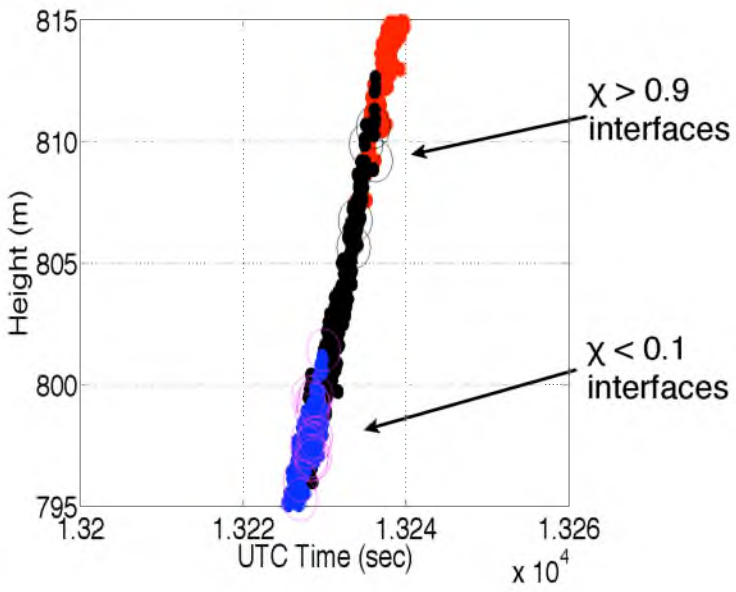

Figure 3.20: Close-up view of one porpoise of RF12, showing detected interfaces near top and bottom boundaries of the EIL.

from RF12 to show variability of mixing fraction along the flight path near cloudy mixed layer and free troposphere interfaces, along with detected interfaces between mixing and pure states.

Next, the mean, median, maximum, and minimum height were calculated for each porpoise's set of interfaces. Finally, for each interface within each porpoise, the approximate boundaries between layers were defined at the mean altitudes of these detected interfaces. This gave a single, average value for the boundaries and extent of the layer of mixing between the cloudy mixed layer and the free troposphere. We took this layer of mixing, now defined by mean detected interfaces, to be our best approximation for the location and extent of the EIL.

3.5 Comprehensive EIL Plots

Calculated values of mixing fraction, along with our approximate average heights for the extent of the EIL, were used to create a comprehensive sketch of the characteristics and structure of the layer of mixing near cloud top for all five flights from POST that were selected for analysis. These comprehensive diagrams for all pods of the selected five flights are shown in Figures 3.21 through 3.25.

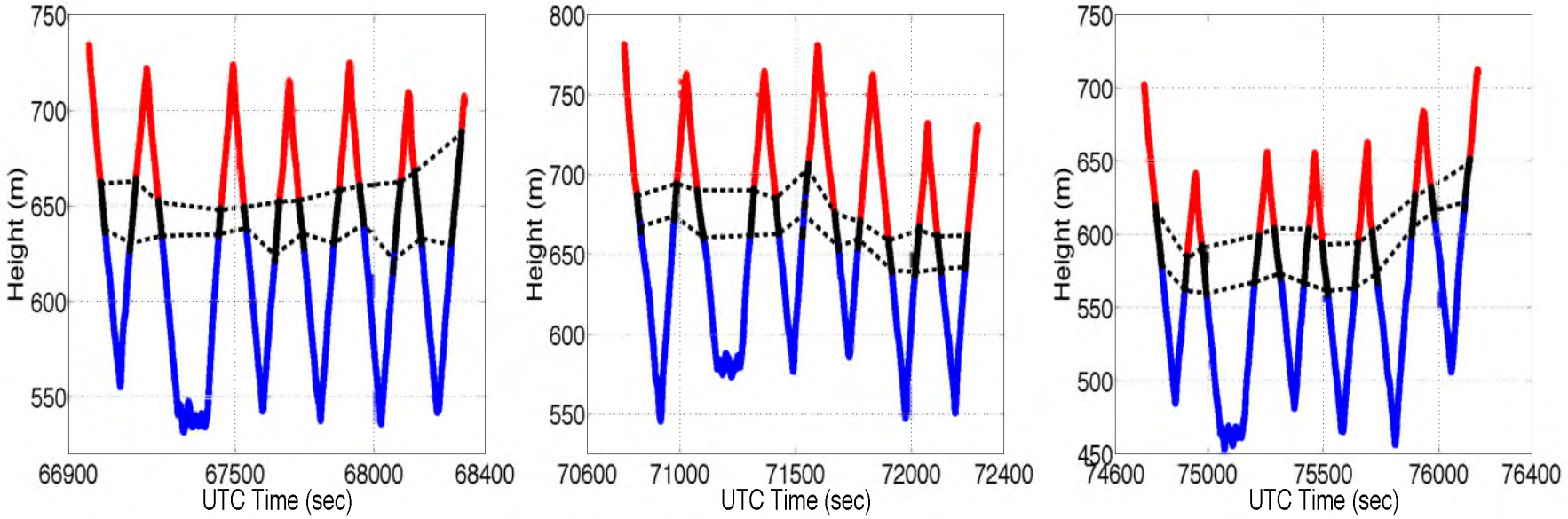

Figure 3.21: Approximate location and extent of the EIL plotted over mixing fraction values for all pods of RF10. EIL boundaries are marked with a black dashed line, mixing fraction values characteristic of pure free tropospheric air are in red, mixing fraction values characteristic of pure cloud layer air are in blue, and mixing fraction values characteristic of the EIL are in black.

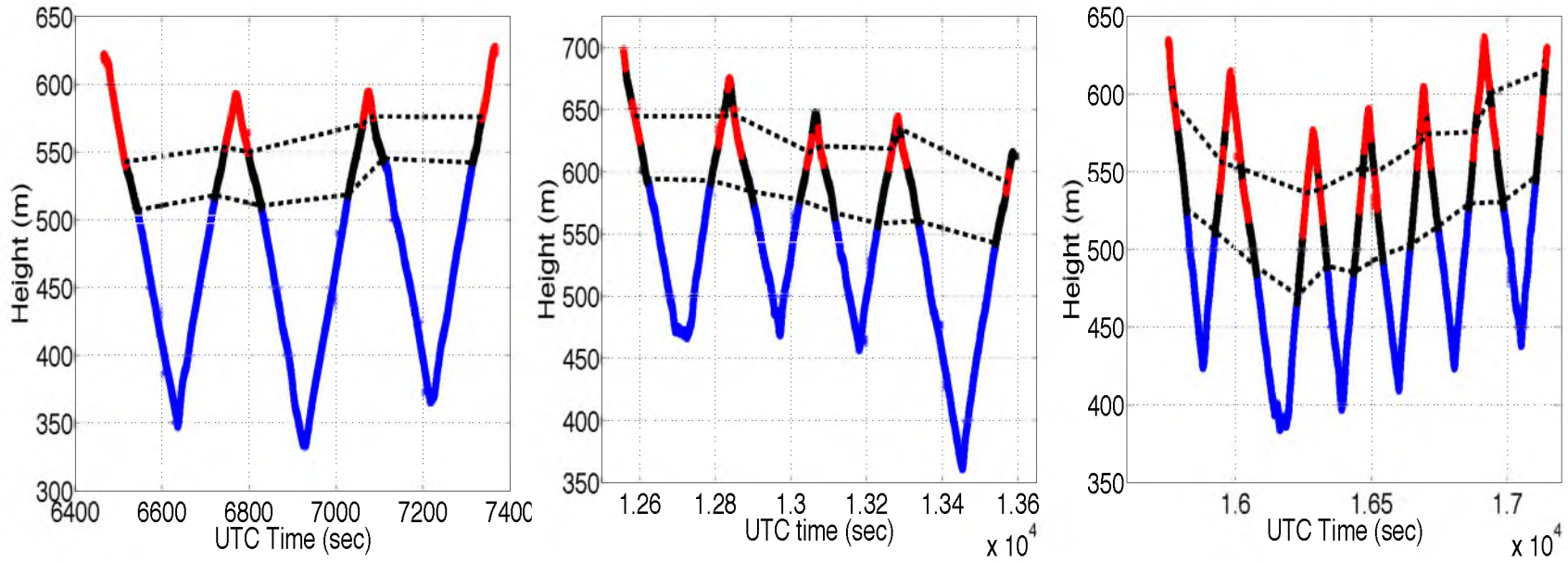

Figure 3.22: Location and extent of our estimated EIL, with mixing fraction color coded for all pods of RF11. Black dashed lines mark EIL boundaries, red areas represent values characteristic of the free troposphere, blue areas represent values characteristic of the cloudy boundary layer, and black areas represent values characteristic of mixing within the EIL.

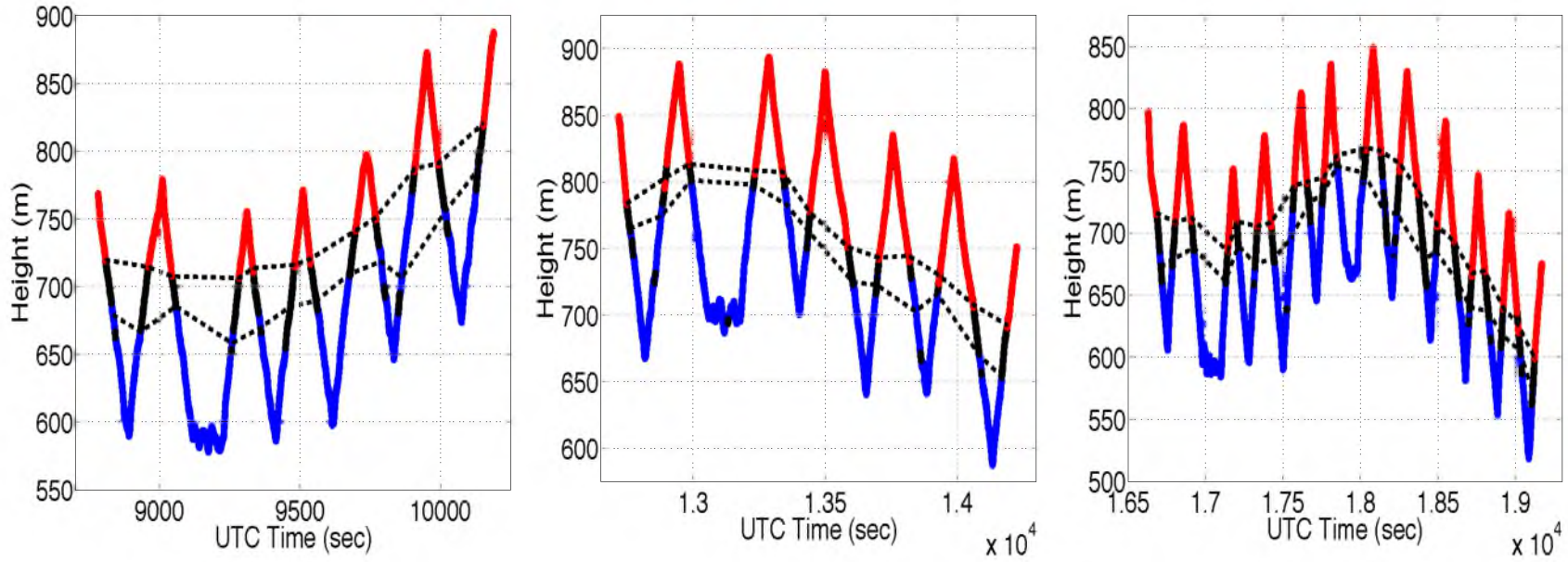

Figure 3.23: For RF12, location and extent of the EIL marked with black dashed lines. Values characteristic of the free troposphere are color-coded in red, values characteristic of the cloudy boundary layer are color-coded in blue, and values characteristic of mixing (and hence the EIL) are color-coded in black.

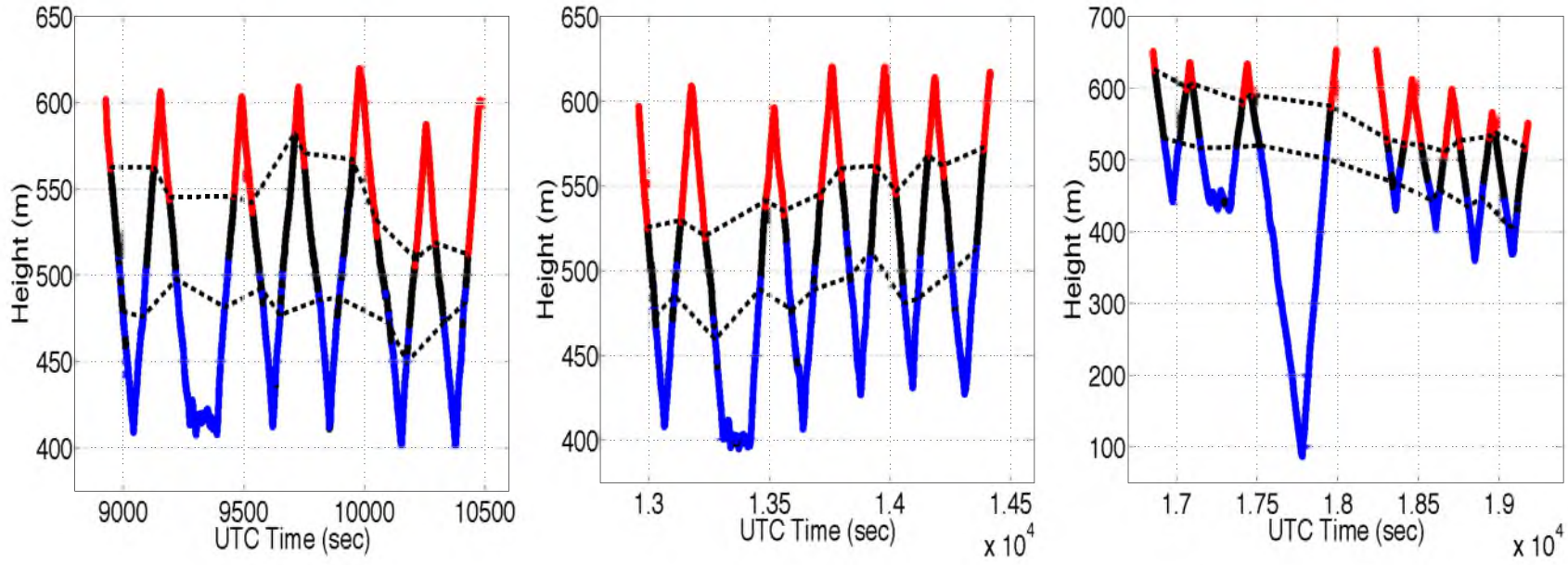

Figure 3.24: Approximate EIL boundaries, marked by a black dotted line, plotted on the vertical flight path for each pod of RF14. Free tropospheric values are color-coded in red, cloudy boundary layer values are color coded in blue, and EIL mixing values are color coded in black.

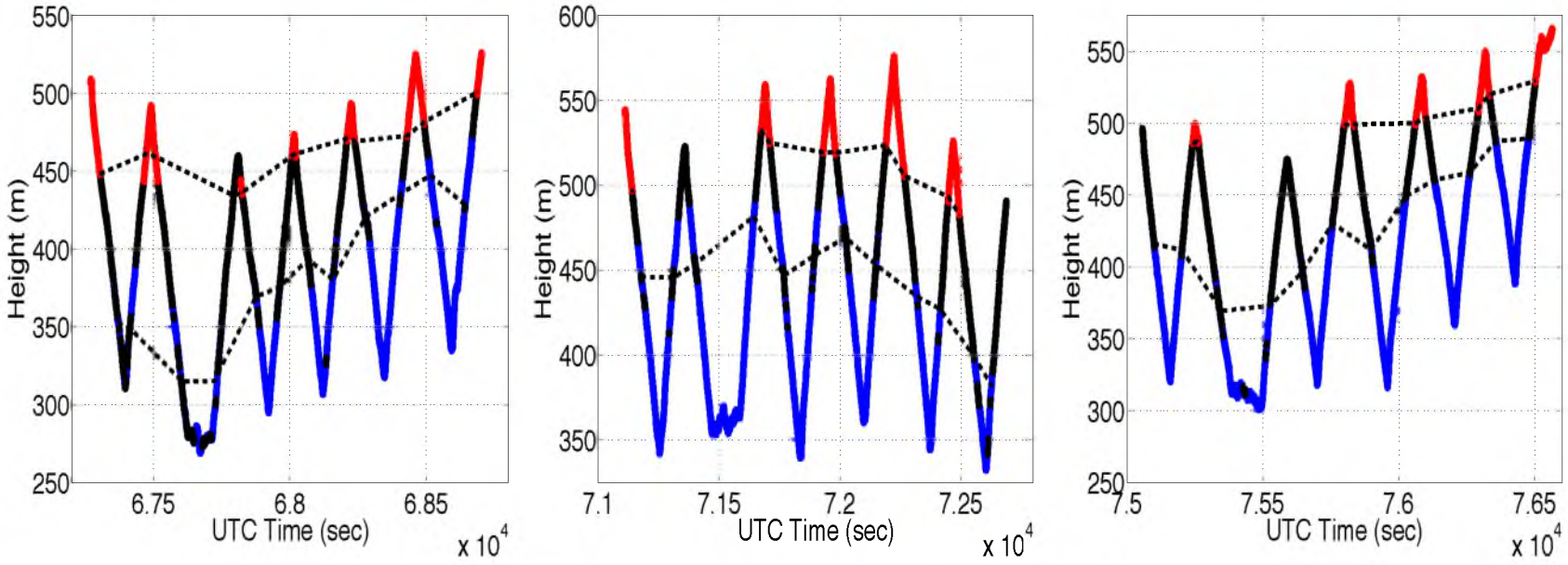

Figure 3.25: The EIL's approximate location and extent for RF16, plotted with dashed black lines. The EIL is superimposed on the vertical flight path for each pod of RF16, with free tropospheric values colored red, cloudy boundary layer values colored blue, and EIL mixing values colored in black.

CHAPTER 4

EIL STATISTICS AND STUDIES

Approximate estimations of the location and extent of the EIL as defined by mixing fraction provided a unique opportunity to look at the evolution and characteristics of the EIL during daytime and evening flights. The following sections will detail these analyses of statistics and behavior of the EIL during the five POST flights analyzed in the previous chapter.

4.1 Thickness of the EIL

Thickness and extent of the EIL at the top of marine boundary layers has remained relatively uncertain due to the methods by which the EIL is defined, and due to limited data collected during observational studies. Estimates of EIL thickness included in this section are based on EIL boundaries calculated from mixing fraction values, which were computed using the high rate data from POST.

To calculate EIL thickness over the course of a flight, the EIL bottom height was subtracted from the EIL top height for each porpoise. Those thicknesses were then averaged over all three pods to give our best estimate of EIL thickness during a given flight. Histograms, shown in Figures 4.1 through 4.5, show the frequency of EIL thickness including all porpoises for Flights 10, 11, 12, 14, and 16. Each "location" refers to a single porpoise passing through the EIL during a given flight.

These distributions of EIL thickness show that, for all five flights, EIL thicknesses of

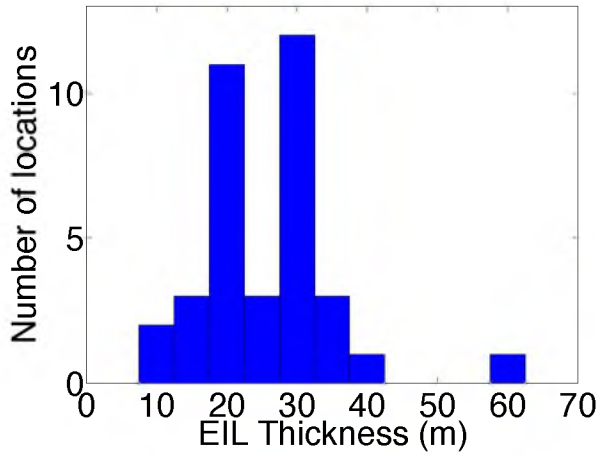

Figure 4.1: Frequency of EIL thickness as observed over all porpoising during RF10, a daytime flight."Locations" refer to porpoises passing through the EIL.

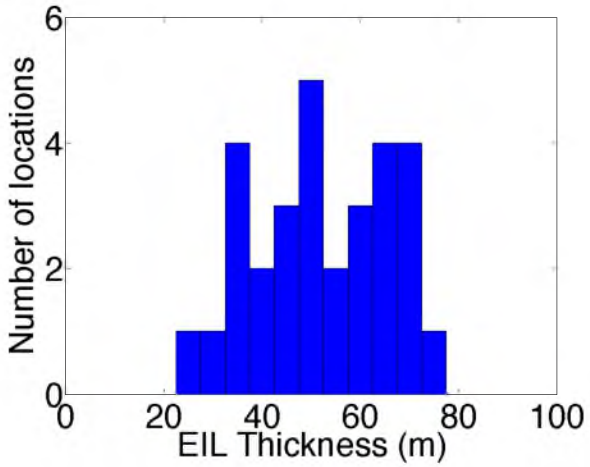

Figure 4.2: EIL thickness frequency when taken over all porpoising during RF11, an evening flight. "Locations" describe porpoises passing through the EIL.

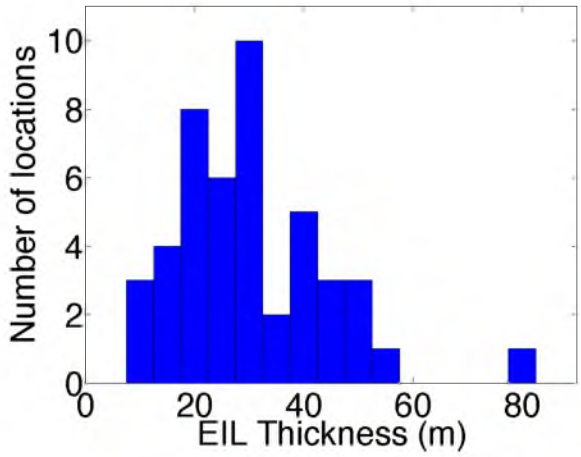

Figure 4.3: When including all porpoises of evening RF12, frequency of EIL thickness values. "Locations" refer to porpoises through the EIL.

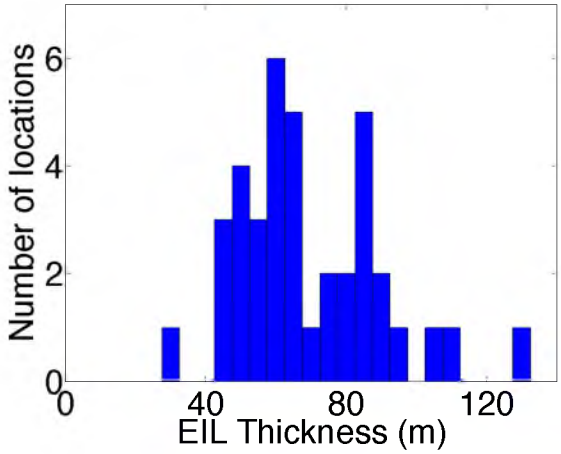

Figure 4.4: Thickness of the EIL when each porpoise ("location") through the EIL is taken into account for RF14, an evening flight.

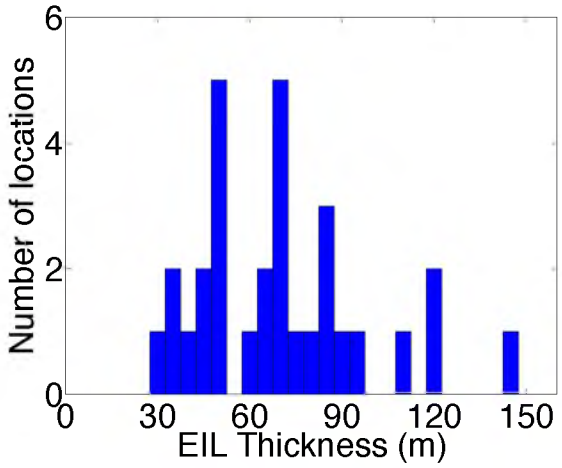

Figure 4.5: Frequency of EIL thickness values when all porpoises from RF16, a daytime flight, are taken into account. A"location" corresponds to a vertical porpoise through the EIL.

several tens of meters are most common. While there are a few instances of extremely thick EILs, they are much less common, and there is only one instance of an especially thin EIL under 10 meters using our mixing fraction technique for defining the EIL. Statistics for each flight regarding EIL thickness are shown in Table 4.1, and flight averages for EIL thickness are shown in Table 4.2.

Table 4.1: Average, maximum, and minimum EIL thickness for RF10, RF11, RF12, RF14, and RF16.

Flight	Avg. EIL Thick (m)	Max. EIL Thick (m)	Min. EIL Thick (m)
RF10 (daytime)	25.9	58.7	10.8
RF11 (evening)	30.4	74.6	26.5
RF12 (evening)	52.0	80.5	8.6
RF14 (evening)	69.6	130.5	28.4
RF16 (daytime)	70.5	144.5	32.4

Table 4.2: Flight averages of EIL thickness for RF10, RF11, RF12, RF14, and RF16.

Flight	Avg. EIL Thickness - Entire Flight (m)
RF10 (daytime)	31.8
RF11 (evening)	43.8
RF12 (evening)	47.0
RF14 (evening)	76.2
RF16 (daytime)	82.5

4.2 Lower Tropospheric Stability and the EIL

To test whether the EIL of California marine stratocumulus is dependent on local and large-scale stability of the atmosphere, a couple of different stability analyses were performed here to identify any observable relationships between EIL thickness and stability of the surrounding atmosphere. Our first approach involved using lower tropospheric stability (LTS) to diagnose the large-scale stability during POST missions. This stability measure is defined as

$$LTS = \Theta_{850hPa} - \Theta_{sfc}. \tag{4.10}$$

As the flight paths during the POST field campaign only extended up to around 900 hPa at the highest point, it was necessary to obtain potential temperature data for the LTS calculation from an outside source. For this, we used archived data from NCEP's Global Forecast System, which consists of 48-hour forecasts at 3-hourly intervals for 20 grid points off the coast of California, covering the entire domain of POST missions. Each grid point is located at an intersection of a line of latitude and a line of longitude. Furthermore, in the vertical, model output is given at 64 pressure levels, from the surface up through most of the atmosphere.

To specifically treat the flights that were chosen here, latitude and longitude data from each of the five flights were plotted onto a latitude-longitude grid. Next, a box about the size of a GCM grid box (one degree latitude by one degree longitude, or 110 kilometers

by 110 kilometers) was defined to be centered on the horizontal extent of the flight path. For the appropriate forecast time step, potential temperature data from the NCEP GFS forecasts were then interpolated to 1-hPa resolution in the vertical, and 0.2 degree latitude and longitude resolution in the horizontal. (This 0.2 degree resolution was defined in order to allow the box to be manipulated and approximately centered on the horizontal flightpath of each analyzed flight.) LTS was next calculated at each interpolated point within the box by taking the difference in potential temperature between the 1020-hPa (surface) level and the 850-hPa level. Finally, all LTS values in the box were averaged to give a mean LTS for that flight. These LTS calculations were plotted against EIL thickness (Δh) for each pod of each flight. The result is shown in Figure 4.6.

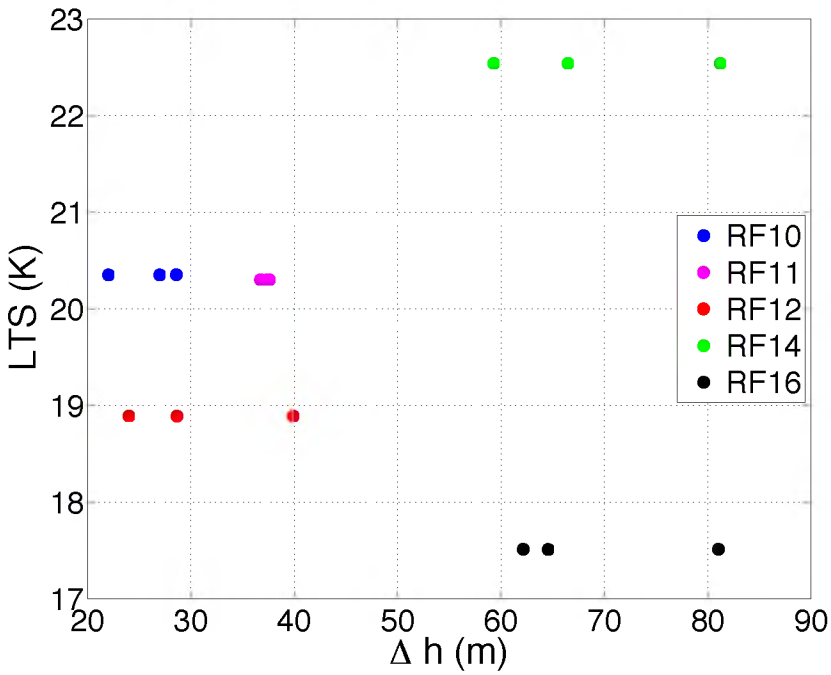

Figure 4.6: Correlation of LTS with EIL thickness for each pod of five POST flights, $R = 0.046$. RF10 and RF16 are daytime flights, and RF11, RF12, and RF14 are evening flights. Data points are color-coded to show values within individual flights; one value of LTS is used for all pods of a given flight.

From Figure 4.6, and the calculation of the correlation coefficient of the dataset containing all pods of all five flights ($R = 0.046$), we see that there appears to be no correlation between the thickness of the EIL and LTS using our analysis methods. Theoretically, we may expect LTS to be negatively correlated with EIL thickness, as turbulence within the EIL would have to work against large-scale stability in order for the EIL to grow in thickness. The fact that we see such weak correlation here may be due to the statistical sample being too small, or large time and spacial scale considerations being overwhelmed by small time scales and small scale processes.

4.3 Undulation Height and EIL Thickness

Bretherton et al. (1999) defined a quantity called undulation height, which is a measure of the deformation of the inversion above a boundary layer when a convective updraft collides with the stable inversion, by equating the gain in potential energy, $\delta z_u \Delta b$, with the loss of vertical kinetic energy, w_*^2, to obtain

$$\delta z_u = \frac{w_*^2}{\Delta b}, \tag{4.11}$$

where w_* is a convective velocity scale, and Δb is the buoyancy given by

$$\Delta b = g\frac{\Delta\Theta_l}{\Theta_{l0}}, \tag{4.12}$$

and g is gravity, $\Delta\Theta_l$ is the jump in Θ_l across the inversion, and Θ_{l0} is an average Θ_l in the EIL. To provide a range of estimates of this undulation height, we used five different approximations for the convective velocity scale in the flights studied here. The first three estimates were calculated in a layer stretching from cloud top down to 50 meters below cloud top. These three estimates were average updraft speed, standard deviation in vertical velocity (based on averages over one second, or about 50 meters horizontally), and the turbulent kinetic energy (TKE) based on horizontal and vertical velocities within that 50

meters (also based on averages over one second, or about 50 meters horizontally). For the fourth and fifth approximations of convective velocity scale, we used TKE taken from velocities within the EIL, and a velocity scale based on the convective mass flux, given by

$$M_c = \rho\sigma_u(1-\sigma_u)(w_u - w_d), \tag{4.13}$$

where ρ is the density of dry air, σ_u is updraft fractional area, and w_u and w_d are average updraft and downdraft velocities, respectively. After calculating δz_u for all five estimates of w_*, we plotted undulation heights for each pod against Δh for each pod for all five analyzed flights, and finally correlations were calculated between the various quantities. These plots are shown in Figures 4.7-4.11.

The correlations between δz_u (based on different measures of convective velocity scale) and Δh shown in Figures 4.7-4.11 are a mix of positive and negative values, and are weak at best. This seems to suggest that, in this case, undulation height is not related to EIL thickness and that there are other factors, such as shear near cloud top, that influence the thickness of the EIL and its relationship to the stability of the surrounding atmosphere.

4.4 Time Evolution of the EIL

Organizing the calculated values for EIL top and bottom heights with respect to longitude (and thus distance from the coast) provided a relatively local analysis of the time rate of change of the thickness of the EIL for our five flights. To accomplish this, the geographical domain for the pods of each flight was first calculated by computing the difference between the maximum and minimum longitude observed during all pods of a given flight. Next, this domain was divided into four equally wide sections, and the EIL top and bottom heights were binned into these four sections based on corresponding average

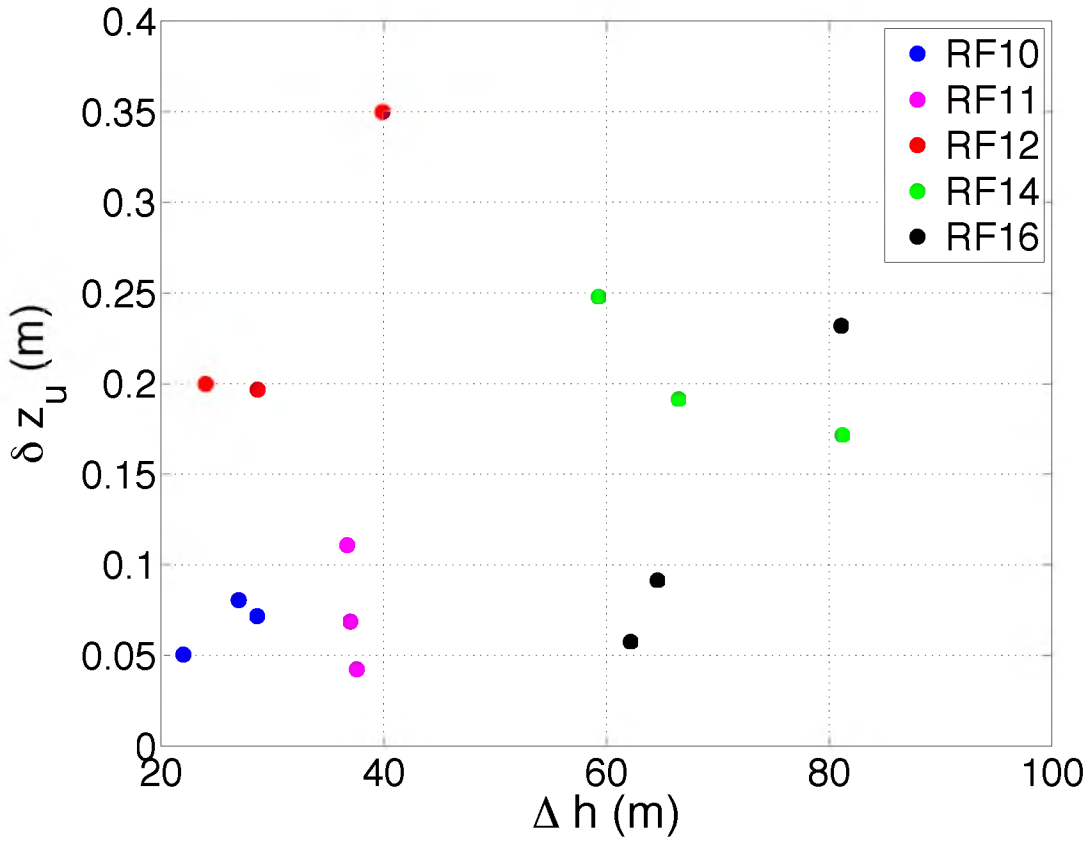

Figure 4.7: Correlation of undulation height, δz_u, calculated using average updraft speed within 50 meters of cloud top, with EIL thickness, Δh, for all five analyzed POST flights, R = 0.27.

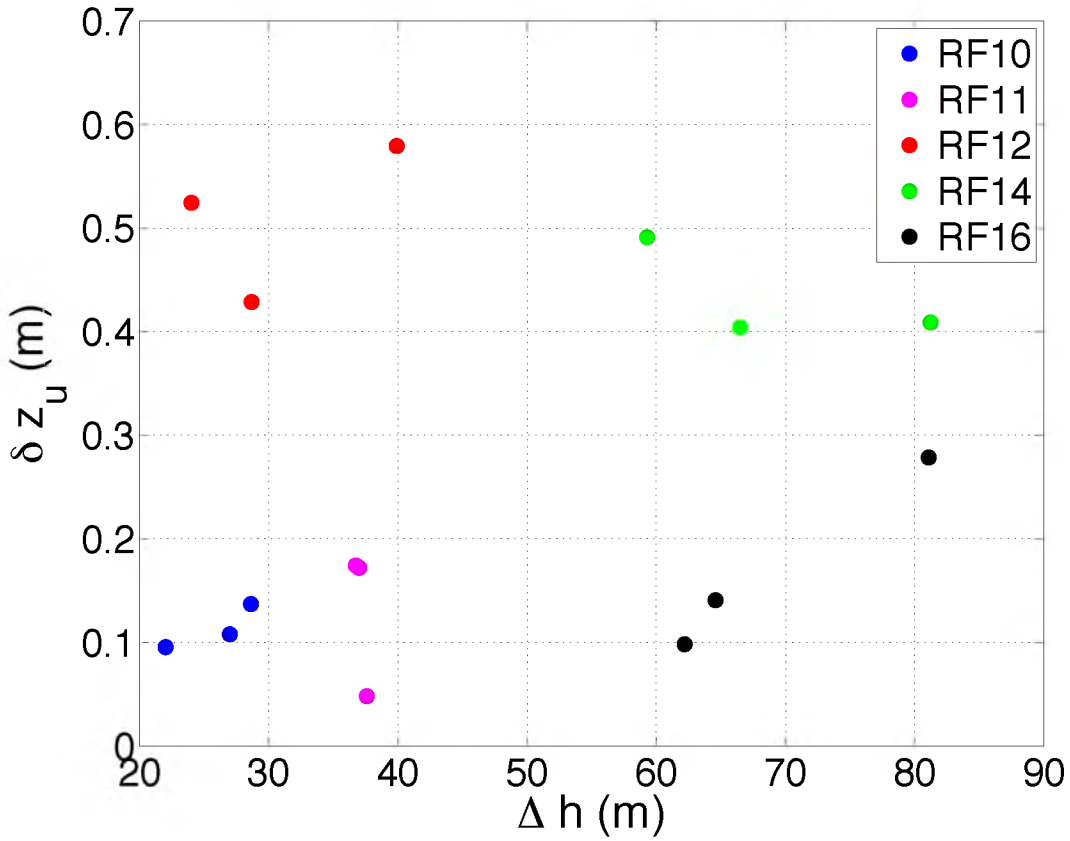

Figure 4.8: Correlation of undulation height, δz_u, calculated using standard deviation of vertical velocity within 50 meters of cloud top, with EIL thickness, Δh, for all five analyzed POST flights, R = 0.17.

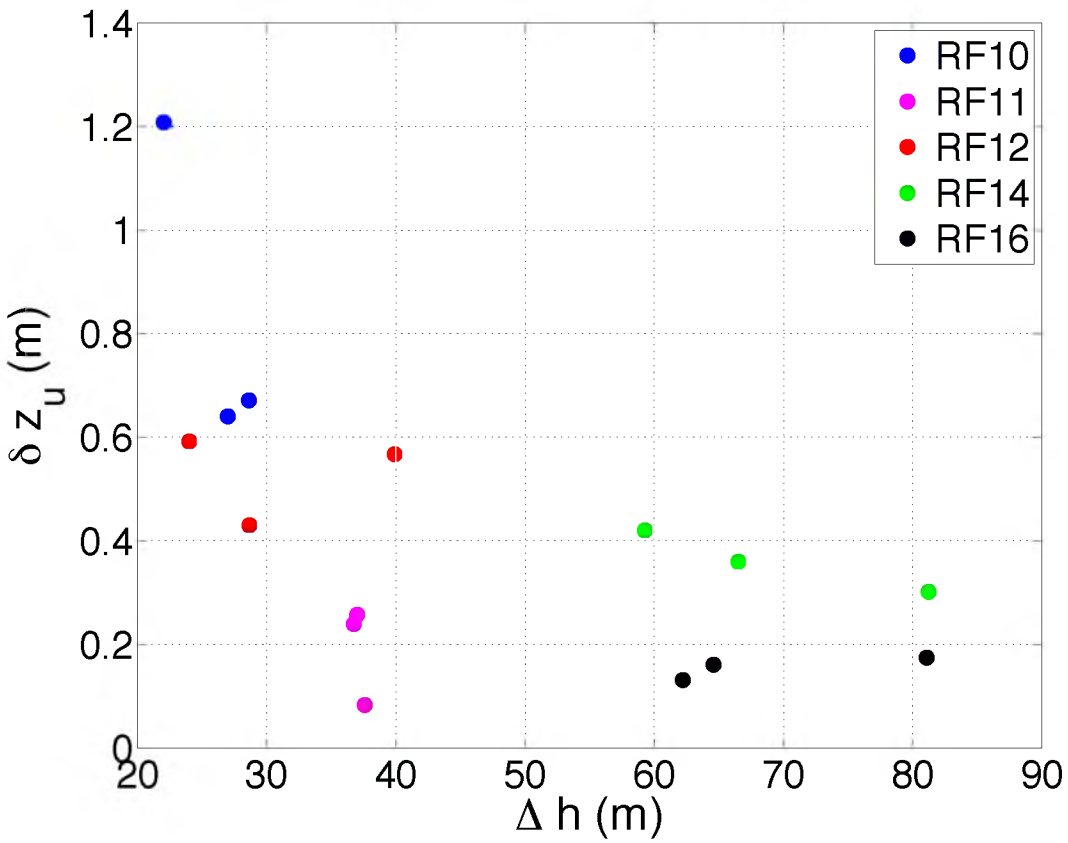

Figure 4.9: Correlation of undulation height, δz_u, calculated using TKE within 50 meters of cloud top, with EIL thickness, Δh, for all five analyzed POST flights, R = -0.59.

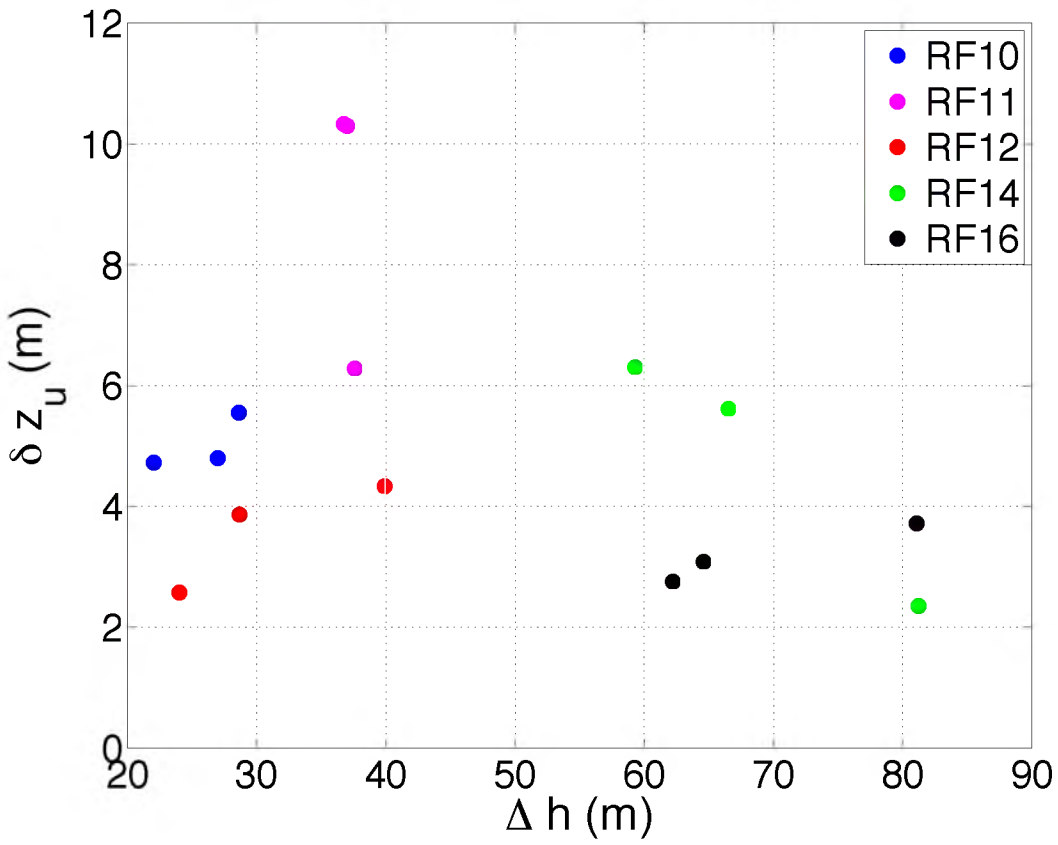

Figure 4.10: Correlation of undulation height, δz_u, calculated using TKE within the EIL, with EIL thickness, Δh, for all five analyzed POST flights, R = -0.30. Larger δz_u values here are due to greater horizontal velocities within the EIL, which are included in the TKE calculation.

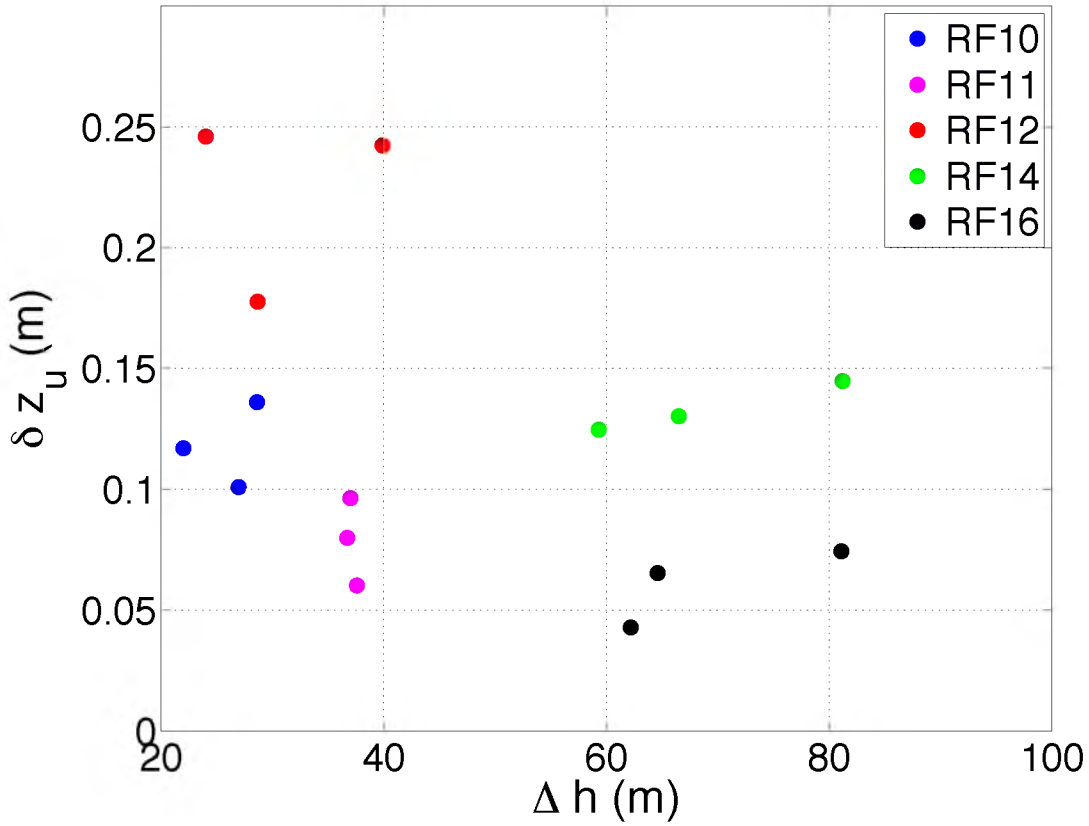

Figure 4.11: Correlation of undulation height, δz_u, calculated using convective mass flux, with EIL thickness, Δh, for all five analyzed POST flights, R = -0.34.

longitude data for individual porpoises during a flight. Finally, linear fits were made to the bins of EIL top heights and to the bins of EIL bottom heights, and the slopes of these linear fits were calculated to give an estimate for the time rate of change of EIL top and bottom heights and EIL thickness. Plots of EIL top and bottom heights as a function of longitude (bins) and time are shown in Figures 4.12 through 4.16.

Daytime RF10 shows EIL top and bottom heights shifting at nearly the same rate of change in the middle of the longitudinal domain, while thinning or thickening of the EIL takes place near the boundaries of the domain. The EIL for evening RF11 exhibits subtle rates of change in EIL top and bottom altitudes, with thinning and thickening of the EIL occurring across the domain. Evening RF12 seems to show a consistent increase in EIL top and bottom heights from east to west following the section of the domain closest to the coast. Evening RF14 shows variable rates of change across the domain. Finally, daytime RF16 shows lifting in each longitude subset, with some thinning of the EIL in the middle of the longitudinal domain.

4.5 Turbulence Profiles Across the EIL

Another way to approximate the location of the EIL is to analyze turbulence in the vicinity of, and across, the top of the cloudy mixed layer. Three of these quantities that characterize the turbulence in this regime are vertical velocity variance, horizontal velocity variance, and the isotropy of the flow itself. One would expect the variance in vertical velocity to be at a maximum in the cloud layer, where vertical velocity fluctuations are a characteristic of the turbulent cloud layer. Vertical velocity variance was calculated using

$$var(w) =< w'w' > \tag{4.14}$$

where

$$w' = w_i - < w > \tag{4.15}$$

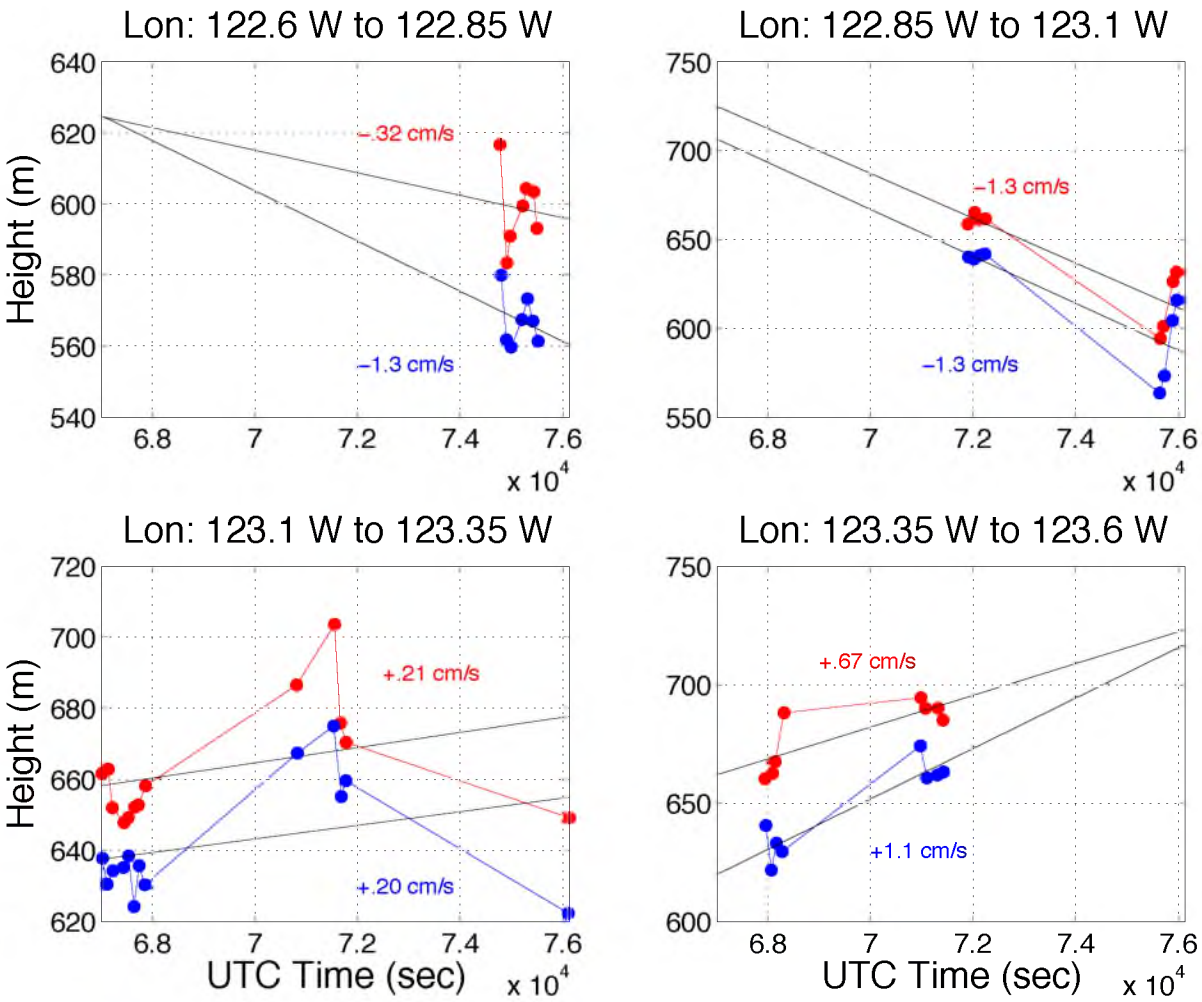

Figure 4.12: EIL thickness as a function of time in four subsets of longitude over the course of RF10, a daytime flight.

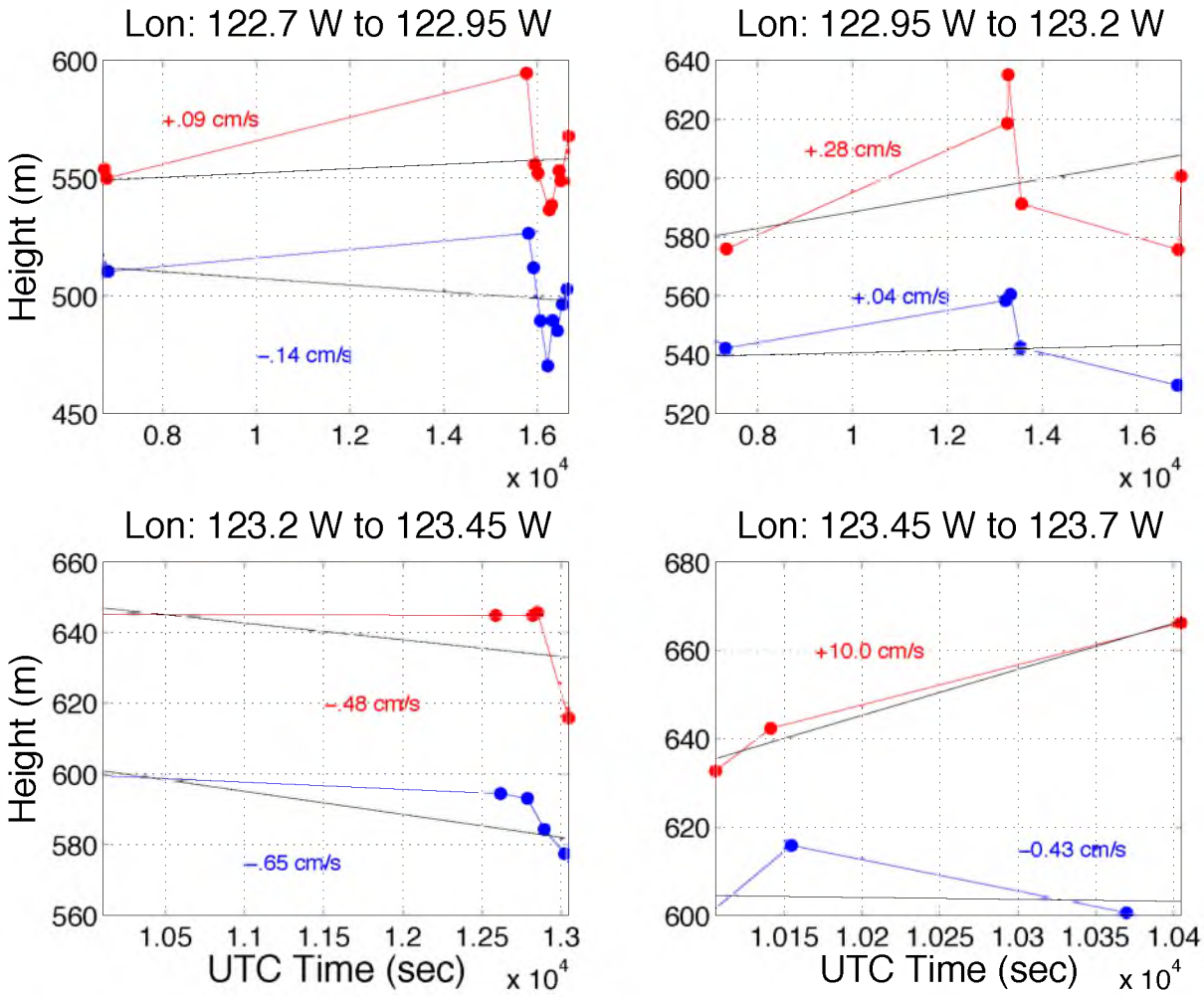

Figure 4.13: EIL thickness as a function of time in four subsets of longitude over the course of RF11, an evening flight.

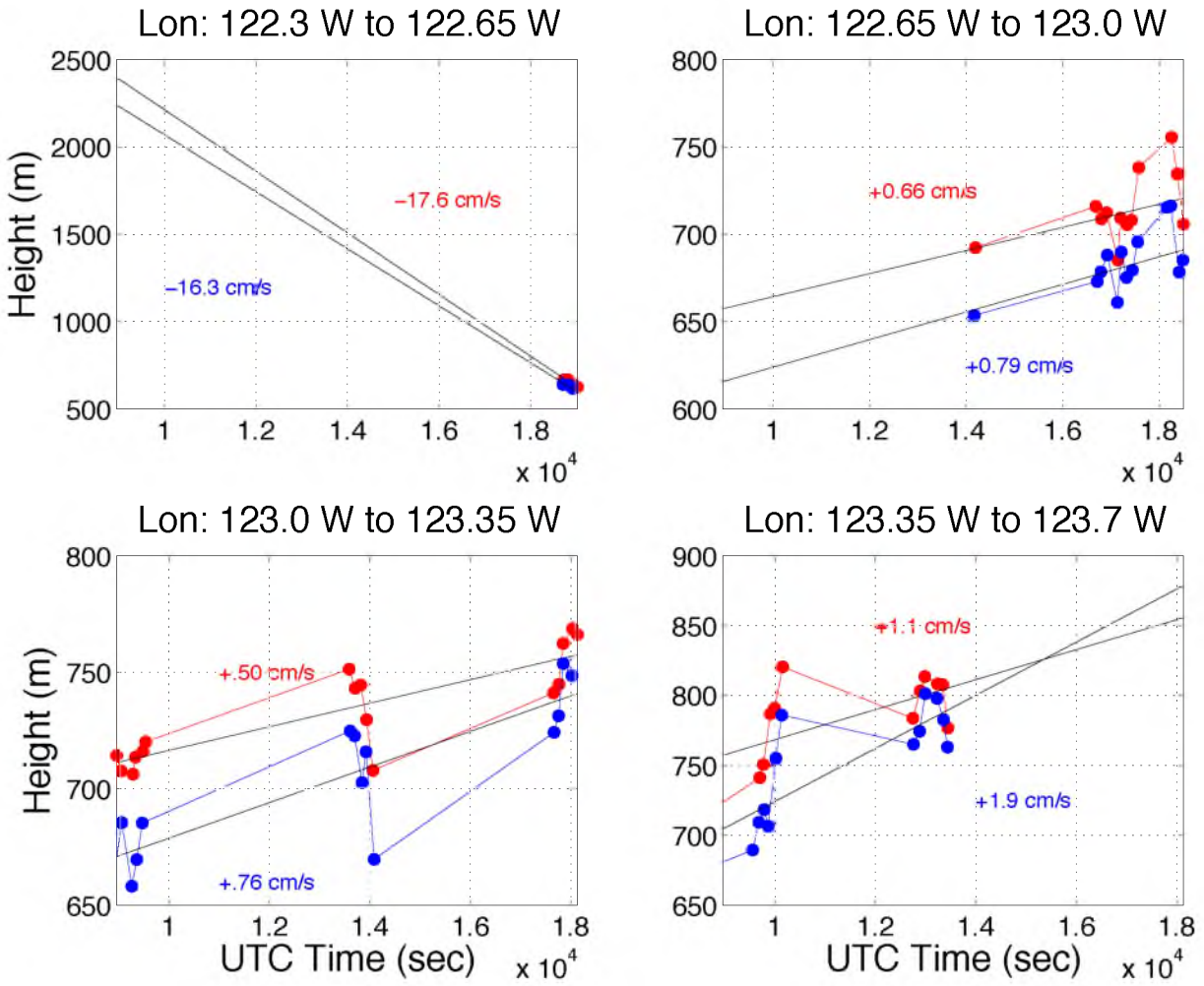

Figure 4.14: EIL thickness as a function of time in four subsets of longitude over the course of RF12, an evening flight.

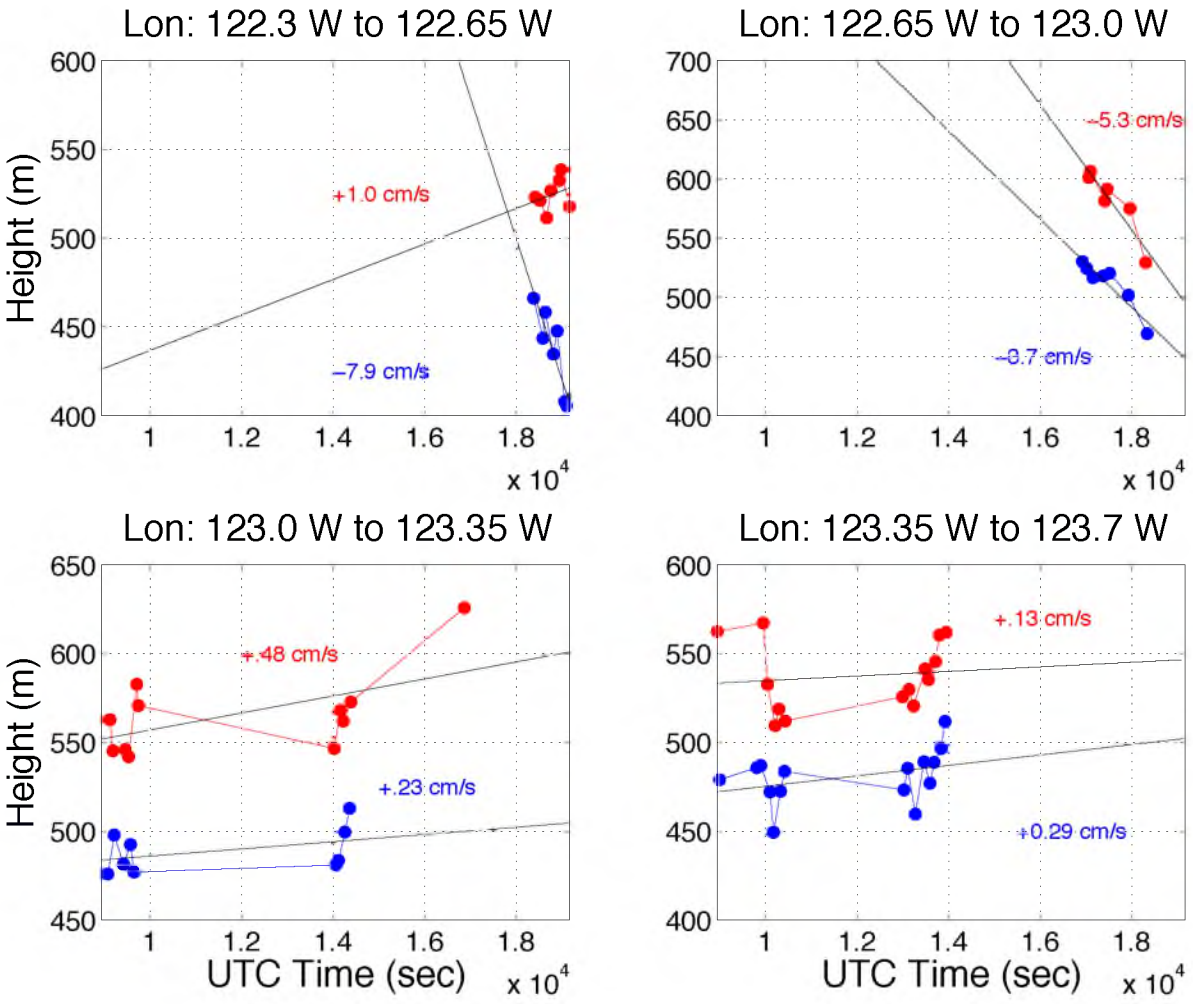

Figure 4.15: EIL thickness as a function of time in four subsets of longitude for RF14, an evening flight.

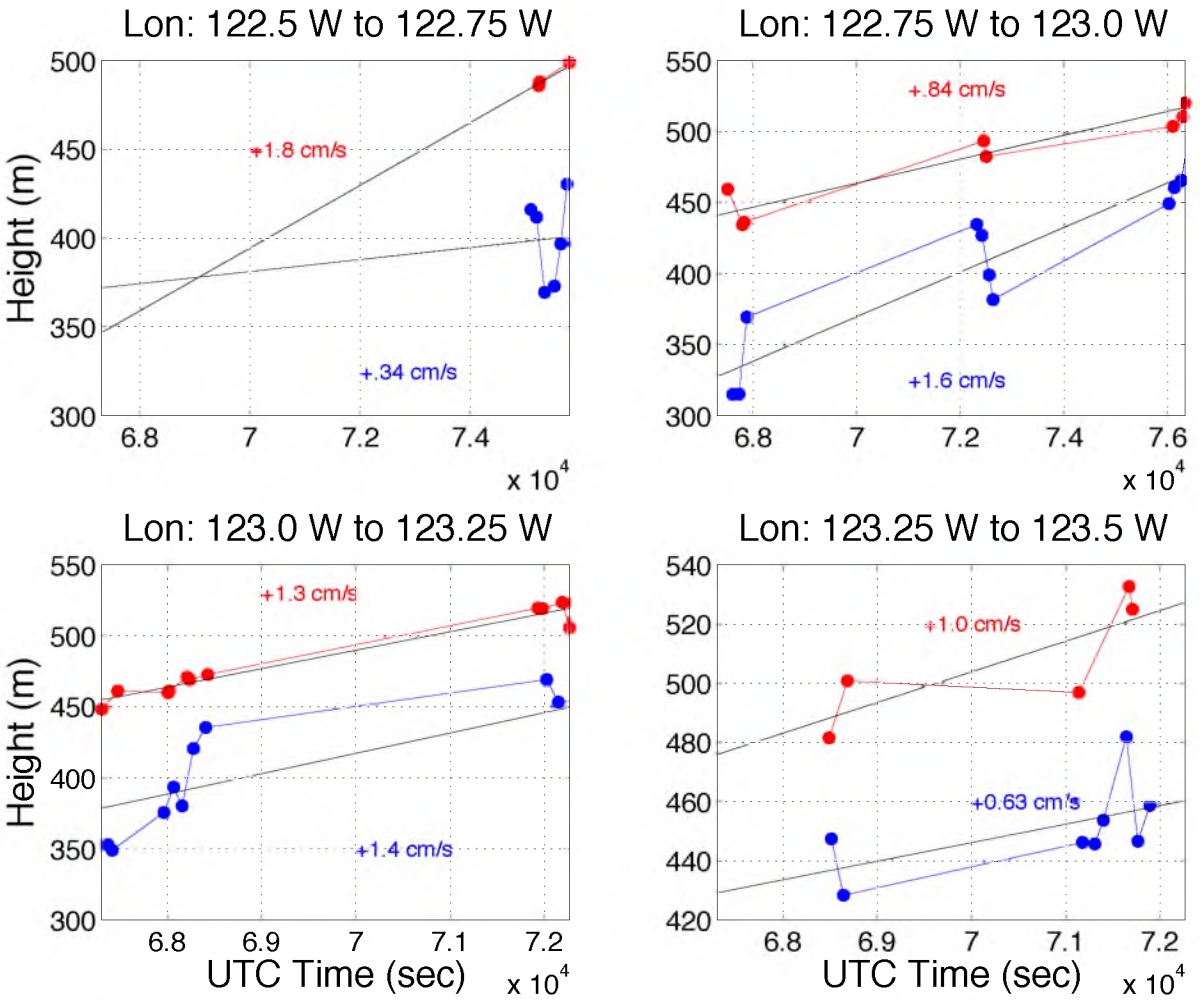

Figure 4.16: EIL thickness as a function of time in four subsets of longitude over the course of RF16, a daytime flight.

Here, w_i is an element from the vertical velocity time series, and $< w >$ is an average of vertical velocity over each second. Above the mixed layer, one would expect the vertical velocity variance to fall off, as horizontal motions are much more prevalent within the EIL and above the mixed layer. The total horizontal velocity variance, like vertical velocity variance, was calculated using

$$var(u + v) =< u'u' > + < v'v' > \tag{4.16}$$

where u' and v' are perturbations in horizontal velocity, calculated as in Section 4.2. One would expect horizontal velocity variance to peak within the EIL, and then fall off in the free troposphere.

Finally, isotropy, when applied to atmospheric velocity measurements, is a measure of the lack of directional dependence, and was calculated using

$$isotropy =< w'w' > /(< u'u' > + < v'v' > + < w'w' >) \tag{4.17}$$

One would expect isotropy values near 1 in the turbulent cloudy layer, where turbulence tends to move air in all directions, and thus shows a lack of dependence on direction. Above the turbulent mixed layer, one would expect isotropy values to decrease where horizontal motions dominate, especially in the free troposphere. Figures 4.17 through 4.21 show the three turbulent quantities from above. These plots include the data from all pods of each flight, binned according to mixing fraction, and then plotted as a mixing fraction profile.

Overall, Figures 4.17 through 4.21 reflect typical behavior at, and around, the mixed layer top: vertical velocity variance is at a maximum in the cloud layer, and falls off through the EIL and up through the free troposphere. Horizontal velocity variance peaks in the EIL, and takes on much smaller values both in the cloud layer and in the free troposphere. The exception to this behavior is RF16, where horizontal velocity variance falls off continuously through the EIL to a minimum value in the free troposphere. Finally, isotropy shows

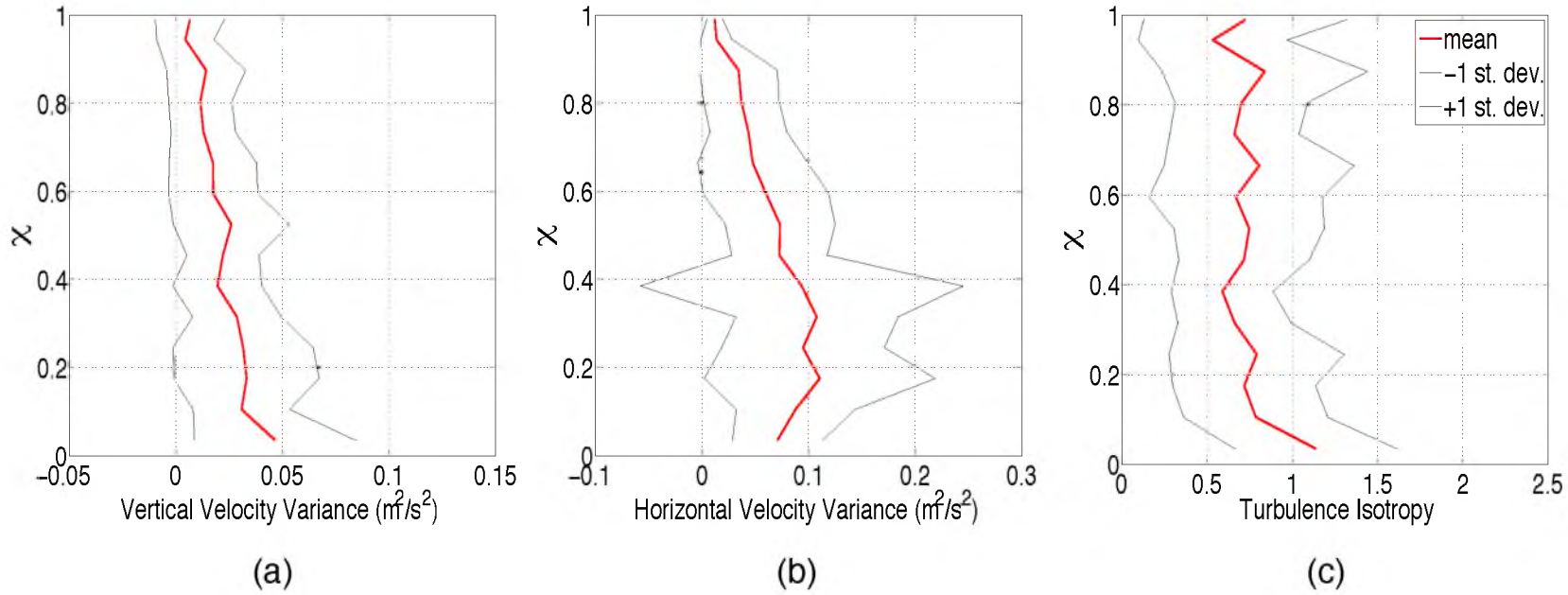

Figure 4.17: Profiles of (a) vertical velocity variance, (b) horizontal velocity variance, and (c) turbulence isotropy for data from all pods of RF10, a daytime flight.

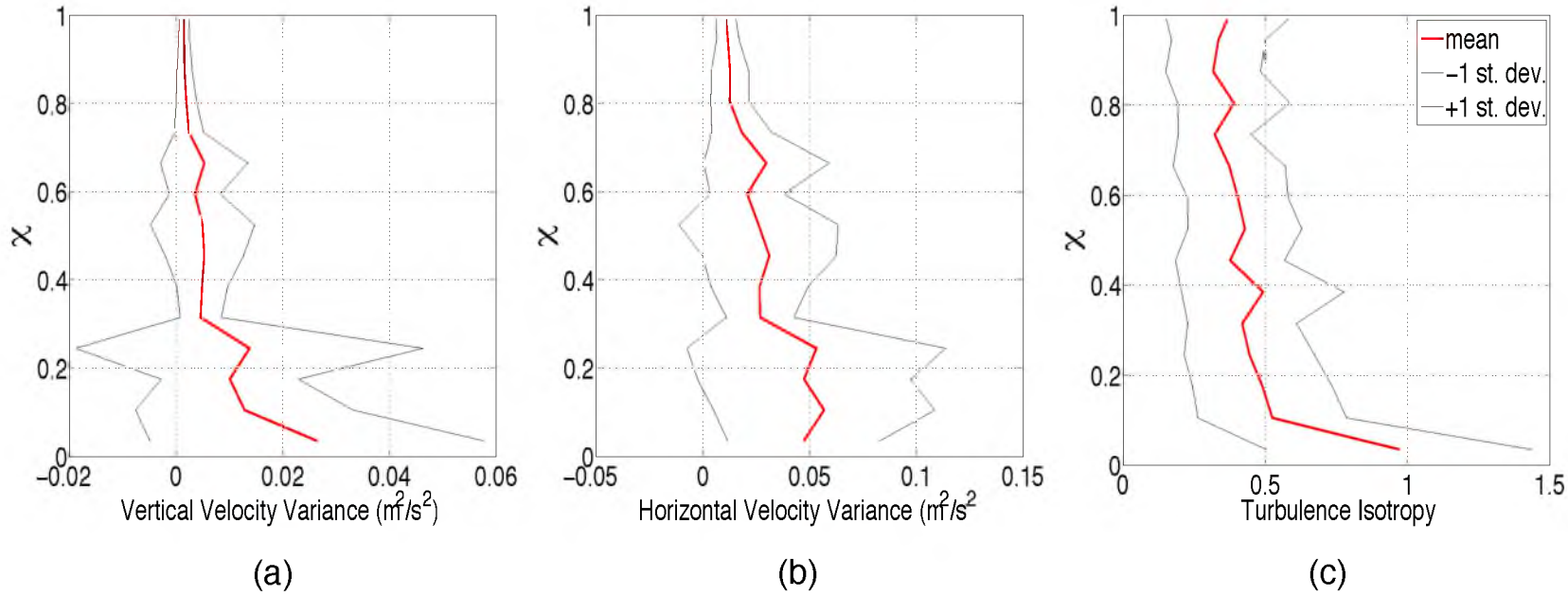

Figure 4.18: Profiles of (a) vertical velocity variance, (b) horizontal velocity variance, and (c) turbulence isotropy for data from all pods of RF11, an evening flight.

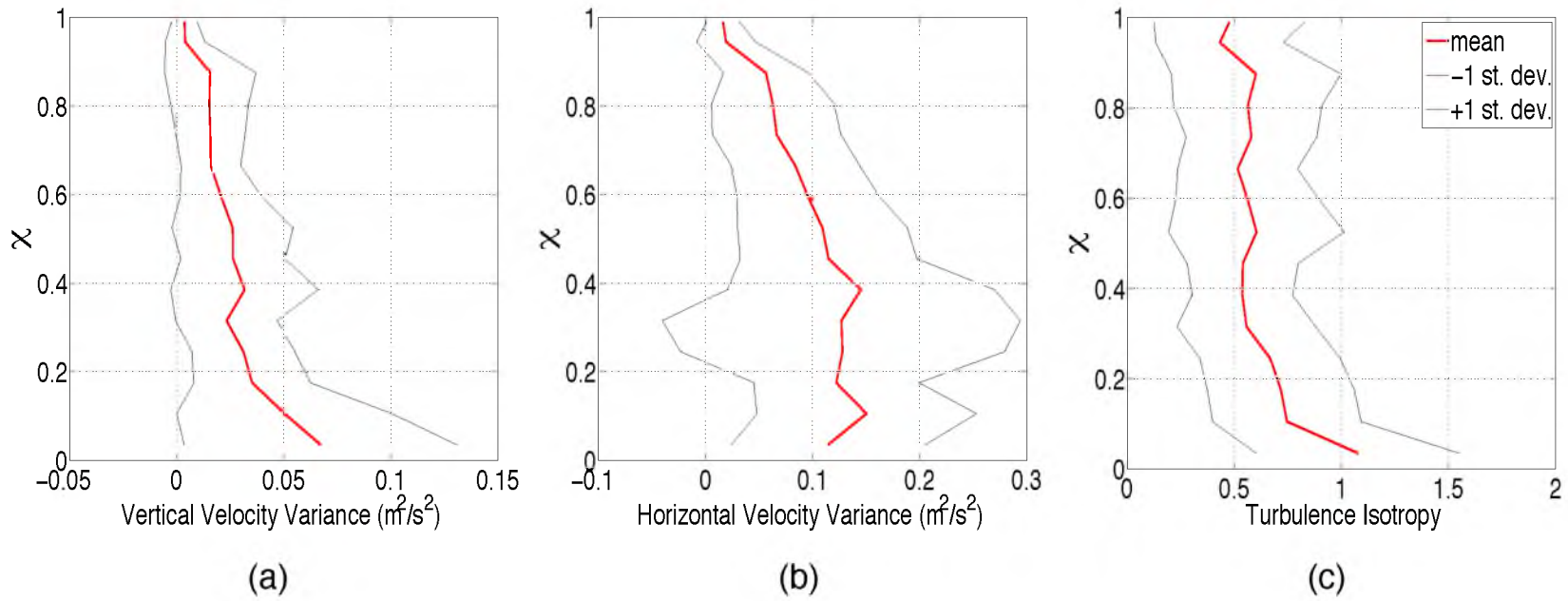

Figure 4.19: Profiles of (a) vertical velocity variance, (b) horizontal velocity variance, and (c) turbulence isotropy for data from all pods of RF12, an evening flight.

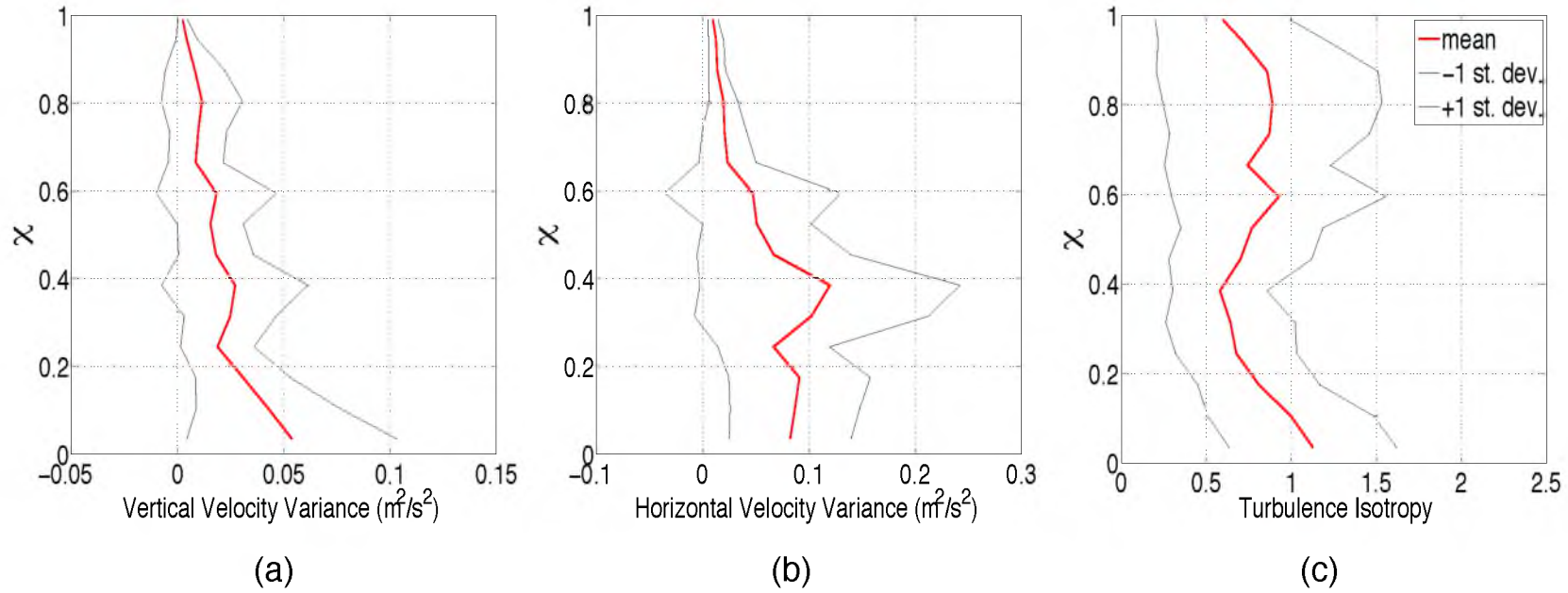

Figure 4.20: Profiles of (a) vertical velocity variance, (b) horizontal velocity variance, and (c) turbulence isotropy for data from all pods of RF14, an evening flight.

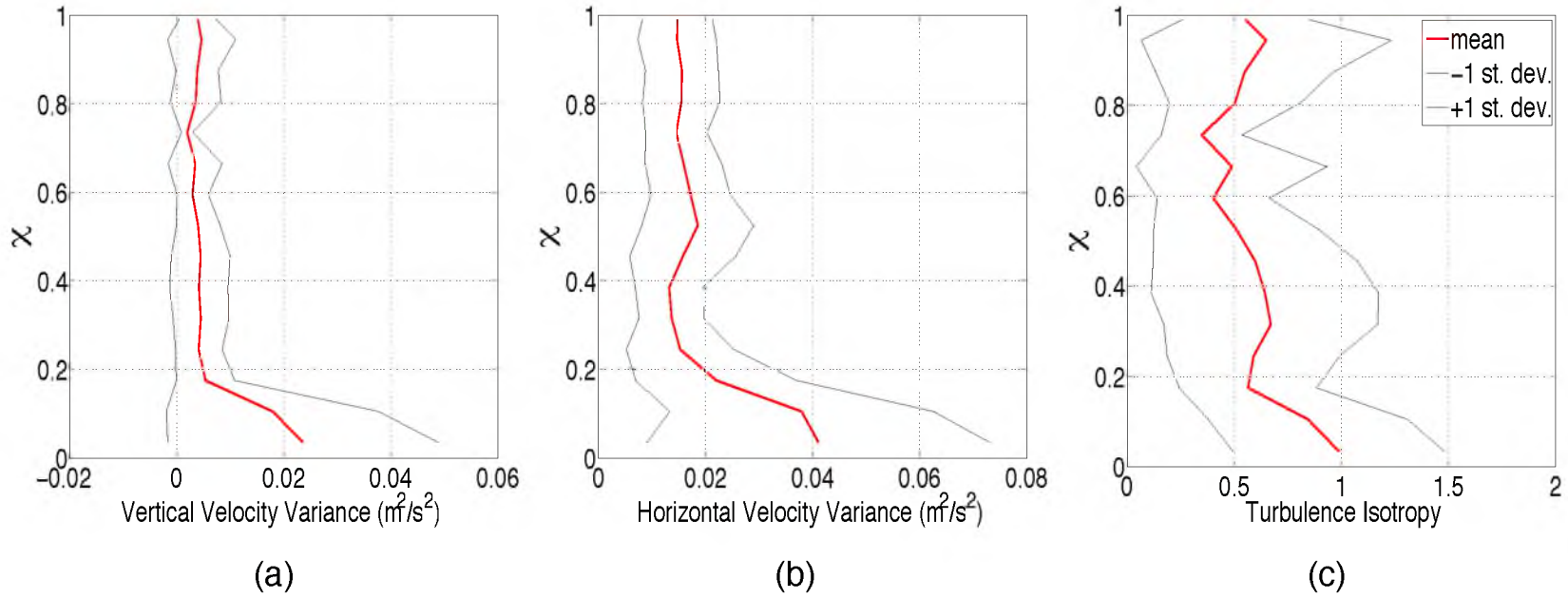

Figure 4.21: Profiles of (a) vertical velocity variance, (b) horizontal velocity variance, and (c) turbulence isotropy for data from all pods of RF16, a daytime flight.

values around 1 where we would expect the turbulent cloud layer to be, and then falls off noticeably up through the EIL and free troposphere, where we would expect to find horizontal motions dominating the flow more than vertical motions.

CHAPTER 5

EFFECTS OF RADIATION AND PHASE CHANGES

Various processes that take place within a Sc cloud layer and within the EIL, namely mixing, phase changes (evaporation of cloud droplets and condensation of vapor), and radiative effects (warming from direct solar radiation and cooling at cloud top) contribute to net virtual potential temperature changes near the top of a given cloud deck. This temperature change is an important detail in studying Sc cloud systems because it is a crucial factor in maintaining shallow convection, and may influence how a cloud deck evolves. In the following sections, we focus on the contributions to a net temperature change in the EIL from the effects of radiation and phase changes.

5.1 Effects of Radiation

Relative contributions of radiation and phase changes to a net temperature change near cloud top were calculated from moist conserved variables and mixing fraction. To calculate the cooling at cloud top due to radiation, we again follow the methodology from vanZanten and Duynkerke (2002):

$$(\delta\Theta_l)_{rad} = \delta\Theta_l - \chi\Delta\Theta_l \tag{5.18}$$

where

$$\delta\Theta_l = \Theta_{lm} - \overline{\Theta_{l2}} \tag{5.19}$$

is the local fluctuation in liquid water potential temperature along the flight path, and

$$\Delta\Theta_l = \overline{\Theta_{l1}} - \overline{\Theta_{l2}} \tag{5.20}$$

is the jump in liquid water potential temperature across the inversion at cloud top. As with the mixing fraction calculation, overbars refer to an average over a layer, a subscript of 1 refers to a free troposphere value, and a subscript of 2 refers to a cloudy mixed layer value. Free troposphere and mixed layer average values for Θ_l were extracted from mixing line diagrams, as layer average values for q_t were. Results from these calculations for each pod of the same five flights are shown in Figures 5.1 through 5.5 in two dimensional histograms.

Next, maximum, minimum, and mean values of warming and cooling for binned values of mixing fraction were calculated to provide a better approximation of heating and cooling across parcels in the midst of mixing within the EIL. For these calculations, mixing fraction values were binned over all mixing fractions found within the EIL (0.1-0.9), with a bin width of $\Delta\chi = 0.1$. Maximum, minimum, and mean $(\delta\Theta_l)_{rad}$ values were then calculated for each bin. The results of these calculations are shown in Tables 5.1 through 5.5.

For daytime RF10 and RF16, on average, net warming due to radiation occurs in the EIL across all mixing fractions. Although, the warming during RF16 is more pronounced than during RF10. Evening RF12 and RF14 exhibit slight cooling in the EIL on average, on the same order of magnitude. The outlier is evening RF11, which shows reduced cooling rates in the EIL and a net warming across all mixing fractions.

5.2 Effects of Phase Changes

The calculation of cooling/warming, at or near cloud top due to phase changes, was accomplished using the following equation, also from vanZanten and Duynkerke (2002):

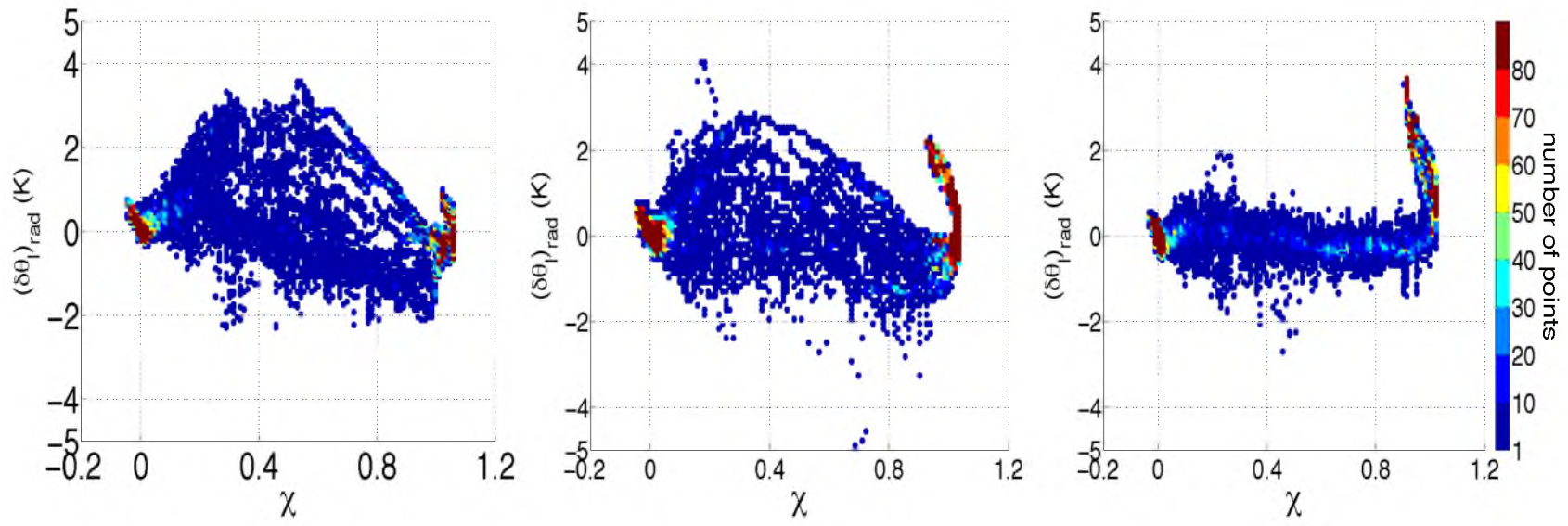

Figure 5.1: Liquid potential temperature change due to radiative effects for RF10, a daytime flight. Warmer colors indicate areas with dense points; cooler colors indicate areas with less dense points.

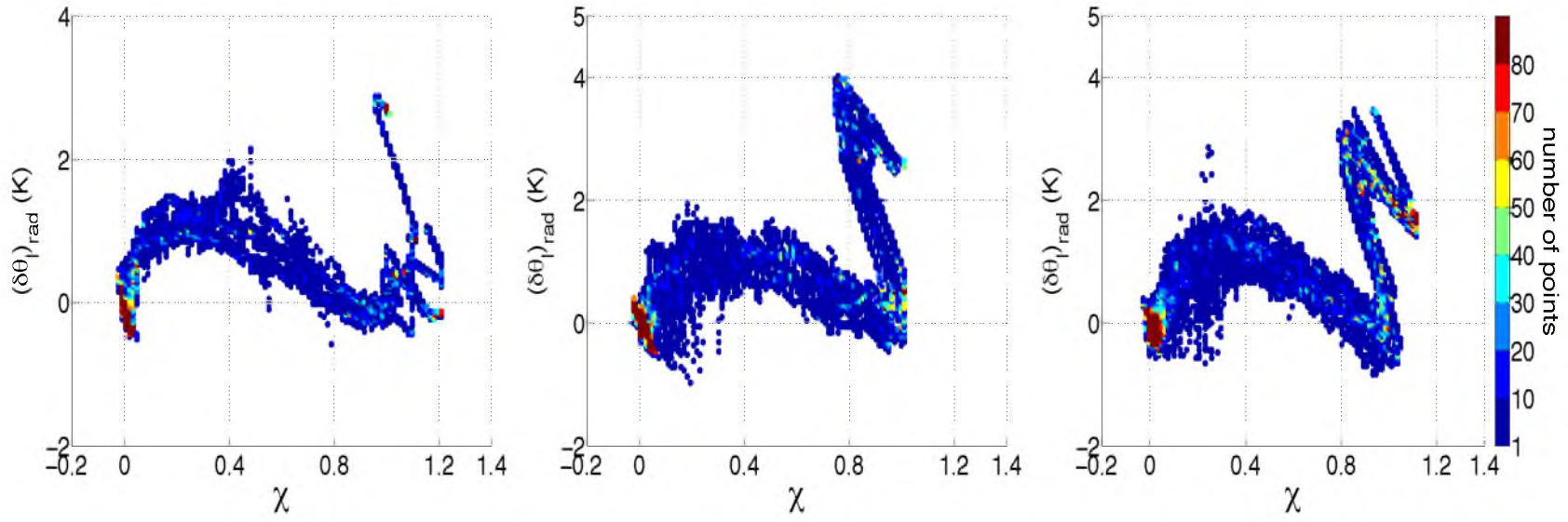

Figure 5.2: Liquid potential temperature change due to radiative effects for RF11, an evening flight. Warmer colors indicate areas with dense points; cooler colors indicate areas with fewer data points.

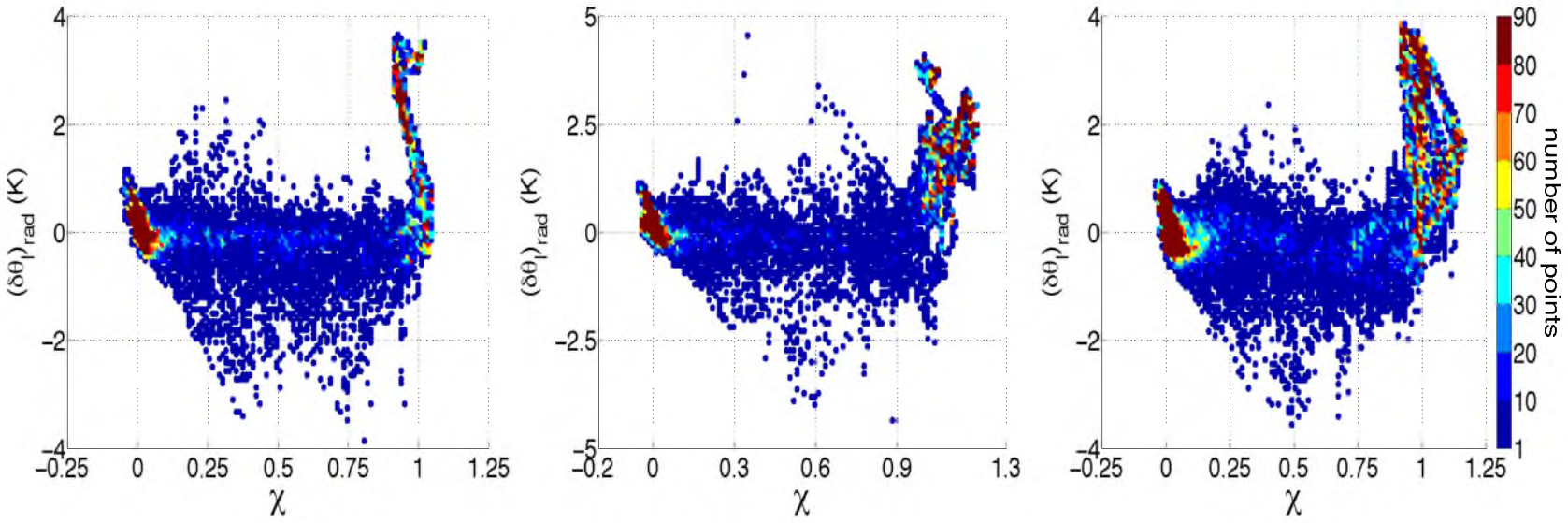

Figure 5.3: Liquid potential temperature change due to radiative effects for RF12, an evening flight. Warmer colors indicate areas with dense points; cooler colors indicate areas with fewer data points.

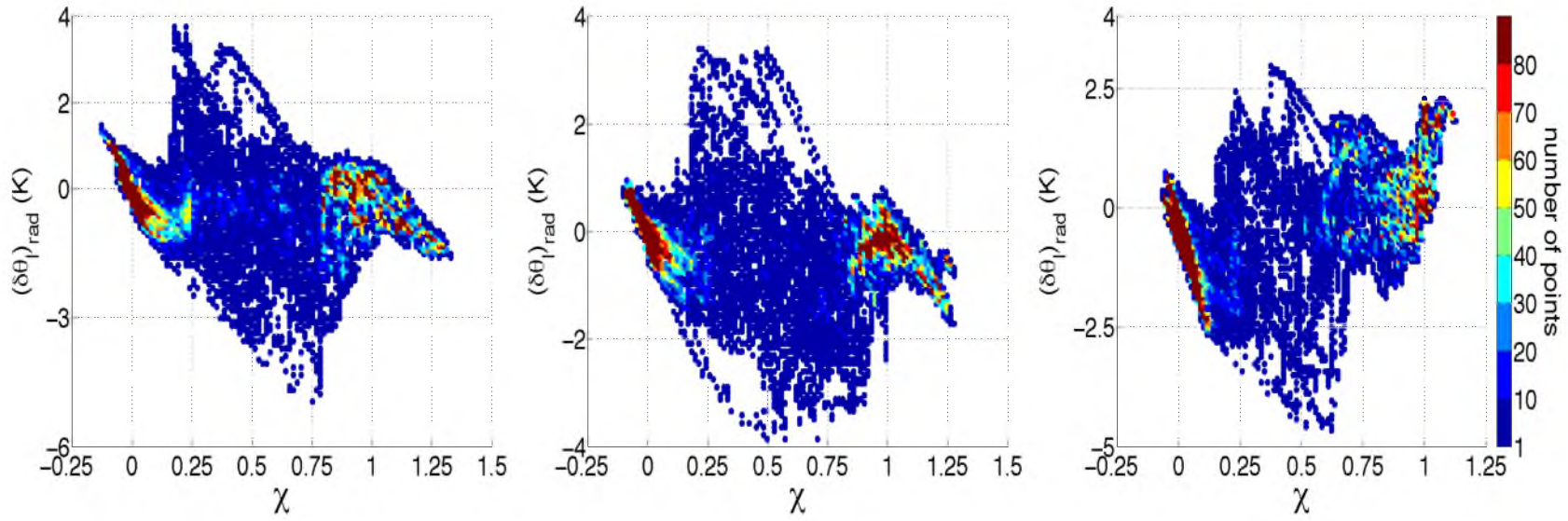

Figure 5.4: Liquid potential temperature change due to radiative effects for RF14, an evening flight. Warmer colors indicate areas with dense points; cooler colors indicate areas with fewer data points

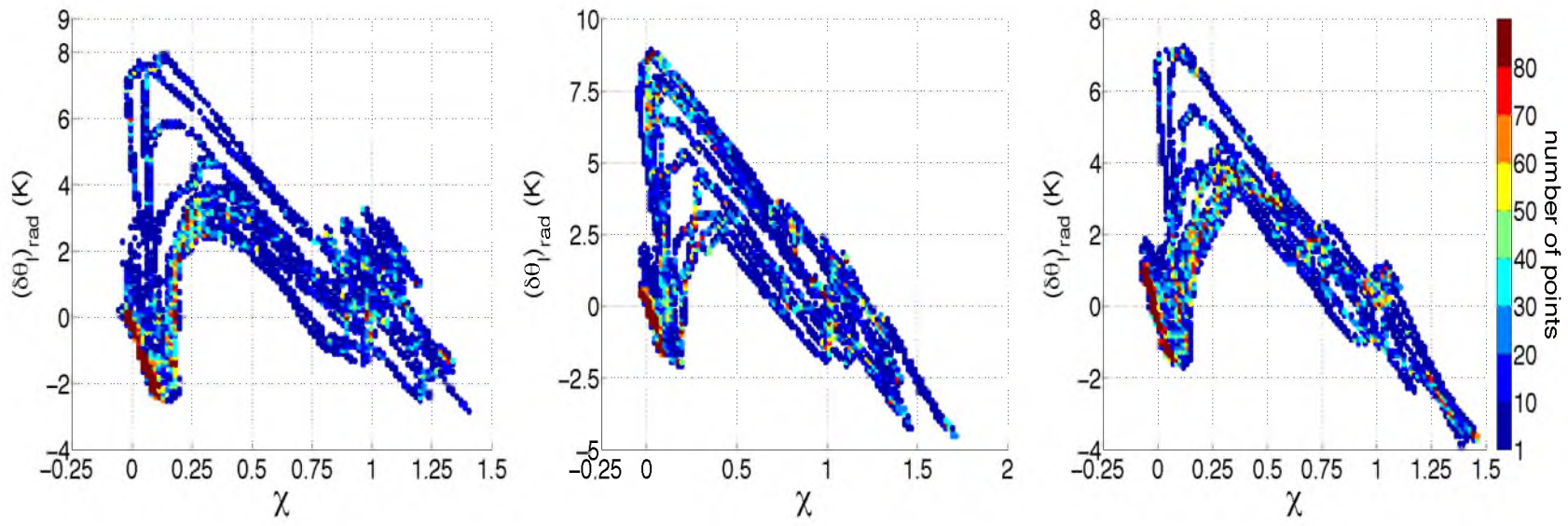

Figure 5.5: Liquid potential temperature change due to radiative effects for RF16, a daytime flight. Warmer colors indicate areas of denser points; cooler colors indicate areas with fewer data points.

Table 5.1: Average, maximum heating, and maximum cooling for binned regions within the EIL for RF10, a daytime flight.

RF10 - $(\delta\Theta_l)_{rad}$	Mean $(\delta\Theta_l)_{rad}$ (K)	Max. Warming (K)	Max. Cooling (K)
$0.1 < \chi < 0.2$	0.53	4.0	-1.9
$0.2 < \chi < 0.3$	0.78	3.4	-2.4
$0.3 < \chi < 0.4$	0.44	3.3	-2.2
$0.4 < \chi < 0.5$	0.27	3.1	-2.7
$0.5 < \chi < 0.6$	0.27	3.5	-6.7
$0.6 < \chi < 0.7$	0.15	2.9	-6.2
$0.7 < \chi < 0.8$	0.15	2.5	-4.7
$0.8 < \chi < 0.9$	-0.30	1.5	-2.8

Table 5.2: Average, maximum heating, and maximum cooling for binned regions within the EIL for RF11, an evening flight.

RF11 - $(\delta\Theta_l)_{rad}$	Mean $(\delta\Theta_l)_{rad}$ (K)	Max. Warming (K)	Max. Cooling (K)
$0.1 < \chi < 0.2$	0.82	1.9	-0.95
$0.2 < \chi < 0.3$	1.0	2.9	-0.79
$0.3 < \chi < 0.4$	1.2	1.9	-0.46
$0.4 < \chi < 0.5$	1.1	2.1	0.0
$0.5 < \chi < 0.6$	0.93	1.7	-0.095
$0.6 < \chi < 0.7$	0.68	1.4	0.0
$0.7 < \chi < 0.8$	1.5	4.0	-0.60
$0.8 < \chi < 0.9$	1.8	3.8	-0.67

Table 5.3: Average, maximum heating, and maximum cooling for binned regions within the EIL for RF12, an evening flight.

RF12 - $(\delta\Theta_l)_{rad}$	Mean $(\delta\Theta_l)_{rad}$ (K)	Max. Warming (K)	Max. Cooling (K)
$0.1 < \chi < 0.2$	-0.13	1.9	-1.9
$0.2 < \chi < 0.3$	-0.15	2.3	-2.7
$0.3 < \chi < 0.4$	-0.23	4.5	-3.4
$0.4 < \chi < 0.5$	-0.34	2.0	-3.6
$0.5 < \chi < 0.6$	-0.43	2.6	-4.0
$0.6 < \chi < 0.7$	-0.41	3.4	-3.7
$0.7 < \chi < 0.8$	-0.41	2.5	-3.5
$0.8 < \chi < 0.9$	-0.25	1.7	-4.4

Table 5.4: Average, maximum heating, and maximum cooling for binned regions within the EIL for RF14, an evening flight.

RF14 - $(\delta\Theta_l)_{rad}$	Mean $(\delta\Theta_l)_{rad}$ (K)	Max. Warming (K)	Max. Cooling (K)
$0.1 < \chi < 0.2$	-0.92	3.8	-3.0
$0.2 < \chi < 0.3$	-0.54	3.7	-3.4
$0.3 < \chi < 0.4$	-0.32	3.3	-3.9
$0.4 < \chi < 0.5$	-0.55	3.4	-4.4
$0.5 < \chi < 0.6$	-0.61	3.3	-4.6
$0.6 < \chi < 0.7$	-0.12	2.6	-4.7
$0.7 < \chi < 0.8$	-0.19	1.9	-5.0
$0.8 < \chi < 0.9$	-0.25	1.5	-3.4

Table 5.5: Average, maximum heating, and maximum cooling for binned regions within the EIL for RF16, a daytime flight.

RF16 - $(\delta\Theta_l)_{rad}$	Mean $(\delta\Theta_l)_{rad}$ (K)	Max. Warming (K)	Max. Cooling (K)
$0.1 < \chi < 0.2$	1.2	8.5	-2.6
$0.2 < \chi < 0.3$	3.3	7.8	-1.9
$0.3 < \chi < 0.4$	3.7	6.9	0.0
$0.4 < \chi < 0.5$	3.6	6.1	0.0
$0.5 < \chi < 0.6$	2.9	5.3	0.0
$0.6 < \chi < 0.7$	2.0	4.4	0.0
$0.7 < \chi < 0.8$	1.4	3.7	-0.87
$0.8 < \chi < 0.9$	1.1	3.4	-1.4

$$(\delta\Theta_v)_{phase} = (\frac{L_v}{c_{pd}} - 1.61\overline{\Theta_{l2}})(q_{lm} - [1-\chi]\overline{q_{l2}}) \tag{5.21}$$

where L_v is the latent heat of vaporization, c_{pd} is the specific heat of dry air at constant pressure, χ is mixing fraction, and the definitions of subscripts and overbars remain the same as for previous equations. In this equation, however, an estimate of the average liquid water mixing ratio of pure cloud layer air is required. To make a reliable approximation for this quantity, a saturation adjustment code was used, with inputs of pressure, temperature, and vapor mixing ratio from the aircraft data. The code calculated a saturation adjusted value for each point along the flight path, which were used in the above equation to calculate the relative contribution of phase changes to temperature effects at cloud top. Results from these calculations for each pod of the five flights are shown in Figures 5.6 through 5.10.

Here again, maximum, minimum, and mean values of warming and cooling for binned values of $(\delta\Theta_v)_{phase}$ according to mixing fraction were calculated. The results of these calculations are displayed in Tables 5.6 through 5.10.

Daytime RF10 and RF16, as well as evening RF11, RF12, and RF14 exhibit net cooling due to phase changes within the EIL across all mixing fraction values on average. This highlights the effects of evaporative cooling near the the top of the cloud layer, and within the EIL regardless of the time of day. For the majority of the time, cooling values are kept to less than 0.7 K, with many substantially lower than this.

5.3 Comparisons Between Radiative and Phase Change Effects

For all flights, magnitudes of the temperature changes in the EIL due to radiative effects and due to phase changes are comparable, on average. The exception to this is daytime RF16, which shows pronounced warming within the EIL, and more subtle cooling.

The net effects due to radiation seem to be due to a balance between heating and cooling within the EIL, whereas net effects from phase changes are due to an absence of condensational warming within the EIL against a background of widespread evaporative cooling.

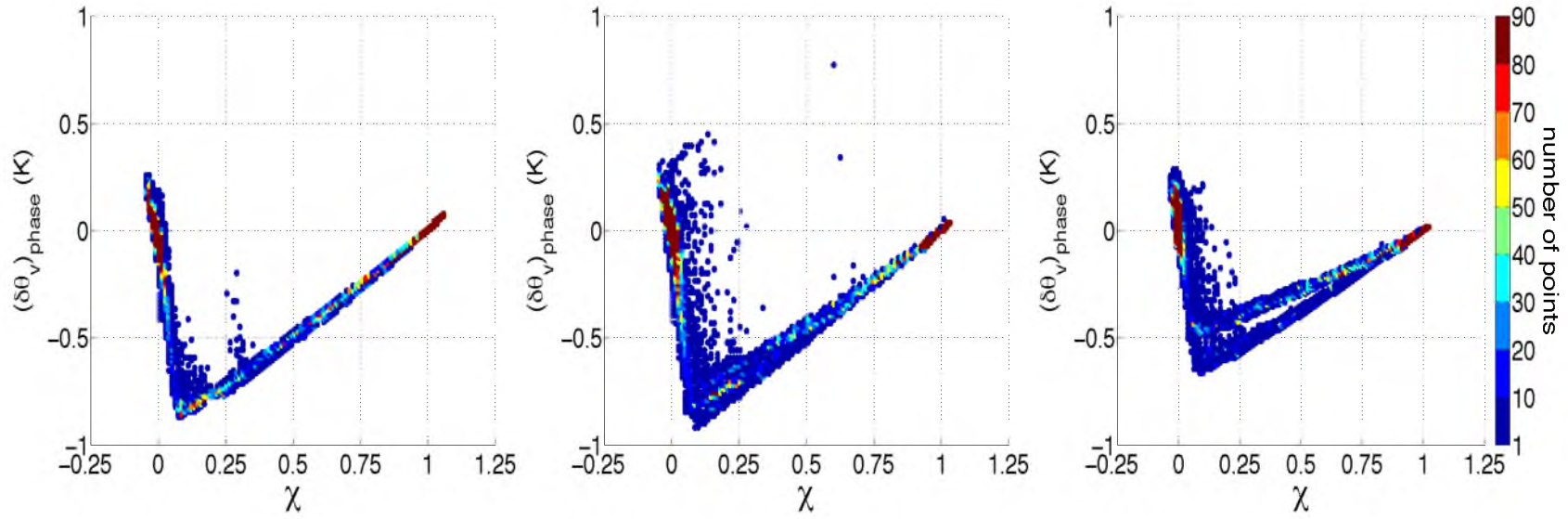

Figure 5.6: Virtual potential temperature change due to phase changes for RF10, a daytime flight. Warmer colors indicate areas with dense points; cooler colors indicate areas with fewer data points.

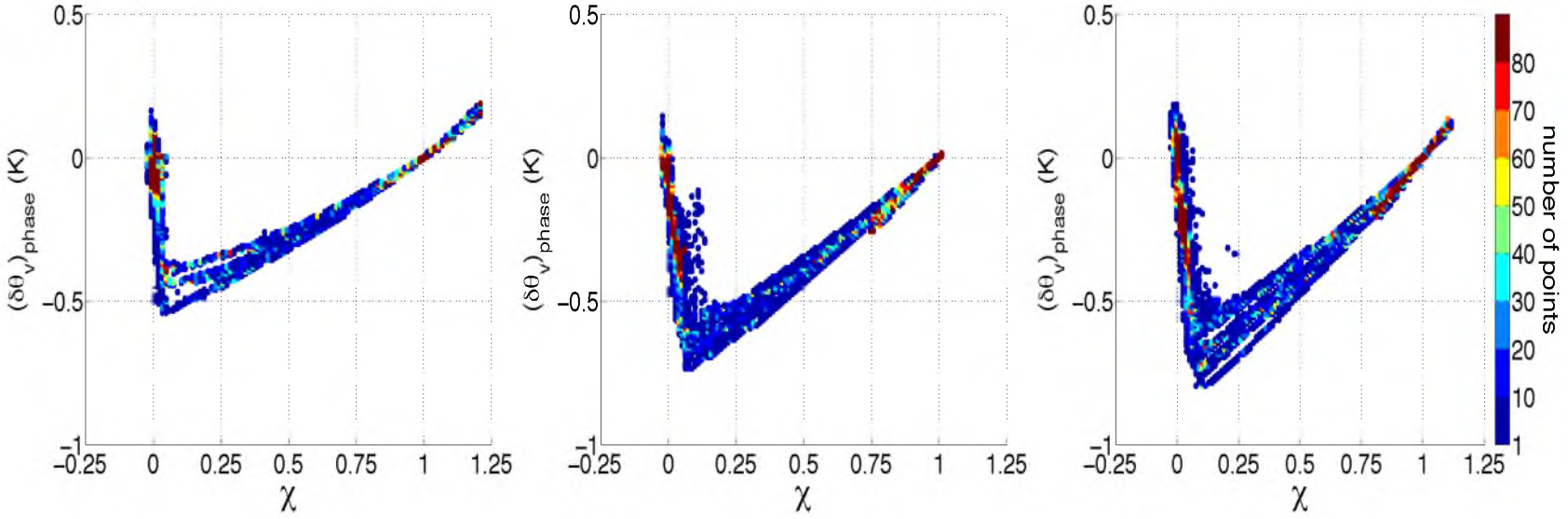

Figure 5.7: Virtual potential temperature change due to phase changes for RF11, an evening flight. Warmer colors indicate areas with dense points; cooler colors indicate areas with fewer data points.

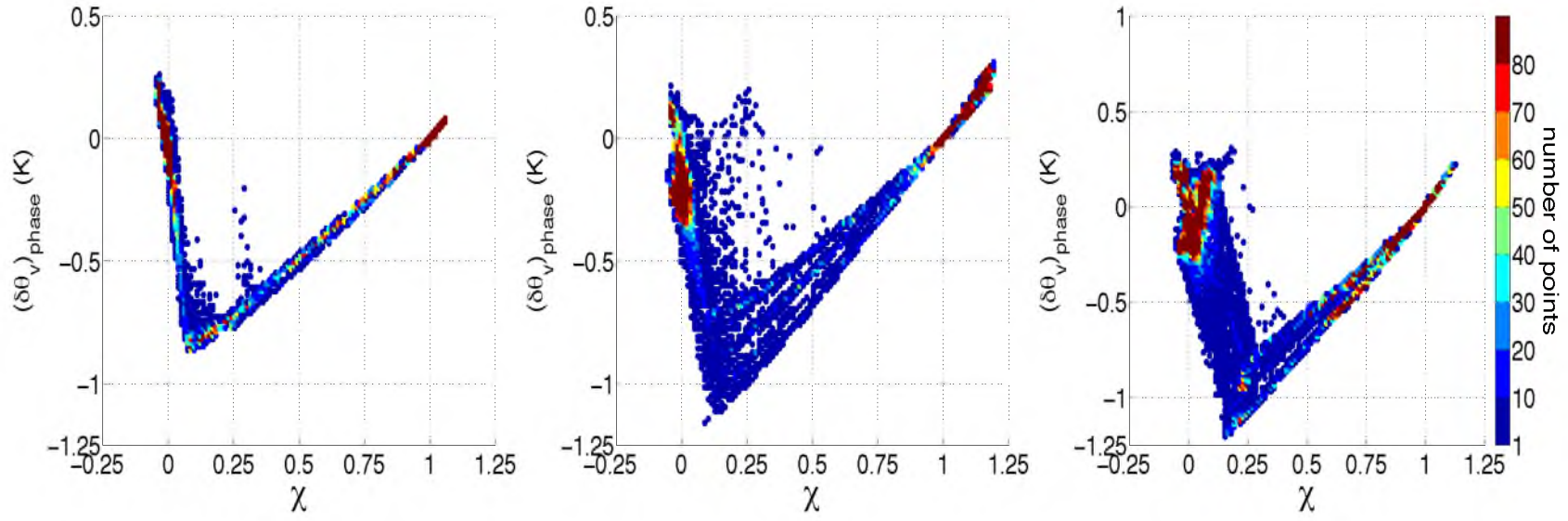

Figure 5.8: Virtual potential temperature change due to phase changes for RF12, an evening flight. Warmer colors indicate areas with dense points; cooler colors indicate areas with fewer data points.

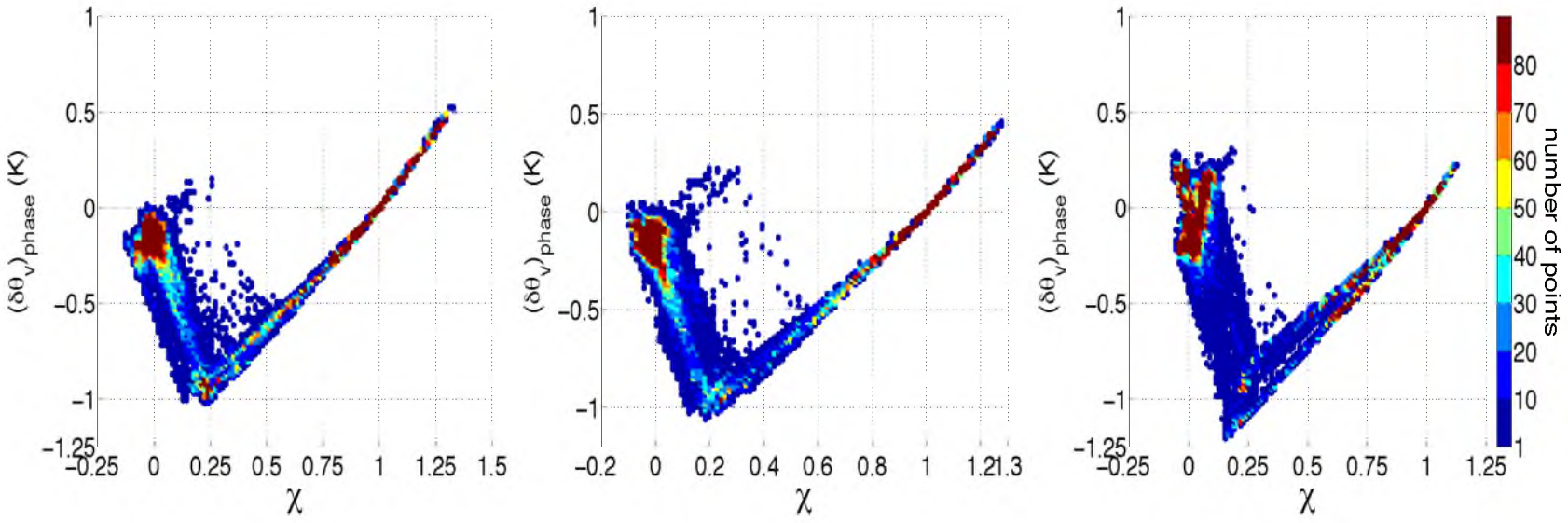

Figure 5.9: Virtual potential temperature change due to phase changes for RF14, an evening flight. Warmer colors indicate areas with dense points; cooler colors indicate areas with fewer data points.

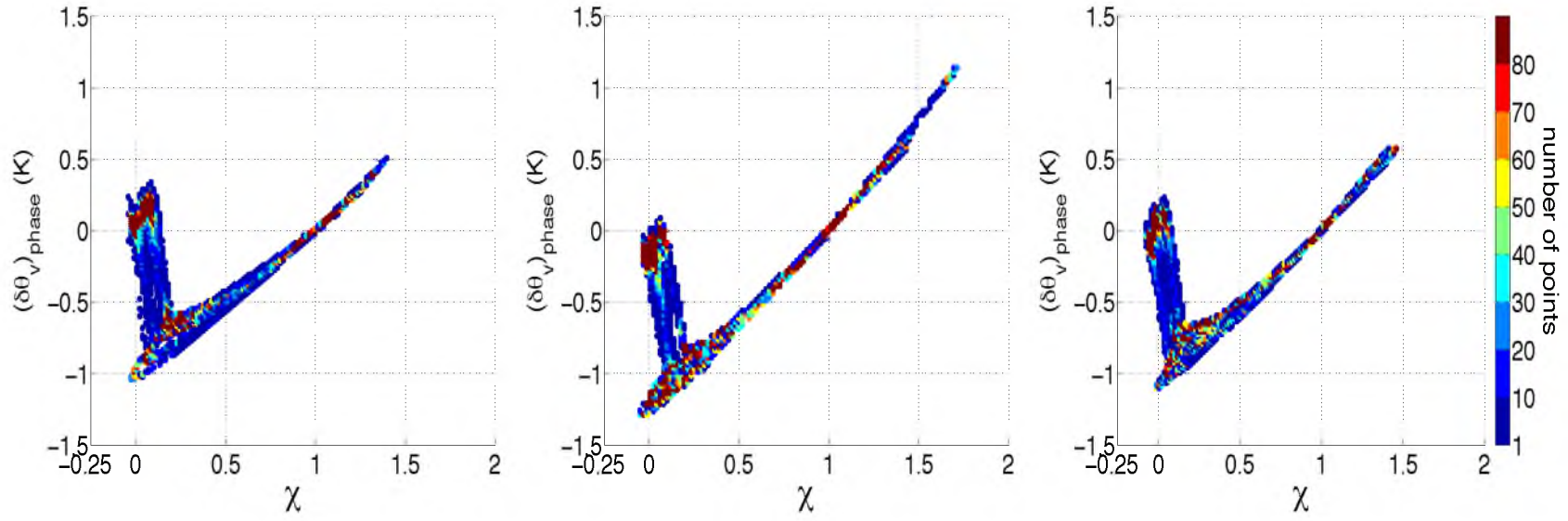

Figure 5.10: Virtual potential temperature change due to phase changes for RF16, a daytime flight. Warmer colors indicate areas with dense points; cooler colors indicate areas with fewer data points.

Table 5.6: Average, maximum heating, and maximum cooling due to phase changes for binned regions within the EIL for RF10, a daytime flight.

RF10 - $(\delta\Theta_v)_{phase}$	Mean $(\delta\Theta_v)_{phase}$ (K)	Max. Warming (K)	Max. Cooling (K)
$0.1 < \chi < 0.2$	-0.68	0.44	-0.91
$0.2 < \chi < 0.3$	-0.61	0.085	-0.82
$0.3 < \chi < 0.4$	-0.53	0.0	-0.72
$0.4 < \chi < 0.5$	-0.44	0.0	-0.62
$0.5 < \chi < 0.6$	-0.37	0.77	-0.53
$0.6 < \chi < 0.7$	-0.28	0.33	-0.43
$0.7 < \chi < 0.8$	-0.21	0.0	-0.33
$0.8 < \chi < 0.9$	-0.13	0.0	-0.22

Table 5.7: Average, maximum heating, and maximum cooling due to phase changes for binned regions within the EIL for RF11, an evening flight.

RF11 - $(\delta\Theta_v)_{phase}$	Mean $(\delta\Theta_v)_{phase}$ (K)	Max. Warming (K)	Max. Cooling (K)
$0.1 < \chi < 0.2$	-0.58	0.0	-0.81
$0.2 < \chi < 0.3$	-0.50	0.0	-0.81
$0.3 < \chi < 0.4$	-0.45	0.0	-0.65
$0.4 < \chi < 0.5$	-0.40	0.0	-0.57
$0.5 < \chi < 0.6$	-0.34	0.0	-0.47
$0.6 < \chi < 0.7$	-0.27	0.0	-0.38
$0.7 < \chi < 0.8$	-0.21	0.0	-0.29
$0.8 < \chi < 0.9$	-0.13	0.0	-0.21

Table 5.8: Average, maximum heating, and maximum cooling due to phase changes for binned regions within the EIL for RF12, an evening flight.

RF12 - $(\delta\Theta_v)_{phase}$	Mean $(\delta\Theta_v)_{phase}$ (K)	Max. Warming (K)	Max. Cooling (K)
$0.1 < \chi < 0.2$	-0.70	0.36	-1.2
$0.2 < \chi < 0.3$	-0.74	0.25	-1.1
$0.3 < \chi < 0.4$	-0.67	0.27	-0.98
$0.4 < \chi < 0.5$	-0.57	0.0	-0.84
$0.5 < \chi < 0.6$	-0.48	0.0	-0.71
$0.6 < \chi < 0.7$	-0.38	0.0	-0.57
$0.7 < \chi < 0.8$	-0.27	0.0	-0.42
$0.8 < \chi < 0.9$	-0.17	0.0	-0.29

Table 5.9: Average, maximum heating, and maximum cooling due to phase changes for binned regions within the EIL for RF14, an evening flight.

RF14 - $(\delta\Theta_v)_{phase}$	Mean $(\delta\Theta_v)_{phase}$ (K)	Max. Warming (K)	Max. Cooling (K)
$0.1 < \chi < 0.2$	-0.55	0.31	-1.2
$0.2 < \chi < 0.3$	-0.89	0.21	-1.1
$0.3 < \chi < 0.4$	-0.81	0.22	-1.0
$0.4 < \chi < 0.5$	-0.69	0.0	-0.88
$0.5 < \chi < 0.6$	-0.57	0.0	-0.74
$0.6 < \chi < 0.7$	-0.47	0.0	-0.60
$0.7 < \chi < 0.8$	-0.34	0.0	-0.47
$0.8 < \chi < 0.9$	-0.20	0.0	-0.33

Table 5.10: Average, maximum heating, and maximum cooling due to phase changes for binned regions within the EIL for RF16, a daytime flight.

RF16 - $(\delta\Theta_v)_{phase}$	Mean $(\delta\Theta_v)_{phase}$ (K)	Max. Warming (K)	Max. Cooling (K)
$0.1 < \chi < 0.2$	-0.69	0.26	-1.2
$0.2 < \chi < 0.3$	-0.75	0.0	-1.1
$0.3 < \chi < 0.4$	-0.69	0.0	-0.95
$0.4 < \chi < 0.5$	-0.60	0.0	-0.81
$0.5 < \chi < 0.6$	-0.50	0.0	-0.68
$0.6 < \chi < 0.7$	-0.40	0.0	-0.55
$0.7 < \chi < 0.8$	-0.30	0.0	-0.42
$0.8 < \chi < 0.9$	-0.17	0.0	-0.28

The effects of radiation at different times of day are notable in this comparison, as radiative heating dominates for daytime flights, while radiative cooling at cloud top dominates for evening flights when solar radiation is reduced. This pattern seems to be largely absent for temperature effects due to phase changes, as evaporative cooling occurs during all flights, regardless of time of day, highlighting the mixing characteristics of the EIL. Plots of average temperature effects (due to radiation and phase changes) over all mixing fractions found within the EIL are shown in Figures 5.11 through 5.15.

In four out of five of our analyzed flights, mixing plays a much more significant role in the mixing process within the EIL than phase changes or radiative processes. During RF10 (daytime flight), RF11, RF12, and RF14 (evening flights), mixing plays a noticeably larger role in modifying parcel temperature, especially for larger mixing fractions. However, for RF16, one of the analyzed daytime flights, radiative heating is pronounced in lower mixing fractions to the point where it outweighs warming due to mixing. The substantial effects of radiation during RF16 can also be seen in mixing line plots for this flight, as they deviate significantly from the linear structure that would be expected from purely mixing effects.

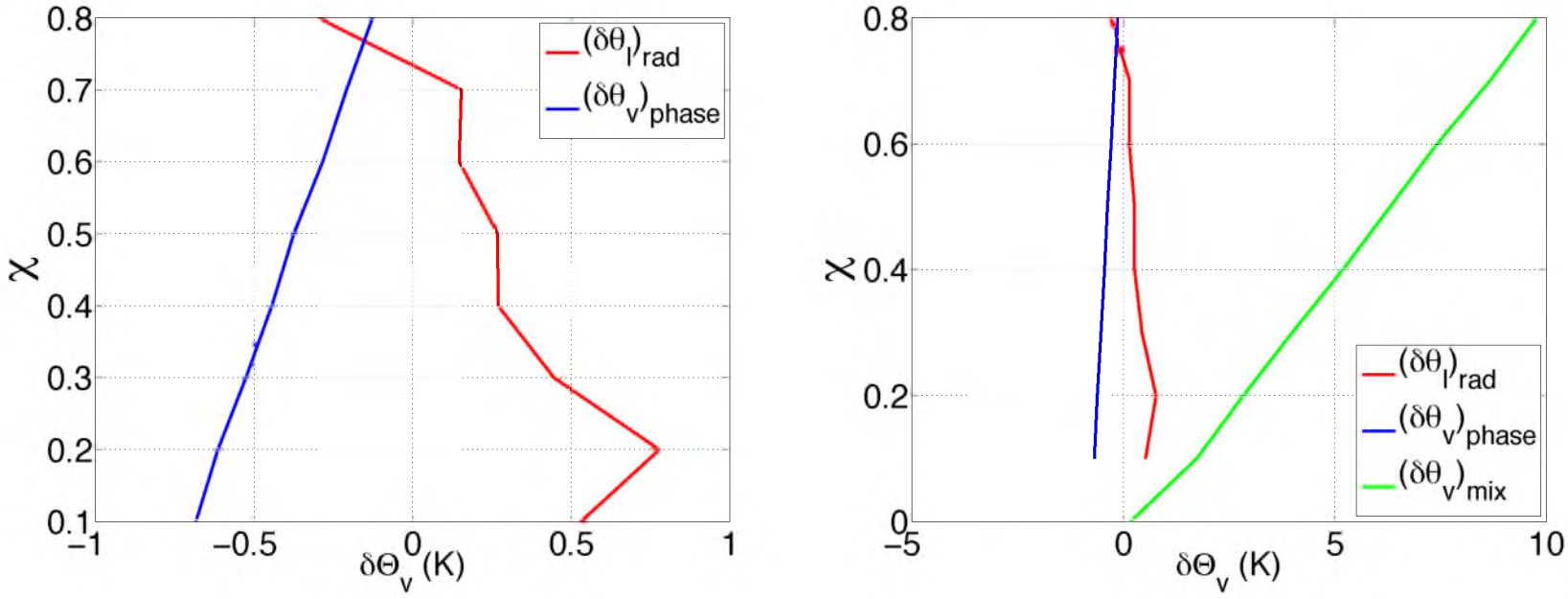

Figure 5.11: Average temperature effects due to radiation (red line) and phase changes (blue line) within the EIL compared to the temperature effects due to mixing (green line) for RF10. $(\delta\theta_l)_{rad}$ and $(\delta\theta_v)_{phase}$ have been binned according to mixing fraction, each bin averaged, and then plotted over the range of mixing fractions found within the EIL. Mixing fraction axis labels correspond to the bottom limit of each bin.

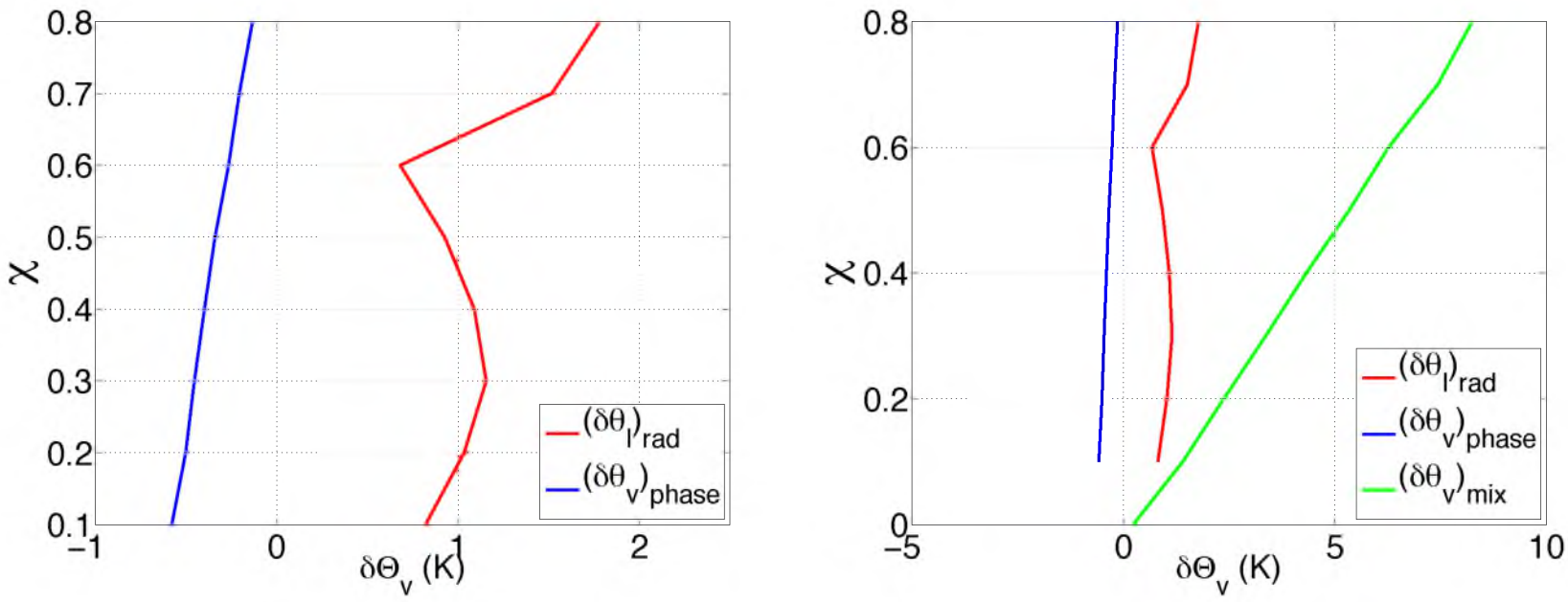

Figure 5.12: Temperature effects due to mixing (green line), compared to temperature effects due to radiation (red line) and phase changes (blue line) within the EIL for evening RF11. $(\delta\theta_l)_{rad}$ and $(\delta\theta_v)_{phase}$ have been binned according to mixing fraction, each bin averaged, and then plotted over the range of mixing fractions found within the EIL. Mixing fraction axis labels correspond to the bottom limit of each bin.

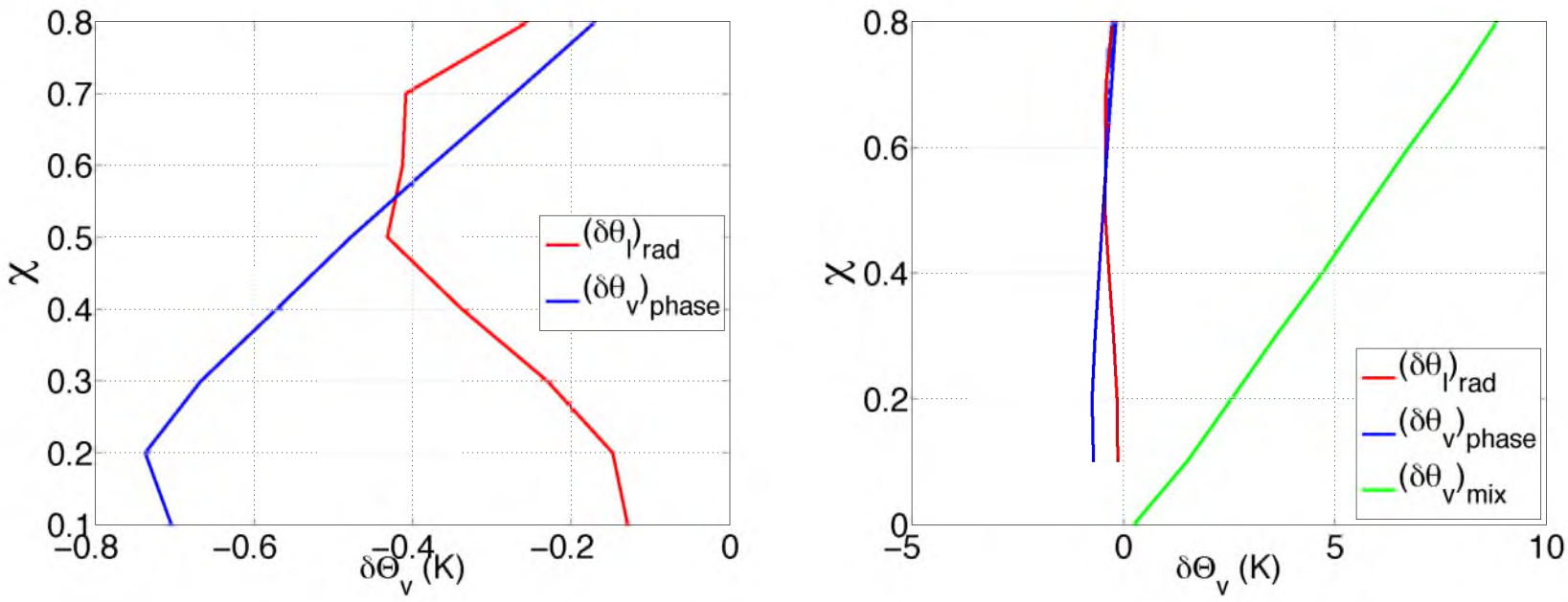

Figure 5.13: Effects on temperature due to radiation (red line) and phase changes (blue line) within the EIL, compared to effects on temperature due to mixing (green line) for RF12. $(\delta\theta_l)_{rad}$ have been binned according to mixing fraction, each bin averaged, and then plotted over the range of mixing fractions found within the EIL, and likewise for $(\delta\theta_v)_{phase}$. Mixing fraction axis labels correspond to the bottom limit of each bin.

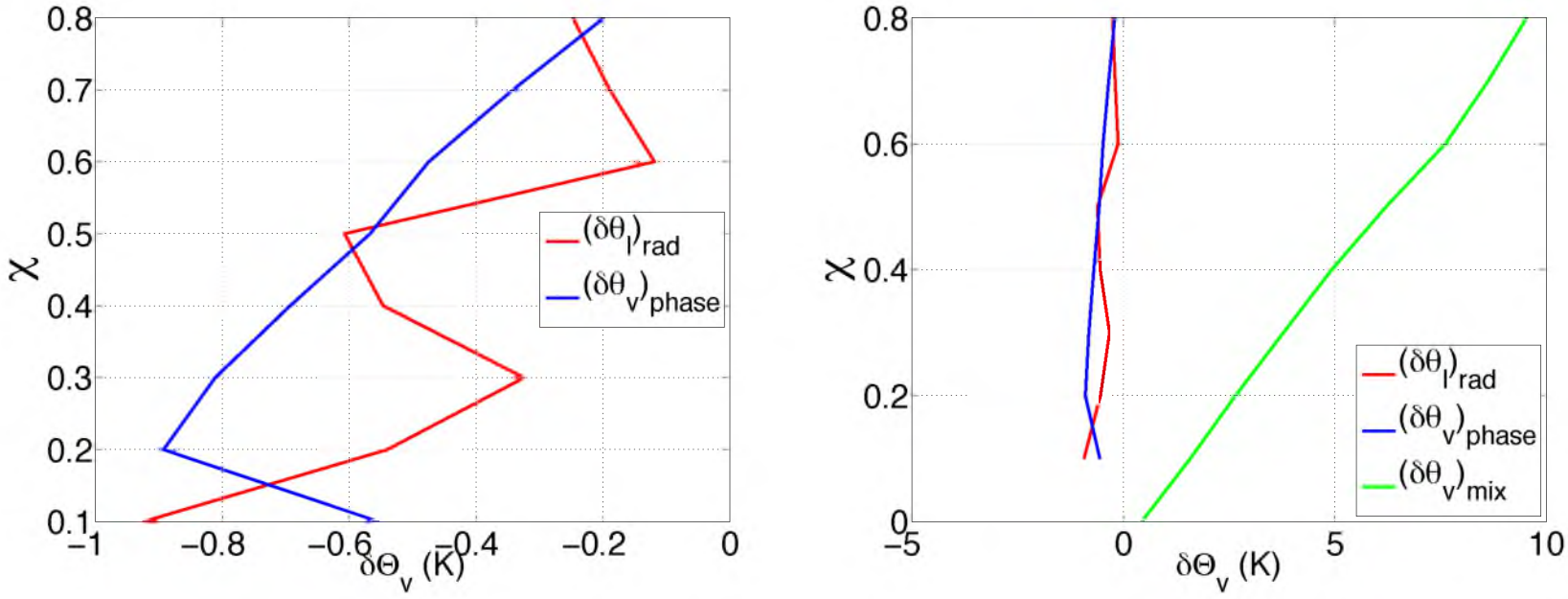

Figure 5.14: Profiles of temperature effects within the EIL for RF14. Contributions from radiation (red line), and phase changes (blue line) are shown in the first figure, while these effects are both compared to the contribution from mixing (green line) in the second figure. For both $(\delta\theta_l)_{rad}$ and $(\delta\theta_v)_{phase}$, values have been binned over the range of mixing fractions found within the EIL, and then plotted according to mixing fraction bins. Axis labels correspond to mixing fraction bottom limits for each bin.

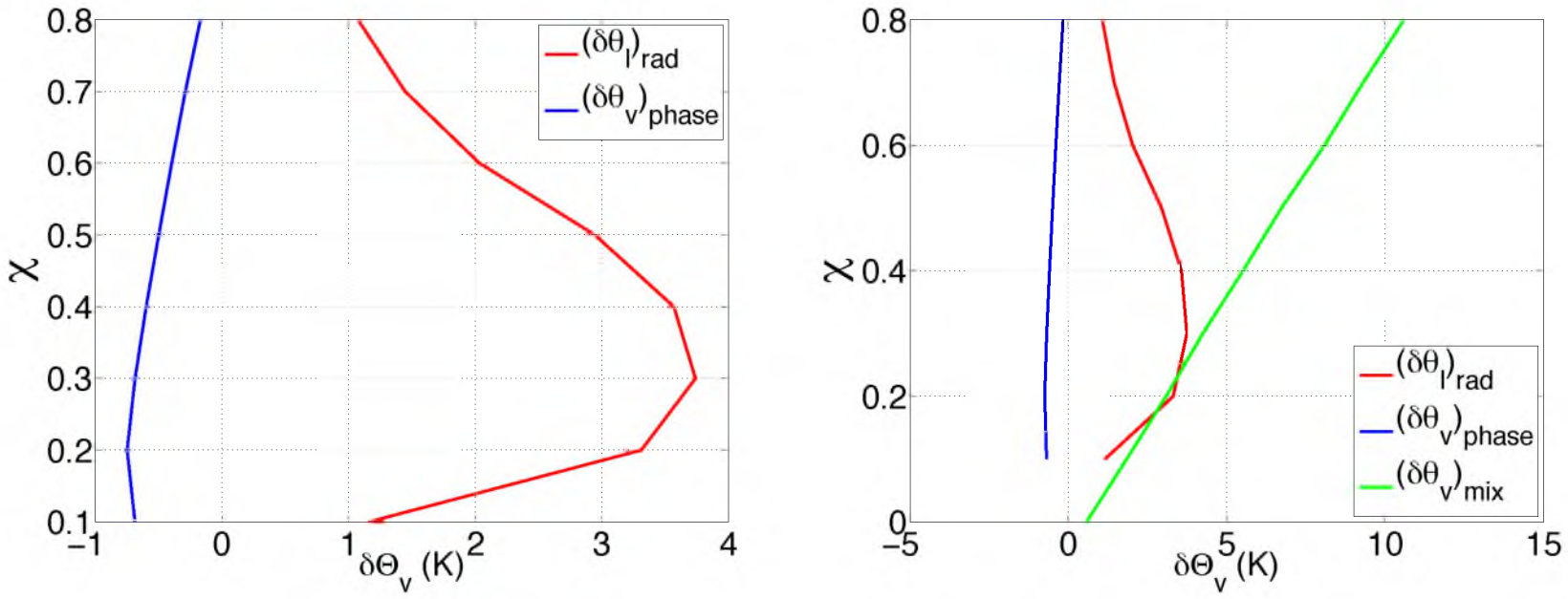

Figure 5.15: Average temperature effects due to radiation (red line) and phase changes (blue line) within the EIL compared to the temperature effects due to mixing (green line) for RF16. $(\delta\theta_l)_{rad}$ and $(\delta\theta_v)_{phase}$ have been binned according to mixing fraction, each bin averaged, and then plotted over the range of mixing fractions found within the EIL. Mixing fraction axis labels correspond to the bottom limit of each bin.

CHAPTER 6

CONCLUSIONS AND DISCUSSION

6.1 The EIL

Based on our calculations of mixing fraction, we find a well-defined, substantial EIL between the cloudy mixed layer and the free troposphere for all five flights that were analyzed. These results support the idea that there exists a region between the free troposphere and the cloudy mixed layer of STBLs that has properties intermediate between those of the overlying atmosphere and those of the boundary layer. Our intermediate values of mixing fraction located at altitudes in between the altitude of the free troposphere and the altitude of the boundary layer suggest that this region is also one containing parcels at different stages in the mixing process.

The thickness of the EIL is highly variable between flights, yet seems to be fairly constant within a given flight. The EIL thickness during POST, as defined by mixing fraction, varies between a minimum value of 8.6 meters (RF12) to a maximum value of 144.5 meters (RF16). However, the EIL as defined by mixing fraction calculations is thicker overall than previously observed EILs of a few tens of meters. Our average EIL thickness results compare favorably with model results from Yamaguchi and Randall (2012), who also approximate the thickness of the EIL to be several tens of meters. The individual values within flights for EIL thickness presented here, however, are at times considerably larger or smaller than this average value.

The time evolution of the EIL is on the order of 0.1 cm/sec in most cases, when EIL

top and bottom heights are binned according to longitude, with a few extreme cases with much larger values. Finally, as the EIL characteristics of the five flights do not seem to show any dependence on whether the flights were flown during the day or in the evening, it seems that there are many other factors that influence the EIL other than the diurnal cycle of marine STBLs.

6.2 Effects of Radiation and Phase Changes

Calculations of temperature changes due to radiative processes and phase changes reveal that radiation and phase changes have a effect on temperatures on the same order, on average, within the EIL for POST flights. Warming due to solar radiation is observed for both daytime flights RF10 and RF16. Especially during RF16, significant radiative warming outweighs radiative cooling to produce net warming within the EIL. Radiative cooling dominates for evening flights, when solar radiation is reduced. Evaporative cooling is the primary effect of phase changes for all five flights, regardless of whether the flight was flown during the day or during the evening. This is conducive to the idea of the EIL as a region of mixing, as subsaturated free tropospheric air comes in contact with saturated cloud layer air at the interface between the two layers, and evaporation of cloud droplets causes cooling.

6.3 Future Work

Observations collected during the POST field campaign make up a dataset with unparalleled resolution in time and space, which has proven extremely useful for investigations into the small scale structure of the EIL and the region near cloud top. The potential exists, with this high rate data, for the detection of individual turbulent mixing events within the velocity fields. This would provide further insight into how mixing takes place in the EIL, and may lead to a greater understanding of how the EIL affects the cloudy mixed layer. An effective way to complete this analysis may be through the use of the relatively recently

developed wavelet method, where asymmetric waveforms have been used to detect sporadic events within a flow field through a multi resolution analysis. Due to the enormous amount of work and testing inherent in wavelet analysis, this endeavor was deemed beyond the scope of this thesis.

In addition, analysis of recent LES model results for model runs under similar conditions as the California marine STBLs during POST may prove beneficial to further understanding the results presented in this thesis. Comparison between observations and model results may help to isolate some of the factors influencing the EIL under a variety of atmospheric conditions.

REFERENCES

Ackerman, A. S., M. P. Kirkpatrick, D. E. Stevens, and O.B. Toon, 2004: The impact of humidity above stratiform clouds on indirect aerosol climate forcing. *Nature*, **432**, 1014-1017.

Ackerman, A.S., M.C. vanZanten, B. Stevens, V. Savic-Jovcic, C.S. Bretherton, A. Chlond, J.-C. Golaz, H. Jiang, M. Khairoutdinov, S.K. Krueger, D.C. Lewellen, A. Lock, C.-H. Moeng, K. Nakamura, M.D. Petters, J. R. Snider, S. Weinbrecht, and M. Zulauf, 2009: Large-eddy simulations of a drizzling, stratocumulus-topped marine boundary layer. *Monthly Weather Review*, **137** (**3**), 1083-1110.

Albrecht, B. A., C.S. Bretherton, D. Johnson, W. H. Schubert, and A.S. Frisch, 1995: The atlantic stratocumulus transition experiment - ASTEX. *Bull. Am. Meteor. Soc.*, **54**, 1004-1012.

Austin, P., Y. Wang, R. Pincus, and V. Kujala, 1995: Precipitation in stratocumulus clouds: observations and modeling results. *J. Atmos. Sci.*, **52**, 2329-2352.

Brenguir, J.-L., H. Pawlowska, L. Schuller, R. Preuser, J. Fischer, and Y. Fouquart, 2000: Radiative properties of boundary layer clouds: droplet effective radius versus number concentration. *Journal of the Atmospheric Sciences*, **57** (**6**), 803-821.

Brenguier, J.-L. and R. Wood, 2009: Observational strategies from the micro to meso scale. *Perturbed clouds in the climate system*, MIT Press.

Bretherton, C.S., P. Austin, and S.T. Siems, 1995: Cloudiness and marine boundary layer dynamics in the ASTEX lagrangian experiments. Part II: Cloudiness, drizzle, surface fluxes and entrainment. *J. Atmos. Sci.*, **52**, 2724-2735.

Bretherton, C.S. and D. L. Hartmann, 2008: Large-scale controls on cloudiness. In Perturbed clouds in the climate system, J. Heintzenberg and R. J. Charlson (eds.). Ernst strungmann forum, Frankfurt Institute for Advanced Study.

Bretherton, C.S. MacVean, M.K., Bechtold, P., Chlong, A., Cotton, W.R., Cuxart, J., Cuijpers, H., Khairoutdinov, M., Kosovic, B., Lewellen, D., Moeng, C.-H., Siebesma, P., Stevens, B., Stevens, D.E., Sykes, I., Wyant, M.C, 1999: An intercomparison of radiatively driven entrainment and turbulence in a smoke cloud, as simulated by different numerical models. *Quarterly Journal of the Royal Meteorological Society*, **125**, 391-423.

Bretherton, C.S. and R. Pincus, 1995: Cloudiness and marine boundary layer dynamics in the ASTEX lagrangian experiments. Part I: Synoptic setting and vertical structure. *J. Atmos. Sci.*, **52**, 2707-2723.

Bretherton, C.S. and M.C. Wyant, 1997: Moisture transport, lower-tropospheric stability, and decoupling of cloud-topped boundary layers. *J. Atmos. Sci.*, **54**, 148-167.

Bretherton, C.S., 1997: Convection in Stratocumulus-Capped Atmospheric Boundary Layers. In *The Physics and Parameterization of Moist Atmospheric Convection*, R.K. Smith, ed., Klumer Publishers, 127-142 (peer-reviewed book chapter).

Burk, S.D. and W.T. Thompson, 1996: The summertime low-level jet and marine boundary layer structure along the California coast. *Monthly Weather Review*, **124**, 668-686.

Burnet, F. and J.-L. Brenguier, 2007: Observational study of the entrainment-mixing process in warm convective clouds. *J. Atmos. Sci*, **64**, 1995-2011.

Bony, S., R. Colman, V. M. Kattsov, R. P. Allan, C. S. Bretherton, J.-L. Dufresne, A. Hall, S. Hallegatte, M. M. Holland, W. Ingram, D. A. Randall, B. J. Soden, G. Tselioudis, and M. J. Webb, 2006: How well do we understand and evaluate climate change feedback processes? *J. Climate*, **19** (**15**), 3445-3482.

Caldwell, P. and C. S. Bretherton, 2008: Response of a subtropical stratocumulus-capped mixed layer to climate and aerosol changes. *J. Climate*, submitted.

Caldwell, P., R. Wood, and C.S. Bretherton, 2005: Mixed-layer budget analysis of the diurnal cycle of entrainment in SE Pacific stratocumulus. *J. Atmos. Sci.*, **62**, 3775-3791.

Caughey, S. J., B. A. Crtease, and W. T. Roach, 1982: A field-study of nocturnal stratocumulus turbulence structure and entrainment. *Quarterly Journal of the Royal Meteorological Society*, **108** (**455**), 125-144.

Deardorff, J. W., 1981: On the distribution of mean radiative cooling at the top of stratocumulus-capped mixed layer. *Quarterly Journal of the Royal Meteorological Society*, **107** (**451**), 191-202.

Deardorff, J. W., 1980: Cloud-top entrainment instability. *J. Atmos. Sci.*, **37**, 131-147.

de Roode, S. R. and P. G. Duynkerke, 1997: Observed lagrangian transition of stratocumulus into cumulus during ASTEX: mean state and turbulence structure. *J. Atmos. Sci.*, **54**, 2157-2173.

de Roode, S. R. and Q. Wang, 2007: Do stratocumulus clouds detrain? FIRE I data revisited. *Bound. Layer Meteorol.*, **122** (**2**), 479-491.

Duynkerke, P.G., 1993: The stability of cloud top with regard to entrainment - amendment of the theory of cloud-top entrainment instability. *J. Atmos. Sci*, **50** (**3**), 495-502.

Duynkerke, P. G. and P. Hignett, 1993: Simulation of a diurnal variation in a stratocumulus-capped marine boundary layer during FIRE. *Mon. Wea. Rev.*, **121**, 3291-3300.

Duynkerke, P. G., H. Q. Zhang, and P. J. Jonker, 1995: Microphysical and turbulent structure of nocturnal stratocumulus as observed during ASTEX. *J. Atmos. Sci.*, **52** (**16**), 2763-2777.

Gerber, H., S. Chang, and T. Holt, 1989: Evolution of a boundary-layer jet. *J. Atmos. Sci*, **46**, 1312-1326.

Gerber, H., G. Frick, S. P. Malinowski, J. L. Brenguier, and F. Burnet, 2005: Holes and entrainment in stratocumulus. *J. Atmos. Sci*, **62** (**2**), 443-459.

Gerber, H., S.P. Malinowski, J.L. Brenguier, and F. Burnet, 2002: On the entrainment process in stratocumulus clouds. Preprints, 11th Conf. on Cloud Physics, Ogden, UT, Amer. Meteor. Soc., CD-ROM, paper JP7.6.

Haman, K. E., S. P. Malinowski, M. J. Kurowski, H. Gerber, and J. L. Brenguier, 2007: Small scale mixing processes at the top of a marine stratocumulus - a case study. *Quarterly Journal of the Royal Meteorological Society*, **133**, (**622**), 213-226.

Hartmann, D. L, M. E. Ockert-Bell, and M. L. Michelsen, 1992: The effect of cloud type on earth's energy balance - global analysis. *J. Climate*, **5**, 1281-1304.

Hignett, P., 1991: Observations of diurnal variation in a cloud-capped marine boundary layer. *J. Atmos. Sci.*, **48**, 1474-1482.

Kalogiros, J. and Q. Wang, 2001: The California low-level coastal jet and nearshore stratocumulus. *Extended Abstract*, 4th Conf. on Coastal Atmospheric and Oceanic Prediction and Processes, St. Petersburg, FL, Amer. Meteor. Soc.

Kawa, S. R. and R. Pearson Jr., 1989: An observational study of stratocumulus entrainment and thermodynamics. *J. Atmos. Sci*, **46**, 2649-2661.

Klein, S. A. and D. L. Hartmann, 1993: The seasonal cycle of low stratiform clouds. *J. Climate*, **6**, 1588-1606.

Krueger, S. K., 1993: Linear eddy modeling of entrainment and mixing in stratus clouds. J. Atmos. Sci., 50, 3078-3090.

Krueger, S.K., G. T. McLean, and Q. Fu, 1995a: Numerical simulation of the stratus-to-cumulus transition in the subtropical marine boundary layer. Part I: Boundary-layer structure. *J. Atmos. Sci*, **52**, 2839-2851.

Krueger, S.K., G. T. McLean, and Q. Fu, 1995b: Numerical simulation of the stratus-to-cumulus transition in the subtropical marine boundary layer. Part II: Boundary-layer circulation. *J. Atmos. Sci*, **52**, 2851-2868.

Kuo, H.-C. and W. H. Schubert, 1988: Stability of cloud-topped boundary layers. *Quart. J. Roy. Meteorol. Soc.*, **114**, 887-916.

Lilly, D. K., 1968: Models of cloud-topped mixed layers under a strong inversion. *Quart. J. Roy. Meteorol. Soc.*, **94**, 292-309.

Leon, D. C., Z. Wang, and D. Liu, 2008: Climatology of drizzle in marine boundary layer clouds based on 1 year of data from CloudSat and Cloud-Aerosol Lidar and Infrared Pathfinder Satellite Observations (CALIPSO). *J. Geophys. Res.*, **113 (D00A14)**, doi: 10.1029/2008JD009835.

Lenschow, D. H., M. Y. Zhou, X. B. Zeng, L. S. Chen, and X. D. Xu, 2000: Measurements of fine-scale structure at the top of marine stratocumulus. *Boundary-Layer Meteorology*, **97** (**2**), 331-357.

Lewellen, D. C. and W. S. Lewellen, 1998: Large-eddy boundary layer entrainment. *J. Atmos. Sci.*, **55**, 2645-2665.

MacVean, M. K. and P. J. Mason, 1990: Cloud-top entrainment instability through small-scale mixing and its parameterization in numerical models. *J. Atmos. Sci.*, **47**, 1012-1030.

Mechem, D. B. and Y. Kogan, 2003: Simulating the transition from drizzling marine stratocumulus to boundary layer stratocumulus with a mesoscale model. *Monthly Weather Revew*, **131**, 2342-2360.

Miller, M. A., M. P. Jensen, and E. E. Clothiaux, 1998: Diurnal cloud and thermodynamic variations in the stratocumulus transition regime: A case study using in situ and remote sensors. *J. Atmos. Sci.*, **55** (**13**), 2294-2310.

Moeng, C. H., W. R. Cotton, C. Bretherton, A. Chlond, M. Khairoutdinov, S. Krueger, W. S. Lewellen, M. K. MacVean, J. R. M. Pasquier, H. A. Rand, A. P. Siebesma, B. Stevens, and R. I. Sykes, 1996: Simulation of a stratocumulus-topped planetary boundary layer: Intercomparison among different numerical models. *Bull. Am. Meteor. Soc.*, **77** (**2**), 261-278.

Moeng, C. H., S. H. Shen, and D. A. Randall, 1992: Physical processes within the nocturnal stratus-topped boundary layer. *J. Atmos. Sci.*, **49**, 2384-2401.

Nicholls, S., 1989: The structure of radiatively driven convection in stratocumulus. *Quart. J. Roy. Meteor. Soc.*, **115**, 487-511.

Nicholls, S., 1984: The dynamics of stratocumulus: aircraft observations and comparison with a mixed layer model. *Quart. J. Roy. Meteorol. Soc.*, **110**, 783-820.

Nicholls, S. and J. Leighton, 1986: An observational study of the structure of stratiform cloud sheets: Part I. Structure. *Quart. J. Roy. Meteorol. Soc.*, **112**, 431-460.

Nicholls, S. and J. D. Turton, 1986: An observational study of the structure of stratiform cloud sheets: Part II. Entrainment. *Quart. J. Roy. Meteorol. Soc.*, **112**, 461-480.

Nieuwstadt, F. T. M. and J. A. Businger, 1984: Radiative cooling near the top of a cloudy mixed layer. *Quart. J. Meteorol. Soc.*, **110**, 1073-1078.

Ohtake, T., 1963: Hemispheric investigations of warm rain by radiosonde data. *J. Appl. Meteorol.*, **2**, 594-607.

Paluch, I. R., 1979: The entrainment mechanism in Colorado cumuli. *J. Atmos. Sci.*, **36**, 2467-2478.

Paluch, I. R. and D. H. Lenschow, 1991: Stratiform cloud formation in the marine boundary layer. *J. Atmos. Sci.*, **48**, 2141-2158.

Pawlowska, H. and J. L. Brenguir, 2003: An observational study of drizzle formation in stratocumulus clouds for general circulation model (GCM) parameterizations. *J. Geophys. Res.*, **108**, 8630, doi: 10.1029/2002JD002679.

Pearson, R. and C. J. Weaver, 1989: Ozone conservation and entrainment in cumulus congestus. *J. Atmos. Sci.* **46**, 2031-2043.

Petty, G. W., 1995: Frequencies and characteristics of global oceanic precipitation from shipboard present-weather reports. *Bull. Amer. Meteor. Soc.*, **76**, 1593-1616.

Randall, D. A., 1980: Conditional instability of the first kind upside-down. *J. Atmos. Sci.*, **37**, 125-130.

Randall, D. A., J. A. Coakley, C. W. Fairall, R. A. Knopfli, and D. H. Lenschow, 1984: Outlook for research on marine stratocumulus clouds. *Bull. Am. Meteor. Soc.*, **65**, 1290-1301.

Schubert, W. H., J. S. Wakefield, E. J. Steiner, and S. K. Cox, 1979: Marine stratocumulus convection. Part I: Governing equations and horizontally homogeneous solutions. *J. Atmos. Sci.*, **36**, 1286-1307.

Siems, S. T., D. H. Lenschow, and C. S. Bretherton, 1993: A numerical study of the interaction between stratocumulus and the air overlying it. *J. Atmos. Sci.*, **50**, 3663-3676.

Slingo, A., 1990: Sensitivity of the earth's radiation budget to changes in low clouds. *Nature*, **343**, 49-51.

Stevens, B., W. R. Cotton, G. Feingold, and C.-H. Moeng, 1998: Large-eddy simulations of strongly precipitating, shallow, stratocumulus-topped boundary layers. *J. Atmos. Sci.*, **55**, 3616-3638.

Stevens, B., C.-H. Moeng, A. S. Ackerman, C. S. Bretherton, A. Chlond, S. de Roode, J. Edwards, J.-C. Golaz, H. Jiang, M. Khairoutdinov, M. P. Kirkpatrick, D. C. Lewellen, A. Lock, F. Müller, D. E. Stevens, E. Whelan, and P. Zhu, 2005: Evaluation of large-eddy simulations via observations of nocturnal marine stratocumulus. *Monthly Weather Review*, **133** (**6**), 1443-1462.

vanZanten, M. C. and P.G. Duynkerke, 2002: Radiative and evaporative cooling in the entrainment zone of stratocumulus - the role of longwave radiative cooling above cloud top. *Bound.-Layer Meteor.*, **102**, 253-280.

vanZanten, M.C., B. Stevens, G. Vali, and D. Lenschow, 2005: Observations of drizzle in nocturnal marine stratocumulus. *J. Atmos. Sci.*, **62**, 88-106.

Wang, Q. and B. A. Albrecht, 1994: Observations of cloud-top entrainment in marine stratocumulus clouds. *J. Atmos. Sci.*, **51**, 1530-1547.

Wang, S. and B. A. Albrecht, 1986: A stratocumulus model with an internal circulation. *J. Atmos. Sci*, **43**, 2374-2391.

Weaver, C. J. and R. Pearson, 1990: Entrainment instability and vertical motion as causes of stratocumulus breakup. *Quarterly Journal of the Royal Meteorological Society*, **116** (**496**), 1359-1388.

Wood, R., 2007: Cancellation of aerosol indirect effects in marine stratocumulus through cloud thinning. *J. Atmos. Sci.*, **64**, 2657-2669.

Wood, R., 2005: Drizzle in stratiform boundary layer clouds: Part I. Vertical and horizontal structure. *J. Atmos. Sci.*, **62**, 3011-3033.

Wood, R. and C.S. Bretherton, 2004: Boundary layer depth, entrainment and decoupling in the cloud-capped subtropical and tropica marine boundary layer. *J. Climate*, **17**, 3576-3588.

Wood, R., M. Kohler, R. Bennartz, and C. O'Dell, 2009: The diurnal cycle of surface divergence over the global oceans. *Q. J. R. Meteorol. Soc.*, **135**, 1484-1493.

Wyant, M.C., C.S. Bretherton, J.T. Bacmeister, J.T. Jiehl, I. M. Held, M. Zhao, S. A. Klein, and B.A. Soden, 2006: A comparison of tropical cloud properties and responses in GCMs using mid-tropospheric vertical velocity. *Climate Dyn.*, textbf27, 261-279.

Wyant, M. C., C. S. Bretherton, H. A. Rand, and D. E. Stevens, 1997: Numerical simulations and a conceptual model of the stratocumulus to trade cumulus transition. *J. Atmos. Sci.*, **54**, 168-192.

Yamaguchi, T. and D.A. Randall, 2012: Cooling of entrained parcels in a Large-Eddy Simulation. *J. Atmos. Sci.*, **69**, 1118-1136.

Yamaguchi, T. and D. A. Randall, 2008: Large-eddy simulation of evaporatively driven entrainment in cloud-topped mixed layers. *J. Atmos. Sci.*, **65**, 1481-1504.

Zemba, J. and C. A. Friehe, 1987: The marine atmospheric boundary layer jet in the Coastal Ocean Dynamics Experiment. *J. Geophys. Res.*, **92**, 1489-1496.